Scholars' Mine

Doctoral Dissertations

Student Theses and Dissertations

Spring 2019

Freeform extrusion fabrication of advanced ceramics and ceramic-based composites

Wenbin Li

FREEFORM EXTRUSION FABRICATION OF ADVANCED CERAMICS AND

CERAMIC-BASED COMPOSITES

by

WENBIN LI

A DISSERTATION

Presented to the Faculty of the Graduate School of the

MISSOURI UNIVERSITY OF SCIENCE AND TECHNOLOGY

In Partial Fulfillment of the Requirements for the Degree

DOCTOR OF PHILOSOPHY

in

MECHANICAL ENGINEERING

2019

Approved by:

Ming C. Leu, Advisor
Robert G. Landers
Gregory E. Hilmas
Frank Liou
Jie Huang

PUBLICATION DISSERTATION OPTION

This dissertation consists of the following four articles, formatted in the style used by the Missouri University of Science and Technology:

Paper I, "Extrusion-On-Demand Methods for High Solids Loading Ceramic Paste in Freeform Extrusion Fabrication," was published in Virtual and Physical Prototyping journal and can be found on pages 15-45.

Paper II, "Characterization of Zirconia Specimens Fabricated by Ceramic On-Demand Extrusion," was published in Ceramics International Journal and can be found on pages 46-75.

Paper III, "Fabricating Ceramic Components with Water Dissolvable Support Structures by the Ceramic On-Demand Extrusion Process," was published in CIRP Annals - Manufacturing Technology journal and can be found on pages 76-92.

Paper IV, "Fabricating Functionally Graded Materials by Ceramic On-Demand Extrusion with Dynamic Mixing," was published in proceedings of *Solid Freeform Fabrication Symposium* and can be found on pages 93-112.

ABSTRACT

Ceramic On-Demand Extrusion (CODE) is a recently developed freeform extrusion fabrication process for producing dense ceramic components from single and multiple constituents. In this process, aqueous paste of ceramic particles with a very low binder content (<1 vol%) is extruded through a moving nozzle to print each layer sequentially. Once one layer is printed, it is surrounded by oil to prevent undesirable water evaporation from the perimeters of the part. The oil level is regulated just below the topmost layer of the part being fabricated. Infrared radiation is then applied to uniformly and partially dry the top layer so that the yield stress of the paste increases to avoid part deformation. By repeating the above steps, the part is printed in a layer-wise fashion, followed by post-processing. Paste extrusion precision of different extrusion mechanisms was compared and analyzed, with an auger extruder determined to be the most suitable paste extruder for the CODE system. A novel fabrication system was developed based on a motion gantry, auger extruders, and peripheral devices. Sample specimens were then produced from 3 mol% yttria stabilized zirconia using this fabrication system, and their properties, including density, flexural strength, Young's modulus, Weibull modulus, fracture toughness, and hardness were measured. The results indicated that superior mechanical properties were achieved by the CODE process among all the additive manufacturing processes. Further development was made on the CODE process to fabricate ceramic components that have external/internal features such as overhangs by using fugitive support material. Finally, ceramic composites with functionally graded materials (FGMs) were fabricated by the CODE process using a dynamic mixing device.

ACKNOWLEDGMENTS

I would like to thank my advisor, Dr. Ming Leu, for providing me with the opportunity to work on this project and for advising me on my research. Further, I thank the Department of Energy's Office of Fossil Fuels, Kansas City National Security Campus, and Intelligent Systems Center (ISC) at Missouri S&T for providing financial support at various stages of my Ph.D. study.

I would like to thank Drs. Robert Landers, Greg Hilmas and Jeremy Watts for their helpful discussions and constructive suggestions during my graduate study. Thanks to Dr. Frank Liou and Dr. Jie Huang for helpful suggestions and serving on my advisory committee.

I would like to acknowledge all current and past members of the CODE/FEF Research Group, and especially, Amir Ghazanfari, Devin McMillen, and Austin Martin for our productive discussions and all the help over the years. I also thank graduate students from the UHTC laboratory, and especially, Ryan Grohsmeyer for his help during mechanical characterization experiments.

Finally, I would like to dedicate this work to my parents Chunmao Li and Liangfeng Fu for their emotional support and unconditional love and sacrifices.

TABLE OF CONTENTS

SECTION

LIST OF ILLUSTRATIONS

LIST OF TABLES

SECTION

1. INTRODUCTION

1.1. BACKGROUND AND RESEARCH OBJECTIVES

Additive Manufacturing (AM) of advanced ceramics has several advantages over traditional processing techniques including ease of fabricating geometrically complex parts and reduction of manufacturing costs for one-of-a-kind parts or small batches. Several AM techniques have been developed to fabricate three-dimensional (3D) ceramic components, including binder jetting [1], material extrusion [2]–[6], vat photopolymerization [7]–[10], powder bed fusion [11], [12], directed energy deposition [13]–[16], etc. All these techniques involve adding ceramic materials layer by layer. A comprehensive review of the additive manufacturing of ceramic-based materials was recently presented by Travitzky et al. [17].

Many efforts to additively manufacture ceramic components resulted in parts with defects (i.e., flaws or large porosity caused by additive manufacturing). It is well-known that the mechanical strength of ceramics is highly dependent on defects due to their crack-sensitive nature, and they would be expected to exhibit poor mechanical properties even at 80% relative density (e.g., [18]). Although these parts may have remarkable geometrical complexity and be suitable for some applications, they are not apt to be used where low porosity and excellent mechanical strength is needed, such as structural ceramics. In many cases, the mechanical properties of these parts are so poor that they are not even reported in papers and technical reports. According to Zocca et al. [19], AM of

monolithic ceramics, pursuing physical and chemical properties that match their conventionally manufactured counterparts, is still a challenge and remains the most important task that needs to be solved to promote AM of ceramics to more than a niche technology. Extrusion-based AM processes are among the most popular approaches for freeform fabrication of ceramic parts due to the simplicity and low cost of their fabrication system, high density (low porosity) of their fabricated parts, their capability of producing components with multiple materials [18] including functionally graded materials [20], [21], and the low amount of material wasted during processing. Major extrusion-based processes, which are referred to as freeform extrusion fabrication in this study include Robocasting (RC) [3], [22]–[25], Extrusion Freeform Fabrication (EFF) [26]–[28], Fused Deposition of Ceramics (FDC) [6], [29], [30], Freeze-Form Extrusion Fabrication (FEF) [5], [21], [31], and Thermoplastic 3D Printing (T3DP) [32].

EFF [27] was the first technique which utilized the extrusion of organic-based ceramic slurries to produce 3D ceramic components. Slurries of alumina powders in liquid acrylic monomers were prepared and deposited onto a heated substrate to retain their shape. The process was further improved to fabricate more complex geometries from other materials such as silicon nitride [26].

Danforth introduced the concept of FDC [29]. They used a Stratasys (Stratasys Inc., Eden Prairie, MN, USA) Fused Deposition Modeling (FDM) system to extrude ceramic-loaded thermoplastic filaments. The feedstock filament was liquefied (melt), extruded, deposited and re-solidified by cooling to retain its shape. Since then, they have further improved their process and have been capable of producing high-quality

components from different materials for various applications, especially sensors and actuators [33], [34].

RC [3], [35] is a renowned freeform extrusion fabrication process of ceramics. The main advantage of RC over EFF, FDC, and T3DP is the use of a lower concentration of binder additives in the feedstock (<10 wt% vs. >30 wt%) which simplifies pre-processing and post-processing. Typically, in this process, an aqueous suspension from ceramic particles (e.g., alumina, zirconia, silicon carbide, and silicon nitride) is prepared and extruded on to a heated substrate to dry and retain its shape. RC can produce sparse structures such as grid and thin-walls for various applications [36]–[38], especially for bio-fabrication [39]–[41].

The thermoplastic 3D printing (T3DP) [32] approach proposed by Scheithaue et al. combines FDM and RC, where a thermoplastic binder system was used to prepare highly loaded feedstocks. The feedstocks were processed in a heatable syringe extruder with XYZ positioning. The thermoplastic feedstocks are based on compositions that are known from low-pressure injection molding. The liquid feedstock (i.e., suspension) can be dispensed via a thin nozzle as nearly endless filament which is similar to FDM and robocasting, or be dispensed as droplets by micro-dispensing technology, which allows the realization of fine structures with higher dimensional resolution. The heated suspension is printed layer by layer. The suspension solidifies upon the deposition due to cooling because of the fast heat transfer from the deposited suspension to the underlying layer and the surrounding atmosphere.

In the FEF process [31], a high solids loading (> 50 vol%) aqueous ceramic paste containing 1-4 vol% of organic additives is extruded in a freezing environment (< -10 °C)

to solidify the paste after being deposited. Freeze drying is then utilized to remove the water content, followed by sintering. The FEF process is also capable of producing complex and functionally graded material (FGM) parts made of different materials such as alumina, zirconium diboride, boron carbide, zirconium carbide, and bio-active glasses [21], [42]–[44]. Advanced controls were also implemented to enhance the precision of extrusion-on-demand and consistency in paste flow rate [45]–[48].

While later extrusion-based additive manufacturing processes have their respective advantages, they also have limitations. The binder removal procedures for EFF FDC and T3DP required extra time and effort, and sometimes causes defects such as warpage and cracks. It might involve multiple cycles of firing with different atmospheres. For FDC, the feedstock filament preparation is also burdensome and requires multiple steps. The filament must also maintain a very tight tolerance of its diameter (<2% variation in diameter) to ensure consistent flow rates [49]. Although parts made of multiple materials can be produced, FDC is not capable of mixing them to fabricate functionally graded parts. It is difficult for RC to build large solid (non-sparse) parts due to the stresses occurred in the non-uniform drying which causes warpage and cracks in the parts. Furthermore, due to the presence of air bubbles in the suspension and inconsistency in extrudate flow rate, the fabricated parts are not fully dense, and their mechanical properties do not match that of parts produced by EFF and FDC. The ice crystal formation during the freezing process and weak layer-to-layer bonding in FEF reduce the relative density and mechanical properties of the parts after sintering [50]. Finally, all these extrusion-based processes suffer from nozzle clogging due to the

agglomeration of ceramic particles and binder in the feedstock, and freezing or drying of paste inside the nozzle tip.

To address the above challenges, the Ceramic On-Demand Extrusion (CODE) process was proposed [51]–[55]. In this process, viscous suspensions (pastes) [56]–[59] of ceramic particles are extruded at controlled flow rates through a nozzle. The nozzle is attached to a 3-axis motion stage which is capable of traveling in X, Y and Z directions through G & M codes generated from an indigenously developed toolpath planning program. The extruded feedstock is deposited on a substrate located in a vat designed to hold a fluid medium. Upon the completion of each layer, a liquid feeding device pumps the fluid medium (normally light mineral oil) into the vat to surround the layer to preclude water evaporation from the sides of the deposited layers. The level of the liquid is regulated at a level that is just (~ 2 mm) below the top surface of the part being fabricated. Infrared radiation is then applied on top of the part to uniformly dry the deposited layer so that the part retains its shape. The part is fabricated layer-by-layer by repeating the layered deposition and the controlled layerwise uniform drying. This layered uniform radiational drying approach minimizes the water content gradient in the fabricated part, mitigates the stresses caused by drying, and thus enables the CODE process to produce crack-free, thick ceramic (minimum wall thickness > 1cm) parts with complex geometries [57]–[63]. Once the printing process is completed, the remaining water content in the printed part is removed by bulk drying to obtain green parts. The green part is then fired to remove the binder content, and sintered at elevated temperatures.

The current research aims to improve the quality of fabricated components, as well as to enhance the CODE's flexibility concerning component geometry and constituent distribution. This research attempts to answer four main research questions:

1)   For three typical extrusion mechanisms, namely, a ram extruder, a shutter valve-based extruder, and an auger extruder, how to select among them for different extrusion-based AM processes, and which one is most suitable for the CODE process?

2)   What are the support materials that can be used for freeform extrusion fabrication of ceramics?

3)   For fabricating functionally gradient material parts by the CODE process, how to address the following challenges: reducing the material transition delay, blending multiple materials to high homogeneity, preventing part warping and cracking caused by residual stresses during printing and post-processing?

4)   How will the material grading of ceramic FGMs affect their dimensional accuracy? Will smoother material gradients lead to less distortion of the final specimens?

To answer the above research questions, different extrusion techniques were investigated, and an auger extruder was chosen for the CODE process to increase the precision of material deposition in an attempt to achieve high density of the fabricated components. Materials and methods of fabricating components with sacrificial supports were investigated to broaden the range of geometries that could be fabricated by this process. Methods and apparatus for fabricating composites, specifically, with functionally

gradient materials (FGMs) by the CODE process were developed. Al_2O_3/ZrO_2 FGM specimens were fabricated using different composition grading steps. The dimensional accuracy of the specimens was characterized, and the relation between the material grading and distortion were investigated.

1.2. EXTRUSION-ON-DEMAND

Freeform extrusion fabrication processes deposit ceramic extrudate layer-by-layer through material extrusion. Precise control of the deposition flow rate is required to fabricate highly dense parts with complex geometries. Inaccurate extrusion start and stop, as well as fluctuations in the extrudate flow rate, lead to the formation of pores in parts, which is a common problem in both filament-based and paste-based freeform extrusion fabrication processes [3], [37], [39]–[41], [57]. Throughout the layer-by-layer deposition process, these defects will accumulate and may eventually cause part failure or reduce the strength of the final part, especially for freeform fabrication of brittle ceramic and glass materials [4], [39]–[41], [64]–[67].

Paste extrusion for freeform extrusion fabrication processes is typically accomplished with a ram extruder, which is a positive placement extruder and consists of a syringe and a plunger. Note that a pneumatic extruder is also used for freeform extrusion fabrication. However, since it controls the extrusion flow rate only by regulating the air pressure instead of piston velocity, its extrusion accuracy is not comparable to a positive displacement extruder [68]. Thus it is not investigated and compared to ram extrusion in this study. Based on ram extrusion, several methods regulating the extrusion force and plunger velocity have been developed for the Freeze-

form Extrusion Fabrication (FEF) process. Zhao et al. (2010) [48] designed an adaptive controller with a general tracking control law and implemented it to regulate the extrusion force. Deuser et al. (2013) [47] developed a hybrid force/velocity controller to regulate both the steady-state extrusion flow rate using a plunger velocity controller and extrusion-on-demand using an extrusion force controller. Oakes et al. (2009) [69] developed a dwell technique and a look-forward technique to compensate for the delay of extrusion start and stop for improving Extrusion-On-Demand (EOD) performance. Zomorodi and Landers (2016) [46] developed a hierarchical model-based predictive control algorithm to systematically perform hybrid force-velocity control to extrude paste and draw consistent lines.

The previous efforts to develop ram extruder based extrusion methods have improved the EOD performance considerably. However, the experimental results still showed that the paste extrusion performance varied from batch to batch due to variations in the paste properties. Thus, the control model parameters had to be re-tuned for each batch of paste. Also, for the same batch of paste being extruded using a constant plunger velocity, under-filling and over-filling of material were observed, indicating that the paste flow rate was inconsistent. The paste flow rate inconsistency for a constant plunger velocity is evidence of the inhomogeneity of the paste properties. Therefore, a more robust EOD method is required [70], [71].

1.3. FREEFORM EXTRUSION FABRICATION OF OVERHANGING FEATURES

The self-supporting capacity of the ceramics pastes allows for the fabrication of porous structures and some complex shapes without requiring the use of molds or

sacrificial support materials. However, as also occurs in other AM processes, under certain circumstances, e.g., creating large overhanging features, it is unavoidable to use a secondary support structure. In these cases, algorithms for calculating the support structure pattern and hardware allowing for the alternate printing of the two materials are needed. And, most importantly, a suitable secondary extrudable fugitive material is required. The support material extrudate must meet the typical requirements for a freeform extrusion fabrication pastes, namely, it must maintain its shape even under the load of overlying layers and be able to be extruded through fine deposition nozzles without clogging. Additionally, this support material must be chemically compatible with the colloidal paste of the main material, and easily removable in the post-processing steps, leaving no byproducts after removal. Finally, since these feedstocks are intended to be removed, it is preferable to formulate them from inexpensive materials, and they should be easy to prepare. Freeform extrusion fabrication of polymers, i.e., fused deposition modeling, has been applied in various fields, where complex geometries can be fabricated by using their well-developed support material systems [72]–[75]. However, very few studies can be found on investigating the self-supporting ability of ceramics extrudates and the development of support material systems for ceramics. A suitable solution has been proposed by Leu and Garcia [3] for the FEF process, where 10 vol. % methylcellulose and 90 vol. % water was mixed to form an extrudable support material. The methylcellulose solution worked well in subzero temperature in the FEF process [3]. However, it turned out to be unsuitable for a room temperature environment in the CODE process since the deposited solution can't be stiffened at room temperature, and was dragged by the moving nozzle.

1.4. FREEFORM EXTRUSION FABRICATION OF FUNCTIONALLY GRADED MATERIALS

Functionally graded materials (FGMs) are characterized by gradual changes in material compositions or structures over volumes. In recent years, a significant amount of research activity has taken place in FGM fabrication due to the promising potential of FGMs in many applications. It is generally understood that FGMs could bring unprecedented material design flexibility by allowing for localized performance optimization and a combination of properties not achievable in regular materials [76]–[79]. Conventional methods of fabricating FGMs are often subject to serious limitations on types of gradients and component geometries that can be created. Both issues are even more critical to ceramic-based FGMs, as ceramics are difficult to process with the use of traditional ceramic shaping technologies. Once ceramic FGMs are fabricated via pressing and sintering methods, it is almost impossible to perform secondary processes with them. Additive manufacturing (AM) could provide a feasible alternative in the fabrication of stepwise FGMs with maximum geometric flexibility. AM enables digital model-driven direct fabrication of structures on a voxel-to-voxel basis, therefore allowing for localized material compositional adjustment in principle [80]. Paste extrusion and ink jetting are the only feasible deposition methods for fabricating ceramic-based FGMs as the melting temperatures of ceramics are usually too high for thermal-based melt deposition [80]. The ink jetting-based AM processes are subject to high porosity (low density) due to the low solids loading, high binder concentration of the ink. Overall, freeform extrusion fabrication is the most favorable AM process for fabricating highly dense FGM components.

Alumina/zirconia (Al_2O_3/ZrO_2) FGM components have been of great interest, mainly to enhance the tensile strength and fracture toughness through the incorporation of the ZrO_2 phase. One practical application is the prosthetic hip joint ball, where the FGM realizes the transition from the tough ZrO_2 core, which provides the high strength of the joint structure, to the wear-resistance of the Al_2O_3 surface layer, which guarantees long service life [81], [82]. Because of the distinct sintering behavior and coefficient of thermal expansion (CTE) mismatch between alumina and zirconia, cracks and camber were present in many Al_2O_3/ZrO_2 composite specimens after processing as evident in the many studies [83]–[87]. Hillman et al. [85] found that sintering shrinkage mismatch results in cracks with large opening displacement (>30 µm), while thermal expansion mismatch causes cracks with a small opening displacement (<2 µm). To minimize the thermal stress, a large difference in thermal expansion characteristics, i.e., the material composition of adjacent layers, should be avoided. However, previous studies only investigated laminar FGM with large material composition steps, i.e., the low resolution of material composition variation. The interlayer steps used in laminated FGMs found from the literature ranged from 5-50 vol%, and the total number of layers was less than 10 when using finer (5%-10%) resolutions [82], [88]–[90]. The resolution and number of layers are probably limited by the redundant powder stacking or tape casting process, which requires a premixed feedstock with different a material composition for every distinct layer. Hence higher resolution will require increasing the number of premixed feedstocks and thus intensive workload. However, fine (<10%) material composition resolution can be readily achieved by freeform extrusion fabrication process. This opens

an opportunity to fabricate Al_2O_3/ZrO_2 FGM with lower residual stresses and investigate the effect of fine material grading step on the dimensional accuracy of the FGM part.

The first 3D ceramic FGM specimen was presented by Leu and Deuser [20] in 2012 using the FEF process, where Al_2O_3 and ZrO_2 were used as the constituents. A static mixer was used to blend the two constituents before they were deposited through the nozzle. Only relatively simple geometries were fabricated with a very rough material grading step (25 vol% per step). The large step in material composition was very likely to create large residual stresses during the sintering process, which may result in severe deformation or even cracking. However, the behavior of the FGM specimens in the sintering process was not presented in Leu and Deuser's work. An active mixing mechanism is desirable to blend the materials to produce homogeneous mixtures more efficiently than using a static mixer. Moreover, the deformation of the FGM specimens in the sintering process needs to be studied.

1.5. ORGANIZATION OF THE DISSERTATION

The background of this research was first presented in the introduction section, where a survey of existing research on freeform extrusion fabrication of ceramics was given. Based on the background, the study of this thesis was proposed with the main research objectives listed. Four published papers addressing the research objectives were included in this thesis.

The first paper investigated three EOD methods based on ram extruder, shutter valve, and auger extruder for extrusion of high solids loading (>50 vol.%) aqueous

ceramic pastes [71]. The extrusion precision of the three methods in terms of start and stop accuracy, as well as flow rate consistency, are compared and analyzed.

In the second paper, 3 mol% Y_2O_3 stabilized zirconia (3YSZ) specimens were fabricated using the CODE process [59]. Mechanical properties including density, Young's modulus, flexural strength, Weibull modulus, fracture toughness, and Vickers hardness of the sintered specimens were examined using ASTM standard test techniques. The grain size was measured using scanning electron microscopy.

The third paper focused on fabricating ceramic components that had external/internal features such as overhangs, bridges, and thus could not be fabricated without the use of support structures [63], [91]. The minimum angle of a slanted surface that can be fabricated using Al_2O_3 (alumina) paste without the need for a support structure was first determined. $CaCO_3$ was identified for building support structures, which decomposed during the sintering process and was then dissolved in water or acid. Sample parts were fabricated and evaluated to demonstrate the effectiveness of the sacrificial material as well as CODE's capability of fabricating geometrically complex parts.

In the fourth paper, a dynamic mixing mechanism was developed for mixing constituent ceramic pastes. FGM specimens with compositions graded between Al_2O_3 and ZrO_2 were fabricated and eventually densified by sintering [92]. Energy dispersive spectroscopy was used to compare final material compositions to the original material designs. The hardness at different locations on the specimens along the gradients was examined by micro-indentation tests. The dimensions of sintered specimens were measured, and the effects of material composition gradients on the distortion of sintered

FGM specimens were analyzed. A conclusion section is presented after the four papers to summarize the study of this thesis, and the recommendations for future work are given in the last section.

PAPER

I. EXTRUSION-ON-DEMAND METHODS FOR HIGH SOLIDS LOADING CERAMIC PASTE IN FREEFORM EXTRUSION FABRICATION

ABSTRACT

Fabrication of highly dense ceramic parts with complex geometries by paste extrusion-based solid freeform fabrication processes require precise control of the extrusion start and stop to dispense material on demand, which is often referred to as extrusion-on-demand (EOD). The EOD process for high solids loading pastes is difficult to control due to the paste's non-Newtonian behavior, compressibility, and inhomogeneity. In this study, three EOD methods based on ram extruder, shutter valve, and auger extruder are investigated for extrusion of high solids loading (>50 vol.%) aqueous ceramic pastes. The extrusion performance characteristics of the three methods in terms of start and stop accuracy, as well as flow rate consistency, are compared and analyzed. The results indicate that the auger extruder-based extrusion method has superior EOD performance and the highest flow rate consistency. Test parts were printed by using these methods and compared to validate this conclusion further.

1. INTRODUCTION

Freeform extrusion fabrication processes such as Robocasting [1]–[5], Contour Crafting [6]–[8], Fused Deposition of Ceramics [9]–[11], Freeze-Form Extrusion

Fabrication [12]–[14], Thermoplastic 3D Printing [15], and Ceramic On-Demand

Extrusion [16] deposit ceramic extrudate layer-by-layer through extrusion. Precise

control of the deposition flow rate is required to fabricate highly dense parts with

complex geometries. Inaccurate extrusion start and stop, as well as fluctuations in the

extrudate flow rate, lead to the formation of pores in parts, which is a common problem

in both filament-based and paste-based freeform extrusion fabrication processes [9], [10],

[14], [15]. Throughout the layer-by-layer deposition process, these defects will

accumulate and may eventually cause part failure or reduce the strength of the final part,

especially for freeform fabrication of brittle ceramic and glass materials [17]–[20].

Paste extrusion for freeform extrusion fabrication processes is typically

accomplished with a ram extruder, which is a positive placement extruder and consists of

a syringe and a plunger. Note that a pneumatic extruder is also used for freeform

extrusion fabrication. However, since it controls the extrusion flow rate only by

regulating the air pressure instead of piston velocity, its extrusion accuracy is not

comparable to a positive displacement extruder [21]. Thus it is not investigated and

compared to ram extrusion in this study. Based on ram extrusion, several methods

regulating the extrusion force and plunger velocity have been developed for the Freeze-

form Extrusion Fabrication (FEF) process. Zhao *et al.* (2010) [22] designed an adaptive

controller with a general tracking control law and implemented it to regulate the

extrusion force. Deuser *et al.* (2013) [23] developed a hybrid force/velocity controller to

regulate both the steady-state extrusion flow rate using a plunger velocity controller and

extrusion-on-demand using an extrusion force controller. Oakes *et al.* (2009) [24]

developed a dwell technique and a look-forward technique to compensate for the delay of

extrusion start and stop for improving Extrusion-On-Demand (EOD) performance. Zomorodi and Landers (2016) [25] developed a hierarchical model-based predictive control algorithm to systematically perform hybrid force-velocity control to extrude paste and draw consistent lines.

The previous efforts to develop ram extruder based extrusion methods have improved the EOD performance considerably. However, the experimental results still showed that the paste extrusion performance varied from batch to batch due to variations in the paste properties. Thus, the control model parameters had to be re-tuned for each batch of paste. Also, for the same batch of paste being extruded using a constant plunger velocity, under-filling and over-filling of material were observed, indicating that the paste flow rate was inconsistent. The paste flow rate inconsistency for a constant plunger velocity is evidence of the inhomogeneity of the paste properties. Therefore, a more robust EOD method is required.

In this paper, two extrusion mechanisms, i.e., shutter valve and auger extruder, which have been utilized in the dispensing industry [26], are investigated in comparison with ram extrusion for the freeform extrusion fabrication of ceramics. Extrusion performance characteristics in terms of start and stop accuracy, as well as flow rate consistency, are analyzed and compared for these three different EOD methods. Solid parts are also printed using the three EOD methods, and their properties are compared. Advantages and drawbacks of these three methods are discussed.

This study focuses on materials that are highly viscous, compressible and inhomogeneous. This type of materials is very common in paste/slurry based freeform extrusion fabrication. Since many researchers are working on freeform extrusion

fabrication and are facing the challenge of precise extrusion [15], [25], [27], it is of prime importance to study the extrusion of this particular type of material. While previous efforts on improving extrusion precision in freeform extrusion fabrication are all based on refining the control model of ram extrusion [22]–[25], [28], the present paper introduces a way of improving extrusion precision by comparing different paste extrusion mechanisms and using a proper control scheme for each mechanism. In addition, although the shutter valve and the auger extruder are described as having high dosing accuracy by their suppliers, no rigorous studies investigating their EOD performance and their flow rate consistency, especially for highly viscous, inhomogeneous materials, could be found.

2. CHALLENGES OF EXTRUSION-ON-DEMAND FOR HIGH SOLIDS LOADING PASTE

A schematic along with a photograph of the paste extrusion based material deposition is shown in Figure 1(a), where the machine used can be found in a previous article [22]. Li et al. (2013) [28] modeled the extrusion process by characterizing the ceramic paste viscosity using a modified Herschel–Bulkley model [31]. The steady-state relationship between the plunger velocity and the extrusion force was developed based on that viscosity model and the Navier–Stokes equation [32]. For pastes with different properties, the steady-state extrusion forces for the same plunger velocity were shown to be different. The influence of air in the paste was also examined. By regulating the plunger velocity using a general tracking controller [22], the plunger velocity reached its steady state very quickly (typically about 1 s). However, the extrusion force responded

slowly, reaching a steady-state value in several hundred seconds. Therefore, it took a long time to reach the steady-state extrudate velocity, i.e., steady-state paste flow rate. It was concluded that the large settling times of the extrusion force and extrudate velocity were mainly due to the air trapped in the paste [28], [29]. It should be noted that for a high solids loading paste, the degassing process in paste preparation is difficult due to the paste's high viscosity.
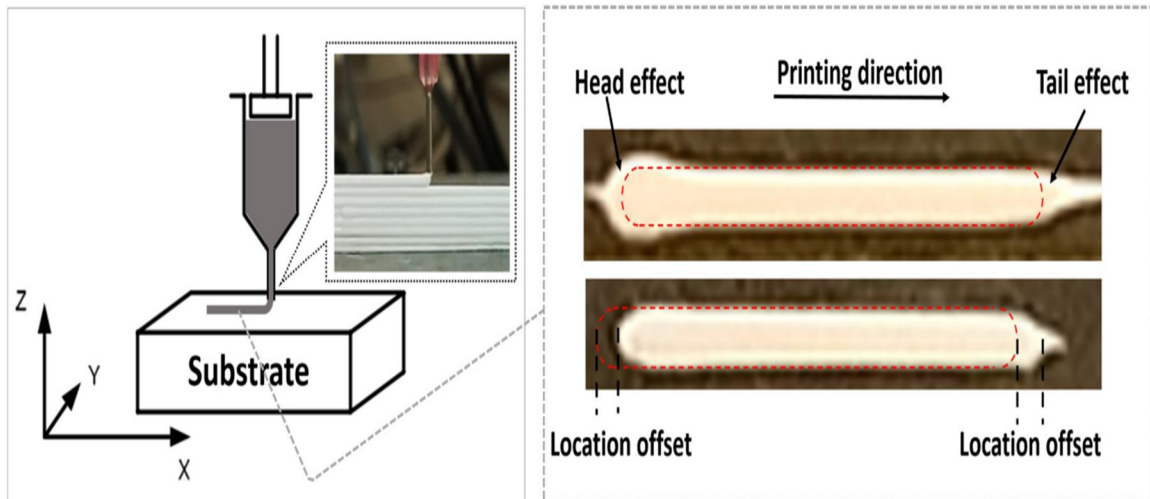
Figure 1. (a) Schematic of paste extrusion based material deposition, and (b) Schematic showing print flaws due to inaccurate extrusion start and stop, where the dashed lines indicate desired extrudate shapes and locations.

The hybrid force-velocity controller developed by Deuser *et al.* (2013) [23] was able to obtain a fast dynamic response of the extrusion force (typically with the settling time between 0.8 and 1.6 s) for the start and stop of extrusion using the extrusion force control. During the steady-state extrusion, the controller used the plunger velocity control. The dwell technique and the look-forward technique [24] were developed to compensate for the time delay in extrusion start and extrusion stop, respectively. These

techniques improved EOD performance considerably. However, the process parameters using a ram extruder must be tuned separately for different batches of paste to achieve high performance since different pastes have different rheological properties. Improper values of extrusion parameters will cause inaccurate extrusion start and stop, resulting in printing flaws. The white regions in Figure 1(b) are the actual printed lines, and the dash rounded rectangles represent the desired shapes and locations of printed lines. Excessive material extruded at the start of printing causes a large 'head' of the printed line, which will be termed 'head effect.' Ineffective stop of extrusion leaves a 'tail' at the end of the printed line, which will be termed 'tail effect.' The head and tail effects are shown in the upper image of Figure 1(b). The lower image in Figure 1(b) shows a printed line not deposited accurately at the desired location due to extrusion time delay, which will be termed 'location offset.'

Moreover, due to the paste's high solids loading, it is difficult to disperse the binder homogeneously during the paste preparation process and thus agglomerates form, causing paste inhomogeneity. Under-filling and over-filling of material were observed under constant velocity printing conditions, indicating inconsistent paste flow rate and providing evidence for paste inhomogeneity. Since the inhomogeneity of paste properties causes unpredictable disturbances to the ram extrusion process, we consider two other extrusion mechanisms, namely the shutter valve and the auger extruder, in this paper to improve EOD performance for the extrusion of high solids loading pastes, which are compressible and inhomogeneous.

3. DIFFERENT EXTRUSION METHODS

The paste extrusion process has two distinct phases: steady-state and transient. Steady-state extrusion occurs when a continuous filament is being printed at a constant extrusion rate. Transient extrusion occurs when the flow rate is changing, usually during the start and stop of extrusion. Both phases will be analyzed for each of the three extrusion methods. An overall description of the three extrusion mechanisms will be given below first.

3.1. OVERALL DESCRIPTION OF THE THREE EXTRUSION MECHANISMS

The ram extruder mechanism in Figure 2(a) consists of a ram-driven plunger and a syringe. The paste flow is regulated by controlling the plunger movement. It starts (or stops) extrusion by generating (or releasing) force on the plunger. Ram extruders are a widely used apparatus for paste extrusion [26], [33]. A shutter valve extrusion mechanism shown in Figure 2(b) has a plunger and syringe similar to the ram extruder mechanism, except that a shutter needle is added to the flow path as a valve. The shutter needle tip is close to the extrudate outlet. The needle is lifted or pressed down by an operating force, resulting in the opening and closing of the flow path. The extrusion flow rate is controlled by the plunger velocity or the force applied to the plunger, while the start and stop of extrusion are controlled by the motion of the shutter needle. Shutter valves are widely used in dispensing fluids such as solder paste, conductive epoxy, and adhesive for surface mounting and semiconductor packaging [26], [34]. The auger extruder mechanism shown in Figure 2(c) also uses a syringe; however, the pressure is

preloaded to the syringe by compressed air. This preloaded pressure is used for delivering the paste to the auger chamber, rather than for extrusion. Extrusion is achieved by rotating the auger using a servo motor. The flow rate is regulated by controlling the auger's angular velocity. The paste flow is stopped by stopping the auger rotation.
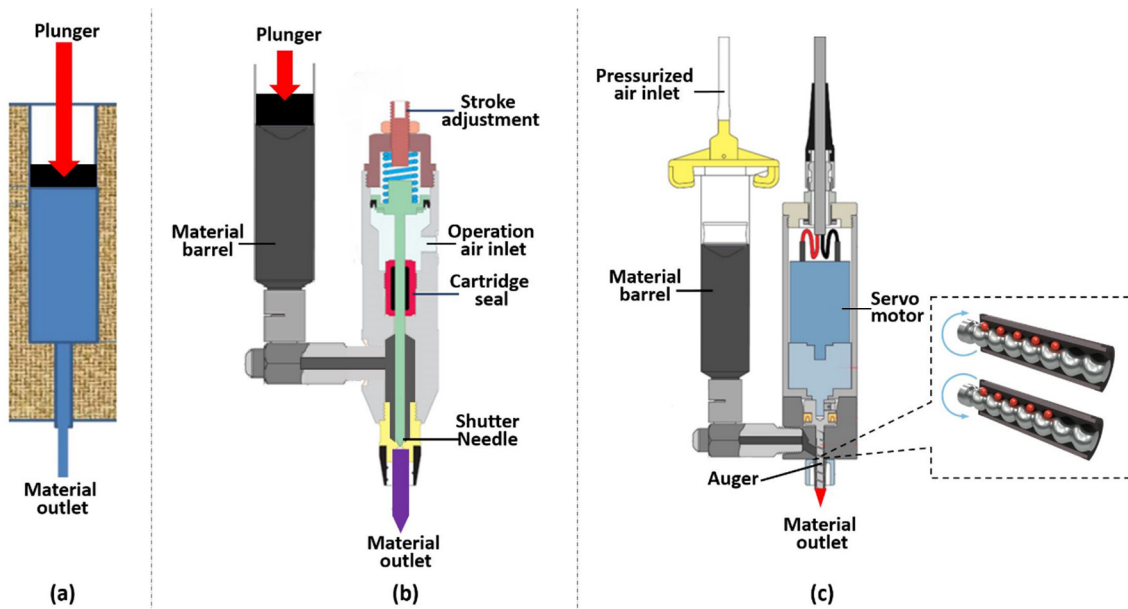
Figure 2. Schematic of three extrusion mechanisms: (a) Ram extruder (b) Shutter valve based extruder [27] (c) Auger extruder (EFD Inc. 2003, ViscoTec Inc. 2014).

Other extrusion mechanisms that work similarly to auger extruders are collectively referred to as 'progressive cavity pumps,' and they are also often referred to as auger pump, screw pump, etc. Auger/screw mechanisms are usually used in fluid dispensing when extra precision or an unlimited feedstock is needed [26], such as in micro-dosing and injection molding processes [35]. They are also used for powder deposition and metering [36] and have been used in extruding copper paste [27] and sulfur concrete [6] in solid freeform fabrication. However, no rigorous studies

investigating the auger extruder's EOD performance and flow rate consistency for inhomogeneous materials could be found. The auger extruder (eco-PEN 300, ViscoTec America Inc., Kennesaw, GA) used in this study consists of a helix metal rotor and an elastomeric stator. Several sealed cavities are formed between the rotor and stator, and they progress down or up when the rotor is turned, as shown in Figure 2(c). Each cavity has a known volume so that the specific volume extruded with each rotation can be determined. This type of auger extruder with a sealing stator is designed for precise micro-dispensing. Auger mechanisms which do not have sealing stators, such as large-scale screw extruders for plastic injection molding, are not included in the present study.

3.2. RAM EXTRUDER-BASED METHOD

For the ram extruder, the paste flow rate and the start and stop of extrusion are controlled by the plunger velocity and the force exerted by the plunger on the paste material. A general tracking controller has been developed and implemented to regulate the extrusion force and velocity [23]. Based on this controller, a hybrid extrusion force/velocity control was developed, which includes a plunger velocity control used to ensure a steady extrusion flow rate, and an extrusion force control to regulate the extrusion start and stop. The extrusion force control has a much shorter time constant than the plunger velocity control, and the hybrid control scheme switches from velocity control to force control when extrusion start or stop occurs.

The time constant of extrusion force control, although is shorter than that of the plunger velocity control, causes a delay at the start and stop of extrusion. Thus compensation is needed to start and stop extrusion accurately. A schematic of the ram

extruder based method is shown in Figure 3. To start extrusion, the gantry remains

stationary, i.e., dwelling for a short period after the force control is activated [24]. The

amount of this waiting time is called the start dwell time and is denoted τ (refer to Figure

3). To stop extrusion, the force control begins to decrease the extrusion force before the

extrusion nozzle reaches the end of the deposition path. The distance between the point

where the extrusion force starts to decrease, and the desired end of the filament is called

the early stop distance and is denoted d (refer to Figure 3).
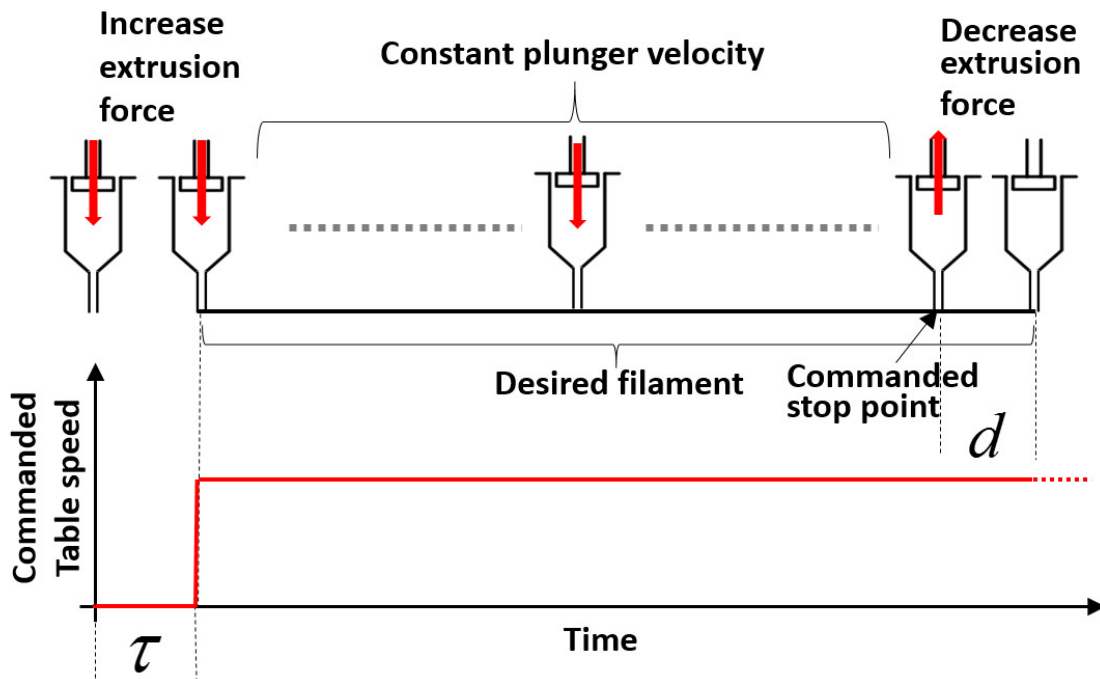
Figure 3. Schematic of ram extruder based method.

As discussed in the previous section, extrusion start and stop delays are caused by

paste compressibility due to the inevitable existence of air [29], [30]. The larger the

volume of paste being compressed and decompressed during the extrusion start and stop

process, the longer the time delay will be. As can be seen in Figure 2(a), the amount of

paste being compressed in the ram extruder is the volume of the entire syringe,

represented by the blue region in Figure 2(a), and is called the 'operation volume' in this

paper. The large operation volume (~ 55 ml when the syringe in this study is full) of the

ram extruder is the main reason for its less than satisfactory EOD performance.

3.3. SHUTTER VALVE BASED METHOD

Unlike the ram extruder based method, the start and stop of extrusion in the

shutter valve based method are controlled by the shutter, which opens and closes the flow

path. The hybrid extrusion force/velocity control described above is again implemented;

however, the control scheme is adjusted as follows. After the flow path is closed by the

shutter, instead of decreasing the force exerted on the plunger, the controller switches

from the plunger velocity control mode to the extrusion force control mode to maintain

the extrusion force so that the extrusion can be started instantaneously in the next start. It

should be noted that during the extrusion start and stop, the paste in the syringe is

compressed but is never decompressed; only the paste in the flow path from the shutter to

the material outlet will be compressed and decompressed. Then, the controller switches

back to the plunger velocity control mode for steady-state extrusion after the flow path is

opened in the next operation. For steady-state extrusion, this method is identical to the

ram extruder based method.

By using this method, since the extrusion stop is controlled by directly block the

flow path, a very fast stop is expected. On the other hand, the volume of paste being

compressed and decompressed during the extrusion start and stop, i.e., the operation

volume, is the volume of the flow path from the shutter to the material outlet, which is represented by the purple region in Figure 2(b). Since the operation volume (~ 0.2 ml for the shutter valve used in this study) is much smaller than that in the ram extruder based method, a much faster extrusion start is anticipated.

However, the time delay caused by the actuator such as the pneumatic shutter is inevitable and may not be negligible. To compensate for any delay of extrusion force and, thus of paste flow rate, the start dwell (τ) and early stop (d) strategies are still used in the shutter valve based method.

3.4. AUGER EXTRUDER BASED METHOD

When using an auger for paste extrusion, the paste flow rate is proportional to the auger's angular velocity. By maintaining a constant rotation speed of the motor that drives the auger, a constant extrusion flow rate is obtained. The start and stop of extrusion are achieved by turning the motor on and off. The syringe here is only for material storage and delivery; the paste material is only extruded by the auger in the auger chamber. Thus, by using the auger extruder based method, the operation volume during the extrusion start and stop is the volume from the auger chamber to the material outlet, which is represented by the red region in Figure 2(c). Since the operation volume (~ 0.1 ml for the auger extruder used in this study) is much smaller than that of the ram extruder based method, a much faster extrusion start and stop is anticipated. Again, in order to compensate for any time delay, the start dwell (τ) and early stop (d) strategies are also used in this method.

For a compressible paste, due to the paste inhomogeneity, the steady-state extrusion force changes during extrusion. For example, the steady-state extrusion force will decrease when a thinner portion of the paste is approaching the nozzle tip and being extruded out; it will increase when a thicker portion or a portion with some large agglomerates is coming out. In other words, the inhomogeneity of the paste properties brings disturbances to the steady-state extrusion process and introduces a transient phase, which is the cause of paste flow rate fluctuation observed when using the ram extruder based method. An effective way to alleviate the fluctuation is to have faster responses to these disturbances so that the system reaches its new steady state quickly once a disturbance is present.

A significant difference between the auger extruder based method and the other two methods is in the steady-state extrusion phase. The ram extruder and shutter valve based methods have large operation volumes during the steady-state extrusion (~ 50 ml, represented by the blue area in Figure 2(a), and dark grey area plus purple area in Figure 2(b), respectively), resulting in a slow dynamic response of the extrudate velocity and the slow fluctuation of paste flow rate when the corresponding steady-state extrusion force changes. Since the operation volume of the auger valve (represented by the red area in Figure 2(c)) is much smaller (~ 0.1 ml vs. ~50 ml), the dynamic response of extrudate velocity is much faster as compared to the other two methods. Therefore, a better flow rate consistency, i.e., less flow rate fluctuation, is expected by using this method compared to using the other two methods.

4. PASTE EXTRUSION EXPERIMENTS

In most extrusion-based freeform fabrication processes, the extrusion start and stop accuracy and flow rate consistency are the most important criteria for extrusion performance. Printing dash lines is an effective way to evaluate the extrusion start and stop accuracy, and printing continuous lines is an effective way to evaluate the paste flow rate consistency.

4.1. PASTE PREPARATION

The paste used in the extrusion experiments contained Al_2O_3 powder, DARVAN® C (Ammonium polymethacrylate, Vanderbilt Minerals LLC, Gouverneur, NY), Methocel (Methylcellulose, Dow Chemical Company, Pevely, MO) and deionized (DI) water. The Al_2O_3 powder, DARVAN® C and DI water were first mixed and ball-milled for 15 h to form a uniform slurry. DARVAN® C was used as a dispersant to balance the Van Der Waals forces between particles. The slurry was then heated up to 70°C and with Methocel dispersed in the slurry agitated by mechanical stirring for 10 min. Then, the slurry was cooled down to room temperature to form the paste. Mechanical stirring was also applied during the cooling down process. Methocel was used as a binder to increase paste viscosity and to assist in forming a stronger green body after drying [37]. Lastly, a vacuum mixer (Model F, Whip Mix Corp., Louisville, KY) was turned on for 10 min to remove air bubbles in the paste.

4.2. DASH LINE PRINTING

      Dash line printing tests were conducted for the three extrusion methods described

above. Location offset, tail effect, and head effect in printing dash lines are quantitative

measures of the accuracy of extrusion start and stop. Three groups of dash line printing

tests with different extrusion conditions listed in Table 1 were conducted. The reference

paste flow rate, table speed, and layer thickness were identical for the three extrusion

methods in each group. Optimal extrusion parameters for each EOD method including

start dwell (τ) and early stop distance (d) were experimentally calibrated for Group 1, i.e.,

for 610 μm diameter nozzle and 60% solids loading paste. The extrusion parameters were

calibrated by printing five dash line segments, changing τ by 10 ms and d by 0.1 mm and

repeat the printing tries until the best start and stop performance characteristics, i.e.,

having the least head and tail effects and location offset, were achieved. Table 2 lists the

values of the obtained τ and d values. Then, the same values of τ and d were applied to

Groups 2 and 3 in conducting dash line printing tests. The test results of Group 1 and

Group 2 were compared to examine the effects of changing nozzle diameter; the results

of Group 1 and Group 3 were compared to examine the effects of changing paste solids

loading.

Table 1. Extrusion conditions of three groups of dash line printing tests

	Group 1	Group 2	Group 3
Nozzle Diameter(μm)	610	406	610
Paste Solids Loading	60%	60%	50%

Table 2. Calibrated extrusion parameters for 610 μm diameter nozzle and 60% solids loading paste

Extrusion Conditions	Calibrated Extrusion Parameters	
	τ(ms)	d (mm)
Ram extruder	450	1.9
Shutter valve	70	0.3
Auger extruder	0	0

4.3. CONTINUOUS LINE PRINTING

A set of continuous line printing tests were conducted, and line width consistency was examined. A special cap was added to the nozzle tip to ensure consistent filament height by restricting the height of the deposited paste. The normal and modified nozzles, as well as their printing schematics, are shown in Figure 4. The filament height (h) was restricted to 150 μm. The reference plunger velocity for the ram extruder was 5 μm/s, which corresponds to a paste flow rate of 0.198 ml/min, and the table speed was set to 660 mm/min, which is a typical speed for this fabrication process. The filament height was set to 150 μm, which is smaller than the typical value of 450 μm, to obtain a larger nominal filament width and to reduce the filament width measuring error. By approximating the filament's cross-section geometry as a rectangle rounded at the two ends, as shown in Figure 4, the nominal filament width (w) of 2.02 mm was calculated.

As discussed in the previous section, the ram extruder based method and the shutter valve based method are essentially the same for continuous line printing (i.e., steady-state extrusion). Hence, the three extrusion methods were divided into two categories for the continuous line printing tests: the ram extruder/shutter valve based

method and the auger extruder based method. The shutter valve based method was chosen to represent the ram extruder/shutter valve category in this experiment. Under these two categories, four groups of dash line printing tests with the experimental conditions listed in Table 3 were conducted. Each group of tests was performed by printing five continuous serpentine lines using the same batch of 60% solids loading paste. Images of the continuous lines were taken, and the filament widths at 350 random sampling points were measured by an image processing software (ImageJ, National Institute of Health). The quality of the printed filament was evaluated statistically.
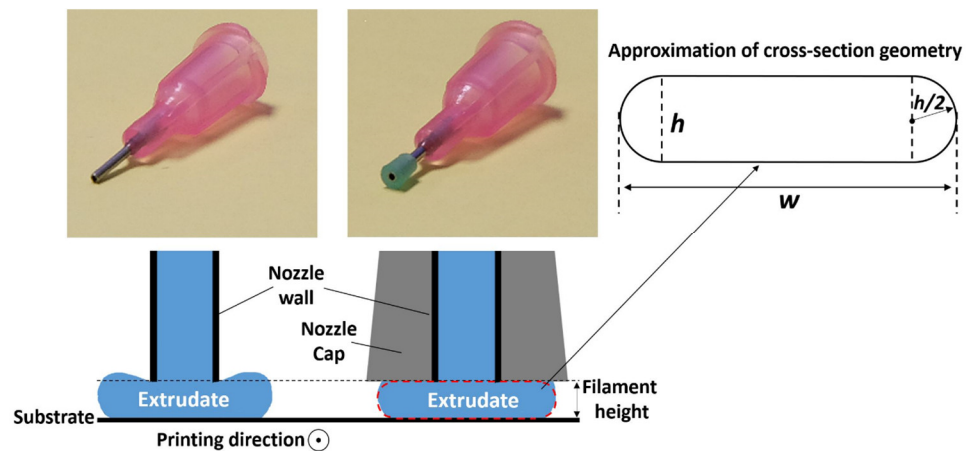
Figure 4. Normal nozzle (left) and nozzle with cap (right) and their printing schematics.

Table 3. Experimental conditions of the four groups of continuous line printing tests

	Group 1	Group 2	Group 3	Group 4
Nozzle Diameter (μm)	610	406	610	406
EOD method	Shutter valve	Shutter valve	Auger extruder	Auger extruder

4.4. SOLID PART PRINTING

In addition to the above line printing experiments, solid parts were fabricated in order to further examine the extrusion start and stop performance and flow rate consistency for the three EOD methods. Printing solid parts is less forgiving to material under-filling and over-filling compared to printing sparse-build parts such as scaffolds. When a solid part is printed, under-fillings will result in undesired pores, while over-fillings will result in accumulation of extra material and eventually the deposited material will interfere with the nozzle. Since the ram extruder based method and the shutter valve based method are essentially the same for continuous printing, only the shutter valve based method was chosen to compare with the auger extruder based method in the fabrication of solid parts.

Blocks with dimensions of $30 \times 15 \times 4 \text{ mm}^3$ were fabricated using the shutter valve and auger extruder based methods with the same gantry, same batch of paste, and identical process parameters which include paste flow rate: 280 μL/min, raster width: 600 μm, layer thickness: 400 μm, table speed: 21 mm/s, and nozzle diameter: 610 μm. Note that the reference plunger velocity of the shutter valve group was calculated from the reference paste flow rate, and the actual mean extrusion flow rate of the auger extruder based methods was calibrated to be close to the reference flow rate (280 μL/min) with less than 0.5% error before the experiment. Also, the parts were dried and sintered under the same conditions: 25 °C and 75% relative humidity for 20 h to dry the parts, and 1550 °C for 1.5 h to sinter them. The densities of the sintered blocks were measured by Archimedes' method [38].

5. RESULTS AND DISCUSSION

5.1. ACCURACY OF EXTRUSION START AND STOP

The results of the dashed line printing experiments were compared for the three

extrusion methods. In Figures 5 and 6, all the dash lines were printed from right to left,

and the dashed and solid vertical lines at the two ends represent the desired start and stop

points of lines segments, respectively. As shown in Table 2, the values of start dwell time

(τ) and early stop distance (d) in the shutter valve and auger extruder based methods are

smaller than those for the ram extruder based method, indicating a faster start and stop,

which validates the anticipation depicted in sections 3.2 and 3.3. The calibrated start

dwell time (τ) and early stop distance (d) for the shutter valve based method were

expected to be zero since the operation volume of shutter valve was negligible compared

to that of the ram extruder (0.2 ml vs. 55 ml). However, the obtained τ and d for the

shutter valve based method are 70 ms and 0.3 mm, respectively. This non-negligible time

delay is due to the pneumatic actuator of the shutter needle. Moreover, by examining

Figures 5 and 6, which contain the dash line segments printed by the shutter valve and

auger extruder based methods, we observe sharper tails than those by the ram extruder

based method, indicating more effective extrusion. By further examining Figure 5, the

dash line segments printed by the ram extruder method can be seen to have considerably

larger location offset when the nozzle diameter changes from 610 (left) to 406 μm (right),

indicating the 406 μm diameter nozzle performs worse than the 610 μm diameter nozzle.

Figure 6 shows the dash line segments printed by the ram extruder based method have

relatively larger heads when the paste solids loading changes from 60% to 50%,

indicating the 50% solids loading paste performs worse than the 60% solids loading paste. In contrast, the line segments printed by the shutter valve and auger extruder based methods kept consistent accuracy when changing the nozzle diameter and paste solids loading. Finally, the optimal extrusion process parameters for the ram extruder based method were experimentally calibrated for Groups 2 and 3, and the results are given in Table 4. It can be seen in this table that the values of the optimal extrusion parameters vary considerably with the change of nozzle diameter and paste solids loading.

Table 4. Ram extrusion parameters calibrated for different extrusion conditions

Group No.	Nozzle Diameter (μm)	Paste Solids Loading	Calibrated Extrusion Parameters	
			τ(ms)	d(mm)
1	610	60%	450	1.9
2	406	60%	650 (44%)*	2.2 (16%)
3	610	50%	300 (-33%)	1.3 (-32%)

* The numbers in parentheses are the percentage of the parameter variations as compared to the values of group 1, which was previously calibrated and listed in Table 1.
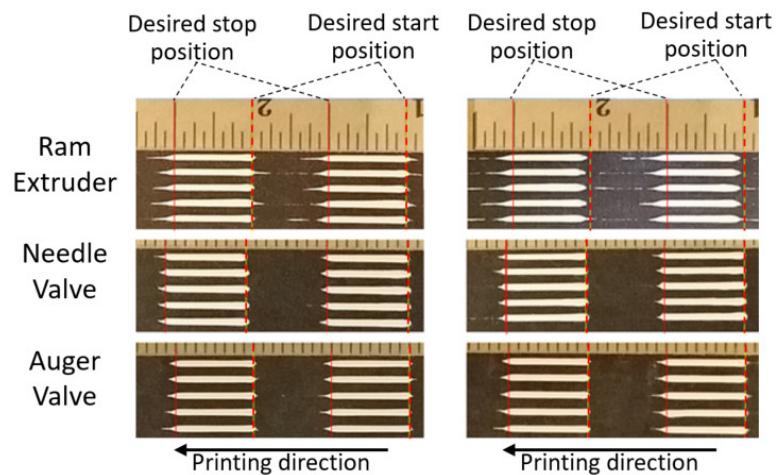
Figure 5. Dash line printing results for 610 μm diameter nozzle (left) and 406 μm diameter nozzle (right), with a paste solids loading of 60%.
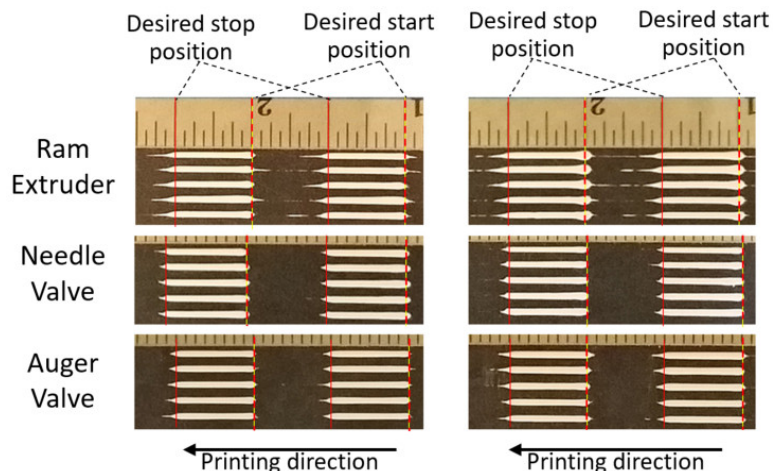
Figure 6. Dash line printing results for 60% solids loading paste (left) and 50% solids loading paste (right), with a nozzle diameter of 610 μm.

5.2. CONSISTENCY OF EXTRUDATE FLOW RATE

As discussed in section 3.3, the ram extruder based method and the shutter valve based method are essentially identical for continuous line printing. Hence the continuous line printing tests were conducted using only the shutter valve based method for both the ram extruder and shutter valve based methods. For the four groups in Table 3, five 1778 mm serpentine lines were printed for each group. In the images taken, a ruler was placed on the substrate to provide a dimensional scale. Figure 7 shows two images of typical printed serpentine lines using the shutter valve based method (left) and the auger extruder based method (right) with a 610 μm diameter nozzle. The substrate consists of a thick polymer tape sticking to a glass plate. As shown in Figure 7, the tape is inside the dashed rectangles. Since the region outside the tape is lower than that inside the tape, measurements were taken only in the areas inside the dashed rectangles to ensure a constant filament height, and also to avoid the transient effects near the corner turns.
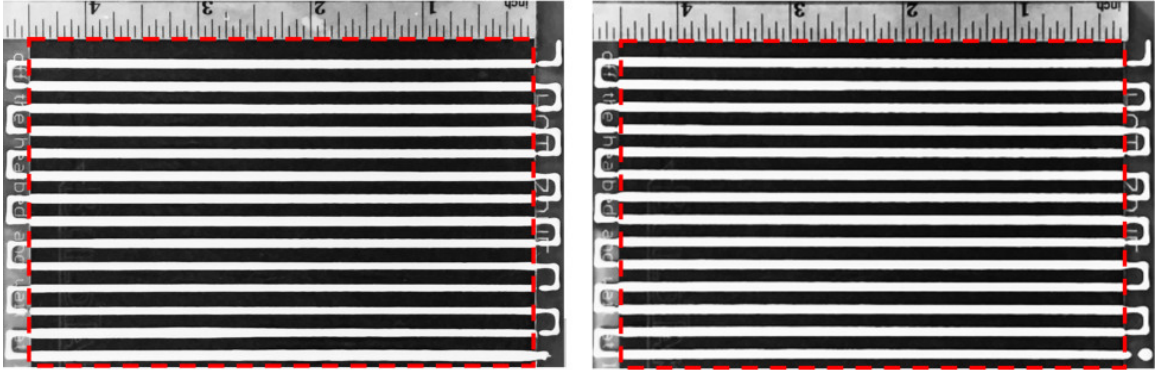
Figure 7. Images of continuous lines printed by shutter valve (left) and auger extruder (right) with 610 μm diameter nozzle. Both serpentine lines were printed from bottom right to top left.

A total of four groups of serpentines were measured, with each group containing five serpentine lines. Figure 7 shows two images taken from two of the four groups. A total of 70 measurements of line width were taken for each image. Hence a total of 350 measurements were taken for each group. The measured data are plotted in Figure 8, with Figure 8(a) for the two groups using a 610 μm diameter nozzle and Figure 8(b) using a 406 μm diameter nozzle. The line width measured from Figure 7 is plotted in Line 3 of Figure 8(a) using dash and solid curves, respectively, for lines printed using the shutter valve and using the auger extruder. The statistical results obtained from the continuous line printing experiments are given in Table 5. The differences between the mean values of line width and the corresponding nominal values are less than 3% for each group. However, the largest variation for the shutter valve groups is 41.6% vs. 7.9% for the auger extruder groups. The standard deviations of line width for the auger extruder groups are 0.09 and 0.07 mm, for 610 μm and 406 μm diameter nozzle, respectively, while the standard deviations of line width for the shutter valve groups are 0.22 and 0.24 mm, respectively. It should be noted that the larger (2.9%) mean value errors of the

auger extruder groups are due to the lack of self-calibration of the auger extruder controller, i.e., there existed an offset between the actual flow rate and the set flow rate appeared on the controller's interface. Also, note that for the solid part printing experiments, self-calibration was done before the experiment.

Table 5. Results of continuous line printing experiments. Numbers in parenthesis are percent difference from the nominal width of 2.02 mm.

| Group No. | Extrusion Condition | | Statistical Results of Printed Line Width | | | |
	EOD Method	Nozzle Dia. (μm)	Mean (mm)	Max. (mm)	Min. (mm)	Std. Dev. (mm)
1	Shutter valve	610	2.02 (0.0%)	2.55 (26.2%)	1.38 (-31.7%)	0.22
2	Shutter valve	406	2.00 (0.9%)	2.55 (26.2%)	1.18 (-41.6%)	0.24
3	Auger extruder	610	2.08 (2.9%)	2.20 (8.9%)	1.90 (-5.9%)	0.09
4	Auger extruder	406	2.08 (2.9%)	2.18 (7.9%)	1.90 (-5.9%)	0.07
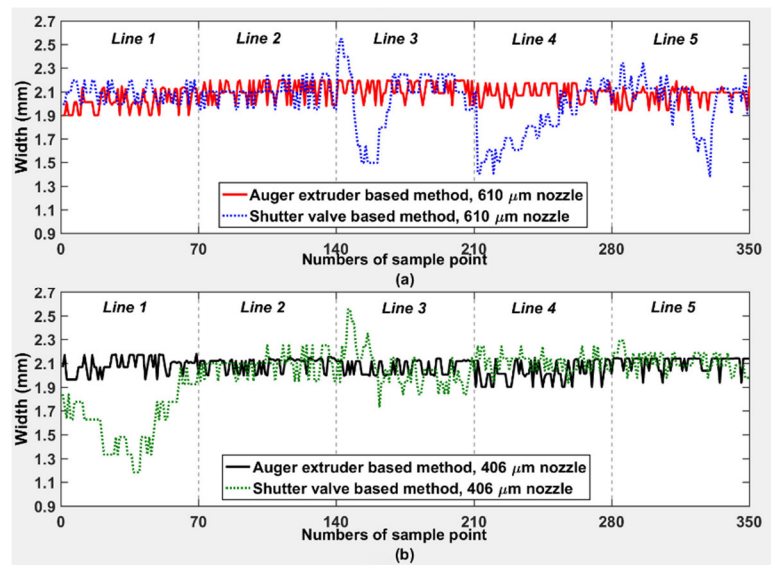
Figure 8. Line widths for continuous line printing experiments using two methods and two nozzle diameters (610 μm and 406 μm).

From Figure 8 and Table 5, we can see the larger fluctuation of paste flow rate in the shutter valve based method compared with the auger extruder based method. It can also be seen that for the shutter valve groups, in the printing of one serpentine line, there exist relatively large fluctuations in the line width which occur gradually in some of the sections. This indicates that the transient phases introduced by paste inhomogeneity disturbance have a slow response. A relatively stable flow rate is seen for the auger extruder groups, which validate the anticipated result as described in section 3.3, i.e., the auger extruder based method is less sensitive to the inhomogeneity of the compressible paste.

5.3. RELATIVE DENSITY OF SINTERED PARTS

The mean density measured for the blocks printed using the shutter valve based method was 96.2% of the theoretical density, and that of the blocks printed using the auger value based method was 98.4% of the theoretical density. Due to the simplicity of the part geometry and its tool path, there were no defects caused by extrusion starts and stops. The higher porosity for printed parts ($30 \times 15 \times 4$ mm^3) using the shutter valve based method was the result of internal pores caused by the material under-fillings due to variations in the widths of the printed lines. This provides further evidence that the auger extruder based extrusion method has better performance in terms of paste flow rate consistency than the shutter valve and ram extruder based extrusion methods. Three blocks printed using the auger extruder in green state are shown in Figure 9.
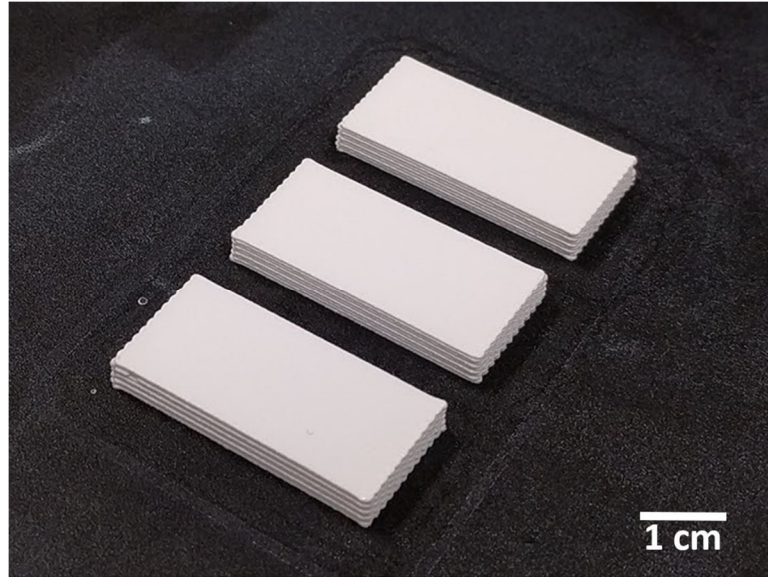
Figure 9. Three solid blocks (green state) printed using an auger extruder for density measurement.

5.4. FURTHER DISCUSSION ON AUGER EXTRUDER BASED METHOD

In addition to the extrusion precision discussed above, another important advantage of the auger extruder based method is its capability of continuous printing with a large volume of paste. By replacing the system's material barrel (see Figure 2) with a large paste reservoir and feeding the material with a pipe, the auger extruder based method can potentially print a paste continuously without the limitation of feedstock volume. Nevertheless, one disadvantage of the auger extruder based method is that the auger and seal rubber are susceptible to wear, especially in printing abrasive materials [6], [33], [39].

Based on the findings of this study and considering the other advantages and disadvantages of each extrusion method, tentative guidelines for choosing an extrusion mechanism for freeform extrusion fabrication are given below:

- In the cases that compact extruder size, high extrusion start and stop accuracy, great flow rate consistency, and unlimited feedstock volume are required, especially when the material lacks homogeneity, the auger extruder mechanism is suggested. An example is printing pore-free large ceramic parts. For extrusion of abrasive materials, however, the wear of auger will need to be considered.

- In the cases where large extruder size/weight is allowed, and high-precision control of extrusion start and stop for inhomogeneous materials is required, the shutter valve mechanism is suggested as a low-cost option.

- In the cases where the material is highly homogenous or incompressible, or the extrusion precision is not critical, the ram extruder mechanism is suggested due to its low cost and simplicity. Another case suitable for the ram extruder is when the material does not need to be much pressurized, such as in extruding with a large nozzle.

6. CONCLUSIONS

Extrusion-On-Demand methods based on ram extruder, shutter valve, and auger extruder have been presented and investigated for freeform extrusion fabrication of high solids loading ceramic pastes. The accuracy of extrusion start and stop, and consistency of paste flow rate was compared for these three methods by performing experiments that print dash and continuous lines. Also, the densities of the sintered ceramics parts were measured and compared for solid blocks printed using the different EOD methods. Advantages and disadvantages of each method were discussed, and tentative guidelines

for selecting the extrusion mechanism were given. Conclusions are drawn from the experimental results as follows:

- The shutter valve and auger extruder based methods exhibit much shorter time delays than the ram extruder based method for extrusion start and stop.

- The shutter valve and auger extruder based methods are more robust for accurate control of extrusion start and stop than the ram extruder based method. The calibrated control parameters for extrusion start and stop can be kept constant for different batches of paste and different nozzle diameters when using the shutter valve and auger extruder based methods. However, the ram extruder based method needs to adjust its control parameters for extrusion start and stop for different paste solids loading and nozzle diameter.

- The auger extruder based method is more robust for continuous printing than the ram extruder and shutter valve based methods. For a constant set extrusion rate, the auger extruder based method have higher consistency in the printed line width than the other two methods.

- The sintered solid ceramic parts printed using the auger extruder based method have a higher density than the part densities obtained using ram extruder and shutter valve based methods.

ACKNOWLEDGMENTS

REFERENCES

[1]   J. Cesarano *et al.*, "Customization of load-bearing hydroxyapatite lattice scaffolds," *Int. J. Appl. Ceram. Technol.*, vol. 2, no. 3, pp. 212–220, 2005.

[2]   J. Cesarano, R. Segalman, and P. Calvert, "Robocasting provides moldless fabrication from slurry deposition," *Ceram. Ind.*, vol. 148, no. 4, p. 94, 1998.

[3]   P. Miranda, E. Saiz, K. Gryn, and A. P. Tomsia, "Sintering and robocasting of β-tricalcium phosphate scaffolds for orthopaedic applications," *Acta Biomater.*, vol. 2, no. 4, pp. 457–466, 2006.

[4]   S. L. Morissette, J. a Lewis, J. Cesarano, D. B. Dimos, and T. Y. Baer, "Solid freeform fabrication of aqueous alumina-poly(vinyl alcohol) gelcasting suspensions," *J. Am. Ceram. Soc.*, vol. 83, no. 10, pp. 2409–2416, 2000.

[5]   J. N. Stuecker, J. Cesarano, and D. A. Hirschfeld, "Control of the viscous behavior of highly concentrated mullite suspensions for robocasting," *J. Mater. Process. Technol.*, vol. 142, no. 2, pp. 318–325, 2003.

[6]   B. Khoshnevis, X. Yuan, B. Zahiri, J. Zhang, and B. Xia, "Construction by Contour Crafting using sulfur concrete with planetary applications," *Rapid Prototyp. J.*, vol. 22, no. 5, pp. 848–856, 2016.

[7]   B. Khoshnevis, X. YUAN, B. Zahiri, J. Zhang, and B. Xia, "Deformation Analysis of Sulfur Concrete Structures Made by Contour Crafting," *AIAA Sp. 2015 Conf. Expo.*, 2015.

[8]   H. K. Kwon and K. S. Kim, "Effect of Orifice Shape in Contour Crafting with Ceramic Material: A Simulation for Extrusion and Deposition Mechanism," *Adv. Mater. Res.*, vol. 26–28, pp. 953–956, 2007.

[9]   M. K. Agarwala *et al.*, "FDC, rapid fabrication of structural components," *Am. Ceram. Soc. Bull.*, vol. 75, no. 11, pp. 60–66, 1996.

[10]   R. Clancy *et al.*, "Fused deposition of ceramics : progress towards a robust and controlled process for commercialization," in *Proceedings of the 8th Annual International Solid Freeform Fabrication Symposium*, 1997, pp. 185–194.

[11] G. M. Lous, I. A. Cornejo, T. F. McNulty, A. Safari, and S. C. Danforth, "Fabrication of piezoelectric ceramic/polymer composite transducers using fused deposition of ceramics," *J. Am. Ceram. Soc.*, vol. 83, no. 1, pp. 124–128, 2000.

[12] M. S. Mason, T. Huang, R. G. Landers, M. C. Leu, and G. E. Hilmas, "Freeform extrusion of high solids loading ceramic slurries, part I: extrusion process modeling," in *Proceedings of the 17th Annual International Solid Freeform Fabrication Symposium*, 2006, pp. 316–328.

[13] M. C. Leu *et al.*, "Freeze-Form Extrusion Fabrication of composite structures," in *Proceedings of the 22nd Annual International Solid Freeform Fabrication Symposium*, 2011, pp. 111–124.

[14] T. Huang, M. S. Mason, G. E. Hilmas, and M. C. Leu, "Freeze-form Extrusion Fabrication of ceramic parts," *Virtual Phys. Prototyp.*, vol. 1, no. 2, pp. 93–100, 2006.

[15] U. Scheithauer, E. Schwarzer, H. J. Richter, and T. Moritz, "Thermoplastic 3D printing - an additive manufacturing method for producing dense ceramics," *Int. J. Appl. Ceram. Technol.*, vol. 12, no. 1, pp. 26–31, 2015.

[16] A. Ghazanfari, W. Li, M. C. Leu, and G. E. Hilmas, "A novel extrusion-based additive manufacturing process for ceramic parts," in *Proceedings of the 27th Annual International Solid Freeform Fabrication Symposium*, 2016, pp. 1509–1529.

[17] J. Luo *et al.*, "Solid freeform fabrication of transparent fused quartz using a filament fed process," in *Proceedings of the 26th Annual International Solid Freeform Fabrication Symposium*, 2015, pp. 122–133.

[18] J. Luo *et al.*, "Bubble formation in additive manufacturing of glass," in *Proceedings of SPIE 9822, Advanced Optics for Defense Application*, 2016, vol. 9822, pp. 982214–982216.

[19] J. Luo *et al.*, "Wire-Fed additive manufacturing of transparent glass parts," in *Proceedings of the ASME 2015 International Manufacturing Science and Engineering Conference*, 2015, vol. 1, p. V001T02A108.

[20] J. Luo, H. Pan, and E. C. Kinzel, "Additive manufacturing of glass," *J. Manuf. Sci. Eng.*, vol. 136, no. 6, p. 061024, 2014.

[21] L. Jianping and D. Guiling, "Technology development and basic theory study of fluid dispensing - a review," in *High Density Microsystem Design and Packaging and Component Failure Analysis, 2004. HDP '04. Proceeding of the Sixth IEEE CPMT Conference on*, 2004, pp. 198–205.

[22] X. Zhao, R. G. Landers, and M. C. Leu, "Adaptive extrusion force control of Freeze-form Extrusion Fabrication processes," *J. Manuf. Sci. Eng.*, vol. 132, no. 6, p. 064504, 2010.

[23] B. K. Deuser, L. Tang, R. G. Landers, M. C. Leu, and G. E. Hilmas, "Hybrid extrusion force-velocity control using Freeze-Form Extrusion Fabrication for functionally graded material parts," *J. Manuf. Sci. Eng.*, vol. 135, no. 4, p. 041015, 2013.

[24] T. Oakes, P. Kulkarni, R. G. Landers, and M. C. Leu, "Development of Extrusion-On-Demand for ceramic Freeze-Form Extrusion Fabrication," in *Proceedings of the 20th Annual International Solid Freeform Fabrication Symposium*, 2009, pp. 206–218.

[25] H. Zomorodi and R. G. Landers, "Extrusion based additive manufacturing using explicit model predictive control," in *Proceedings of the 2016 American Control Conference*, 2016, pp. 1747–1752.

[26] L. Jianping and D. Guiling, "Technology development and basic theory study of fluid dispensing - a review," *High Density Microsyst. Des. Packag. Compon. Fail. Anal. 2004. HDP '04. Proceeding Sixth IEEE CPMT Conf.*, pp. 198–205, 2004.

[27] S. Hong, C. Sanchez, H. Du, and N. Kim, "Fabrication of 3D printed metal structures by use of high-viscosity Cu paste and a screw Extruder," *J. Electron. Mater.*, vol. 44, no. 3, pp. 836–841, 2015.

[28] M. Li, L. Tang, R. G. Landers, and M. C. Leu, "Extrusion process modeling for aqueous-based ceramic pastes, part 2: experimental verification," *J. Manuf. Sci. Eng.*, vol. 135, no. October 2013, p. 051009, 2013.

[29] M. Li, L. Tang, R. G. Landers, and M. C. Leu, "Extrusion process modeling for aqueous-based ceramic pastes—part 1: constitutive model," *J. Manuf. Sci. Eng.*, vol. 135, no. 5, p. 51008, 2013.

[30] M. Li, L. Tang, R. G. Landers, and M. C. Leu, "Extrusion process modeling for aqueous-based ceramic pastes—part 2: experimental verification," *J. Manuf. Sci. Eng.*, vol. 135, no. 5, p. 051009, 2013.

[31] W. Herschel and R. Bulkley, "Measurement of consistency as applied to rubber benzene solutions," *Proc. Am. Soc. Test. Mater.*, vol. 26, no. 82, pp. 621–629, 1926.

[32] R. Temam, *Navier-stokes equations*, vol. 2. Amsterdam: North-Holland, 1984.

[33] J. Benbow and J. Bridgewater, *Paste flow and extrusion*. Oxford: Clarendon Press, 1993.

[34]   Nordson Corporation, "741V needle valve system for precise, consistent fluid control," 2010. [Online]. Available: http://pdf.directindustry.com/pdf/nordson-efd/741v-needle-valve/35688-657310.html. [Accessed: 17-Feb-2017].

[35]   D. M. Bryce, *Plastic injection molding: manufacturing process fundamentals*. Dearborn, MI: Society of Manufacturing Engineers, 1996.

[36]   S. Yang and J. R. G. Evans, "Metering and dispensing of powder; the quest for new solid freeforming techniques," *Powder Technology*, vol. 178, no. 1. pp. 56–72, 2007.

[37]   J. Li, "An experimental study of fabrication temperature effect on aqueous extrusion freeform fabrication," Missouri University of Science and Technology, 2014.

[38]   ASTM C373, "Standard Test Method for Water Absorption, Bulk Density, Apparent Porosity, and Apparent Specific Gravity of Fired Whiteware Products, Ceramic Tiles, and Glass Tiles." ASTM International, West Conshohocken, PA, 2014.

[39]   ViscoTec Inc., "Micro dispensing in perfection," 2014. [Online]. Available: https://www.viscotec.de/media/preeflow_brochure_2014.pdf. [Accessed: 17-Feb-2017].

[40]   EFD Inc., "Auger valve dispensing," 2003. [Online]. Available: http://www.smtnet.com/library/files/upload/EFD__Auger_Valve_Dispensing.pdf. [Accessed: 17-Feb-2017].

II. CHARACTERIZATION OF ZIRCONIA SPECIMENS FABRICATED BY CERAMIC ON-DEMAND EXTRUSION

ABSTRACT

The Ceramic On-Demand Extrusion (CODE) process is a novel additive manufacturing method for fabricating dense (~99% of theoretical density) ceramic components from aqueous, high solids loading pastes (>50 vol.%). In this study, 3 mol% Y_2O_3 stabilized zirconia (3YSZ) specimens were fabricated using the CODE process. The specimens were then dried in a humidity-controlled environmental chamber and afterward sintered under atmospheric conditions. Mechanical properties of the sintered specimens were examined using ASTM standard test techniques, including density, Young's modulus, flexural strength, Weibull modulus, fracture toughness, and Vickers hardness. The microstructure was analyzed, and grain size measured using scanning electron microscopy. The results were compared with those from Direct Inkjet Printing, Selective Laser Sintering, Lithography-based Ceramic Manufacturing (LCM), and other extrusion-based processes, and indicated that zirconia specimens produced by CODE exhibit superior mechanical properties among the additive manufacturing processes. Several sample components were produced to demonstrate the CODE's capability for fabricating geometrically complex ceramic components, and the surface roughness of these components was examined.

1. INTRODUCTION

Zirconia ceramics, especially 3Y-TZP (3 mol% Y_2O_3 stabilized tetragonal zirconia polycrystal), are important structural ceramic materials due to the superior mechanical properties resulting from the transformation toughening mechanism [1]. Additive manufacturing provides the capability of producing components with high geometrical complexity. However, most ceramic additive manufacturing processes exhibit less than satisfactory mechanical properties due to residual porosity in the final products, a result of additive manufacturing processes, and the flaw-sensitive nature of ceramic materials. Thus, pursuing mechanical properties equal to those of more traditional processing methods is a challenge for ceramic additive manufacturing.

The Ceramic On-Demand Extrusion (CODE) technique is a novel, extrusion-based, additive manufacturing (AM) process, which produces dense (~99% of theoretical density) ceramic components after sintering. It deposits high solids loading (>50 vol%) aqueous ceramic pastes onto a substrate, layer-by-layer, at room temperature. Each deposited layer is solidified by uniform infrared radiation drying from the top surface. At the same time, the undesirable water evaporation from the side of the part is prohibited by surrounding the part with liquid [2,3]. This layered uniform radiation drying approach eliminates the water content gradient in the fabricated part and thus enables the CODE process to produce crack-free ceramic parts. The progressive cavity pump based extruder utilized in CODE guarantees a precise Extrusion On-Demand (EOD) control with a consistent deposition flow rate to avoid pores in the part [4], which further improves the density of the as-printed part.

In the work described in the present paper, the CODE process was used to fabricate 3YSZ specimens, and the mechanical properties and microstructure of these specimens were evaluated and compared with those fabricated by other processes. For demonstration, several geometrically complex parts made of 3Y-TZP were fabricated using CODE, and their surface finish was examined.

2. EXPERIMENTAL PROCEDURE

2.1. PASTE PREPARATION

The aqueous zirconia paste was made of a commercially available 3 mol% yttria-stabilized zirconia (3YSZ) powder (TZ-3Y-E, Tosoh USA, Inc., Grove City, OH, USA), distilled water, dispersant (Dolapix CE 64, Zschimmer & Schwarz GmbH, Lahnstein, Germany), and ammonium hydroxide solution (221228, Sigma Aldrich, St. Louis, MO, USA) for pH adjustment. The zirconia powder had an average particle size of 40 nm and a surface area of 16 m^2/g, according to the manufacturer.

Batches of ceramic paste were produced at approximately 50 vol% solids loading by dispersing 3YSZ powder in distilled water using 5 wt% dispersant. The pH was adjusted using the ammonium hydroxide solution until an alkaline pH $\approx$ 9-10 was achieved, as measured by a pH meter (HI 2210, Hannah Instruments, Woonsocket, RI, USA). The solid particles were added slowly and mixed. All mixing was performed using a whip mixer (Model F, Whip Mix, Louisville, KY, USA) while pulling a mild vacuum (~20 kPa) during discrete mixing steps to aid in deaeration, until all solids were added.

The paste was then stirred for an additional five minutes under vacuum to homogenize the paste.

2.2. PART BUILDING PROCESS

The zirconia paste was extruded at controlled flow rates through a circular nozzle. While the nozzle moved under the control of G&M codes, the extruded material was deposited on a substrate located in a tank designed to hold a fluid medium. Once the deposition of each layer was completed, oil was pumped into the tank surrounding the layer to prevent undesirable water evaporation from the sides of the deposited layers. A mineral oil (Florasense Lamp Oil, MVP Group International Inc., Charleston, SC, USA) was chosen as the fluid surrounding the part to preclude interaction between the fluid and the aqueous paste. The level of oil was controlled so that it was maintained at a level typically 0.4 mm (thickness of one layer) below the top surface of the part being fabricated. Infrared radiation was then applied to uniformly dry the deposited layer from its top so that the part being fabricated would maintain its shape while subsequent layers were deposited. By repeating the above steps, the component was fabricated layer-by-layer. A schematic of the process is shown in Figure 1. The layered uniform radiation drying, together with the prohibition of undesirable evaporation from the sides of the part, enables rapid solidification of each layer without causing moisture gradients in the part, thus preventing part cracking and warpage. The remaining water content and oil on the part surface was eliminated through bulk drying during post-processing.
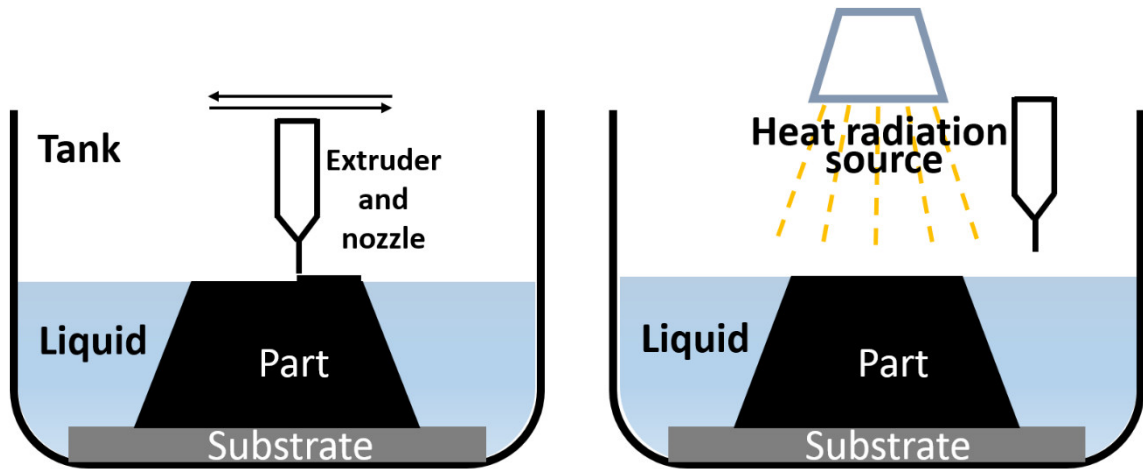
Figure 1. Schematic of the part building process of CODE.

In this study, 24 beams with dimensions of 6 mm × 25 mm × 4 mm (width × length × height, based on a CAD model), and 5 blocks with dimensions of 53.2 mm × 53.2 mm × 6.4 mm (width × length × height, based on a CAD model) were printed for property evaluation.

2.3. POST PROCESSING

Once the parts were built and removed from the tank, the remaining water content in the parts, and the oil on the surface of the parts were eliminated by bulk-drying to obtain "green" parts. The bulk-drying was performed in an environmental chamber where the relative humidity and temperature were controlled to 75% and 25°C, respectively, for 20 hours. The high humidity in the chamber slowed down the drying rate to avoid part warpage and crack formation. The green parts were then sintered in an electric furnace (DT-29-RSA, Deltech, Denver, CO) under atmospheric pressure to obtain the final parts.

In order to determine an appropriate sintering temperature and time, a sintering study was performed on the zirconia beams. The 24 "green" beams were divided into eight groups and sintered under eight different sintering conditions. The eight groups of sintered specimens were then tested to compare their density, hardness and fracture toughness. The best sintering condition among the eight groups was determined through comparison of these properties. The 5 "green" zirconia block specimens were then sintered using these selected conditions.

2.4. CHARACTERIZATION

The density of sintered specimens was determined by Archimedes' method [5]. The dry mass of each specimen was measured first. Then, the specimens were saturated by submerging in distilled water and placing them under vacuum for 12 h. The saturated and suspended masses were then recorded to calculate the bulk density. This value was divided by the theoretical density (T.D.) of 3Y-TZP (6.056 g/cm^3 [6,7]) to obtain the average relative density of the specimen.

Vickers hardness was measured according to ASTM C1327 [8] using a microhardness tester (V-100-V2, LECO, Saint Joseph, MI, USA). The applied force was 98.07 N for 10 seconds. The test surfaces of specimens were polished using successively finer diamond abrasives down to 0.25 μm prior to indentation.

For the 24 sintered beams, fracture toughness was estimated from the indentation test using Anstis' method [9]. For the blocks sintered at the selected final sintering condition, fracture toughness was determined by testing Chevron-Notched (CN) beams in four-point bending using a fully articulating test fixture for configuration A (L=50 mm,

B=3 mm, W=4 mm, and a_0=0.8 mm) according to ASTM C1421 [10]. Test bars were cut out from the block specimens and ground to standard size using an automated surface grinder (Chevalier, FSG-3A818, Santa Fe Springs, CA, USA). A dicing saw (Accu-cut 5200, Aremco Products, Ossining, NY, USA) with a 0.15 mm-thick diamond wafering blade was then used to machine the chevron notches on each test bar. An instrumented load frame (Instron 5881, Instron Corporation, Norwood, MA, USA) was used to test the CN beams with a crosshead velocity of 0.2 mm/min. The dimensions of chevron notches were then measured using an optical microscope (KH-3000, Hirox, Hackensack, NJ, USA).

Flexural strength was measured by the four-point bending method according to ASTM C1161 [11] using an instrumented load frame (5881, Instron Corporation, Norwood, MA, USA) with a crosshead velocity of 0.2 mm/min. Both A-size (2 mm × 1.5 mm × 25 mm) and B-size (4 mm × 3 mm × 45 mm) beam specimens were prepared and tested. From the five sintered blocks, 30 A-size specimens and 30 B-size specimens were cut. All four surfaces of each specimen were ground using a 600-grit diamond wheel, and then manually chamfered using a 1200-grit diamond grinding disk. Young's modulus was determined from Euler-Bernoulli beam theory [12] using the readings of the deflectometer (a linear variable differential transformer) on the load frame which measured the deflection at the center of the test beam during the bending test (see [13] for detailed calculation procedure).

Microstructural analysis was performed using scanning electron microscopy (SEM) (Helios Nanolab 600, FEI, OR, USA). Prior to SEM imaging, the specimen was first polished down to a 0.25-micron finish using successively finer diamond abrasive

slurries, then thermally etched at 1350°C for 0.5 h to reveal the grain boundaries. The average grain size was measured by the linear intercept length method [14] in ImageJ [15], an open-source image processing software.

3. RESULTS AND DISCUSSION

3.1. STUDY OF SINTERING CONDITIONS

The 24 beam specimens were divided into 8 groups, each group having 3 specimens, and sintered at 8 different sintering conditions, i.e., different temperatures (T) and hold times (t). The relative density (D) and Vickers hardness (HV) were measured, and the fracture toughness (K_{IC}) was estimated from the indentation test for each group of specimens. The average bulk density of each group was measured from 3 specimens. The hardness was measured from a total of 6 indentations across three specimens, with two on each specimen. The fracture toughness was then calculated according to Equation (1) from the six indentations using

$$K_{IC} = \varphi(E/H)^{1/2} P/c^{3/2} \tag{1}$$

where φ is a constant (0.016) [16,17], H is the hardness (GPa), P is the applied load (N), E is Young's modulus (GPa), and c is the crack half-length (m), which is the diagonal length of the indent plus the two crack lengths, divided by 2 (see Figure 2). The Young's modulus (E) assumed in Equation (1) was 210 GPa, which is a commonly used value in most of the fracture toughness tests for 3Y-TZP[17–19], and it will be updated in future sections (section 3.5) once actual E values were measured. The applied load was 98.07

N. The average results, as well as the standard deviations measured from the eight groups, are given in Table 1.

Table 1. Density (D), hardness (HV) and fracture toughness (K_{Ic}) results of 8 sintered groups; T is the sintering temperature, and t is the sintering duration.

	T (°C)	t (h)	D (%)	HV (GPa)	K_{Ic} (MPa·m$^{0.5}$)
Group 1	1350	1	99.11 (0.31)	14.2 (0.19)	3.5 (0.04)
Group 2	1350	2	99.52 (0.01)	14.1 (0.09)	3.5 (0.05)
Group 3	1450	0.5	99.47 (0.07)	13.9 (0.21)	3.7 (0.09)
Group 4	1450	1	99.32 (0.13)	13.7 (0.16)	3.8 (0.07)
Group 5	1500	0.5	99.22 (0.22)	13.8 (0.24)	3.8 (0.14)
Group 6	1500	1	99.13 (0.12)	13.8 (0.12)	3.7 (0.06)
Group 7	1550	0.5	99.09 (0.04)	13.4 (0.35)	4.0 (0.07)
Group 8	1550	1	99.16 (0.09)	13.1 (0.14)	4.3 (0.08)

Note: Values in parentheses represent the standard deviation.
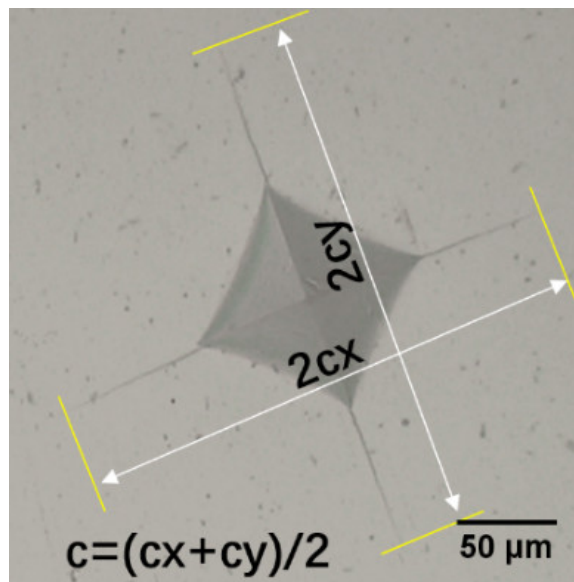
Figure 2. Micrograph of a Vickers indent and cracks.

According to Table 1, all groups had a density above 99% of the theoretical density. Group 2 (sintering at 1350°C for 2 h) reached a maximum density of 99.5%, while group 8 (sintering at 1550 °C for 1 h) had the highest fracture toughness (4.3 MPa·m$^{0.5}$). Although it exhibited the lowest hardness, the sintering condition for group 8 was chosen to move forward since it resulted in the highest fracture toughness, which is more desirable for 3Y-TZP than hardness.

3.2. SHRINKAGE

The five block specimens were subsequently sintered at the selected sintering condition (1550 °C, 1 h). Figure 3 illustrates one of the five sintered block specimens. The printing parameters for all specimens are also listed in this figure. The part dimensions were measured by a Vernier caliper at different stages, i.e., after bulk drying and after sintering. For each specimen, at each stage, six measurements were taken for each dimension (W, L, and H). Hence a total of 30 measurements were obtained from 5 specimens for each dimension. The mean value of the 30 measurements is reported in Table 2, as well as the amount of shrinkage. Compared to the wet (as-printed) specimens, the dried specimens had 1.5%, 1.2% and 2.2% reduction in width, length, and height, respectively, corresponding a volumetric shrinkage of 4.8%. The sintered specimens had 20.2%, 20.0% and 21.6% reduction in width, length, and height, respectively, compared to the as-printed specimens. This corresponds to a 50.0% volumetric shrinkage. The shrinkage rate in the length and width directions during both drying and sintering stages were slightly lower than that in the height direction. The cause of this anisotropy is hypothesized to be the friction between the specimen and the substrate, i.e., the friction

hinders the particles from moving in the longitudinal and transverse directions of the specimens, while the friction is absent in the vertical direction. However, further evidence is needed to validate this hypothesis.

Table 2. The average amount of shrinkage of the block specimens.

	Dimensions (mm)	Linear shrinkage (%)	Volumetric shrinkage (%)
As-printed	53.2×53.2×6.4	--	--
Dried	52.4×52.4×6.3	1.5×1.2×2.2	4.8
Sintered	42.4×42.5×5.0	20.2×20.0×21.6	50.0
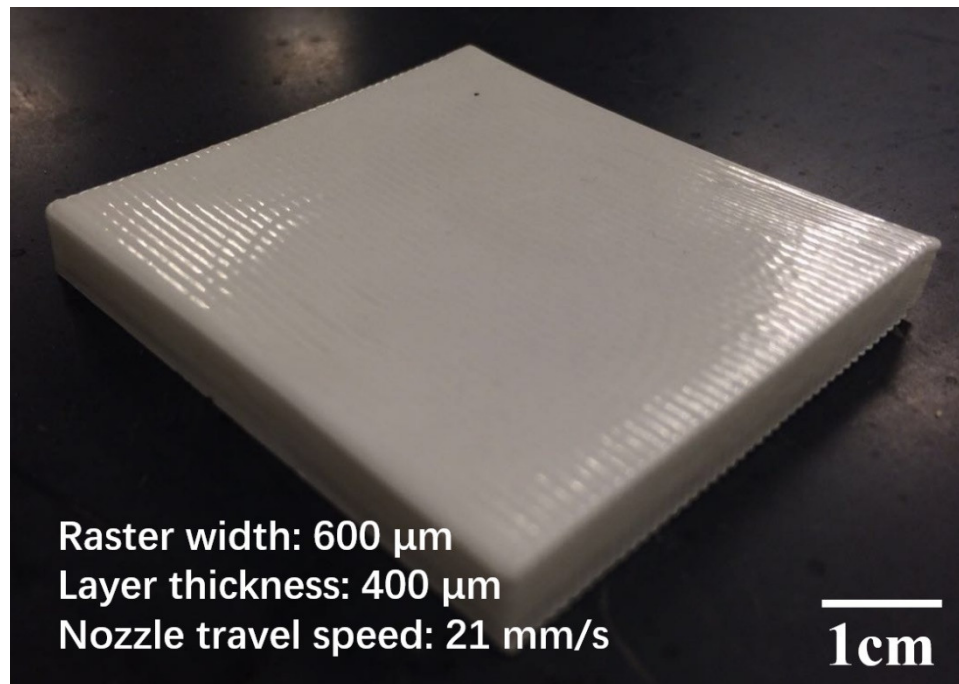
Figure 3. A sintered 3Y-TZP block fabricated by the CODE process.

3.3. MICROSTRUCTURE

An SEM micrograph showing a representative microstructure of a sintered 3Y-TZP specimen is shown in Figure 4. Neither intergranular nor intragranular porosity was observed, which was expected based on the density measurements. The average grain size was measured by the linear intercept length method [14]. Twenty horizontal lines with equal length were drawn on the SEM micrograph at random vertical positions, created a total of 494 interceptions with the grain boundaries. The average grain size was determined as 1.56 times the average linear intercept length [14], which was 0.81 μm. This is in agreement with the reported grain size under similar sintering conditions in the literature, which ranges from 0.2 to 1.0 μm [18–21]. However, lower sintering temperatures (1300~1450 °C) were found as being commonly used to obtain finer grain sizes [18–20,22–24].
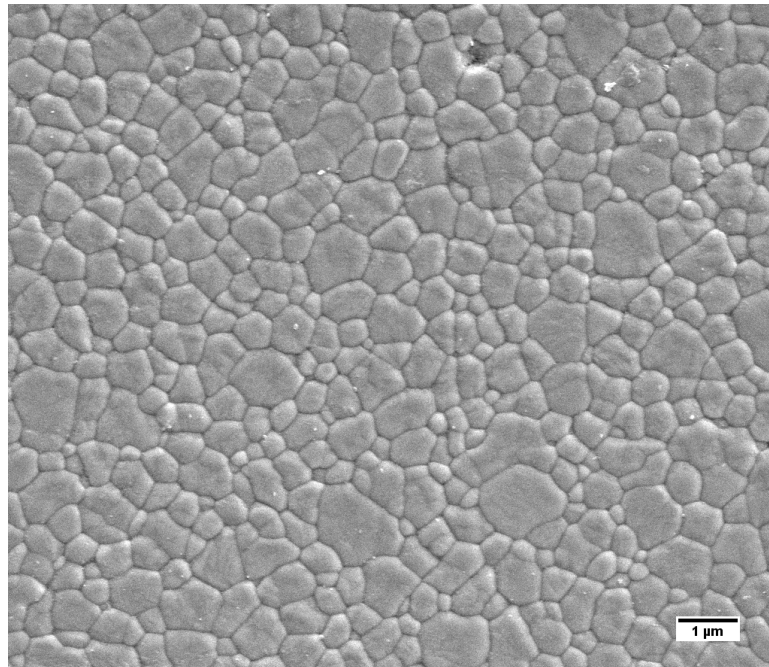
Figure 4. SEM micrograph showing the microstructure of specimens after sintering at 1550 °C for 1 h.

3.4. FRACTURE TOUGHNESS

Chevron-Notched (CN) beams were prepared from 16 B-size beams, out of which

8 CN beams were successfully cut, but the other eight beams were discarded due to

machining damage. For the 8 CN beams, the first two tests failed to give stable load

curves, so a simple compression-compression fatiguing procedure was applied to the

other six specimens according to ASTM C1421[10]. After the compression-compression

fatigue cycle[10], all six specimens exhibited stable crack growth. The average fracture

toughness (K_{Ivb}) was 4.6 MPa·m$^{0.5}$, with a standard deviation of 0.23 MPa·m$^{0.5}$. The

measured fracture toughness value is in agreement with the reported values for 3Y-TZP

under similar sintering conditions from the literature ranging from 3.8 to 5.0 MPa·m$^{0.5}$

[6,7,22,24].

3.5. FLEXURAL STRENGTH, WEIBULL MODULUS AND YOUNG'S MODULUS

Four-point bending tests were performed on 30 A-size beam specimens, of which

29 tests were valid. This was followed by a Weibull analysis. The Weibull distribution

parameters of the flexural strength values of the 29 specimens were calculated according

to ASTM C1239 [25]. The Weibull plot is shown in Figure 5. A regression analysis was

performed using Matlab to determine the Weibull modulus, $\widehat{m}$ (the slope of the fitted

line). From the regression analysis, $\widehat{m} = 8.3$ was obtained. However, the measured

Weibull modulus ($\widehat{m}$) generally exhibits statistical bias. The amount of statistical bias

depends on the number of test specimens. An unbiased estimate of m can be obtained by

multiplying $\widehat{m}$ by an unbiasing factor provided in ASTM C1239. For 29 specimens, an

unbiasing factor of 0.951 was used, resulting in the unbiased estimate of the Weibull

modulus of $m = 7.9$.
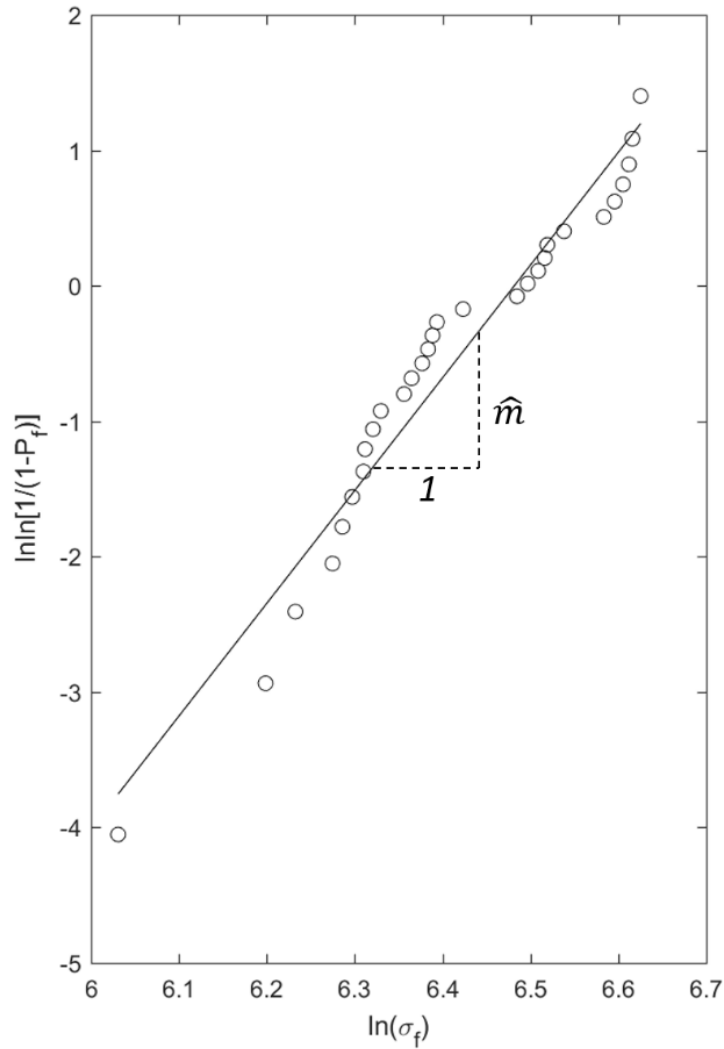
Figure 5. Weibull plot for 29 A-size beam specimens.

Among the 30 B-size beam specimens, 16 were used for preparing Chevron-

Notched beams for fracture toughness testing, four were damaged during machining. For

the remaining 10, their flexural strengths were also measured through four-point bending

tests, revealing a mean flexural strength of 563 MPa. A flexural strength comparison

between CODE specimens and specimens reported from other processes will be made in the following section. The measured Young's modulus was 221 GPa, with a standard deviation of 12.3 GPa. By correcting the assumed E values (210 GPa) used in Equation (1) to 221 GPa, the estimated fracture toughness from indentation in Table 1, Group 8 (4.3 MPa·m$^{0.5}$) was corrected to 4.4 MPa·m$^{0.5}$, which has better agreement with the fracture toughness value (4.6 MPa·m$^{0.5}$) measured from the Chevron-Notched beams.

3.6. PROPERTIES COMPARED TO OTHER PROCESSES

3.6.1. Zirconia (3YSZ) Specimens Fabricated by Other AM Processes.

Several additive manufacturing processes have been developed for ceramics, including Binder Jetting (3DP) [26–29], Stereolithography (SLA) [30–33], Lithography-based Ceramic Manufacturing (LCM) [7,34], Robocasting [35], Fused Deposition of Ceramics (FDC) [36], Freeze-form Extrusion Fabrication (FEF) [37], Selective Laser Sintering (SLS) [38,39], Selective Laser Melting (SLM) [40], Thermoplastic 3D Printing (T3DP) [41], Direct Inkjet Printing (DIP) [42], Direct Ink Writing [43–45], Extrusion-based Photo-initiate Polymerization [46], and 3D gel-printing (3DGP) [47]. Among them, a number of attempts to fabricate zirconia components have been made in the past 20 years, as briefed below.

Bertrand et al. [39] and Shahzad et al. [38] employed SLS to fabricate zirconia parts. Bertrand et al. [37] directly sintered pure Y_2O_3-ZrO_2 powder to obtain the final part. The density of their as-fabricated part was 56% T.D. (theoretical density), and they also reported that further sintering in a conventional furnace was not able to increase the density. Shahzad et al. [36] prepared a mixture containing Y_2O_3-ZrO_2 powder and

isotactic polypropylene (PP). They used SLS to melt the organic binder (PP) phase to produce green parts and then bulk-sintered the green part to obtain the final part. The density of their sintered 3Y-TZP parts was only 32% of T.D.; however, they reported that the combination of pressure infiltration (PI) of ZrO_2 suspension and warm isostatic pressing (WIP) could increase the final density to 85% of T.D.

Scheithauer et al. [41] developed the Thermoplastic 3D Printing process which combines FDM and robocasting. They used a thermoplastic binder system and Y_2O_3-ZrO_2 powder to prepare highly loaded feedstocks that were processed in a heated dispensing unit. The density of their sintered 3Y-TZP parts was reported to be 98% of T.D., but only single-wall specimens were produced.

Faes et al. [46] prepared a dispersion based on ceramic powders and UV-resin. The dispersion was selectively deposited through a nozzle while being cured by an LED array. This process was referred to as extrusion-based additive manufacturing using photo-initiated polymerization. The density reported for their sintered 3Y-TZP parts was 92% of T.D.

Özkol et al. [42] applied the direct inkjet printing (DIP) process to fabricate 3Y-TZP parts. They prepared an aqueous ink containing 40 vol% of Y_2O_3–ZrO_2 particles and used a modified HP office-type thermal inkjet printer to print the ink. The printed parts were then dried and sintered. An absolute density of 5.82 g/cm^3 was reported, which corresponds to 96.1% of T.D. They also reported the Weibull characteristic flexural strength, mean flexural strength and Weibull modulus, which were 843 MPa, 759 MPa and 3.6, respectively.

Shao et al. [47] fabricated 3Y-TZP parts with the 3D Gel-Printing (3DGP) process, which is based on a 2-hydroxyethyl methacrylate (HEMA) gelation system. The solids loading of the ZrO_2 gel was 50 vol%. The reported density, average flexural strength, and Vickers hardness were 97.6%, 450 MPa and 14.4 GPa, respectively.

Harrer et al. [7] fabricated 3Y-TZP samples with the Lithography-based Ceramic Manufacturing (LCM) technology using a commercial printer (CeraFab 7500 printer, Lithoz GmbH, Vienna, Austria) and resin with 42 vol% of ZrO_2 particles. The sintered samples achieved 6.032 g/cm^3 absolute density, corresponding to 99.6% of T.D. The reported Vickers hardness, fracture toughness, Weibull characteristic flexural strength, and Weibull modulus were 13.4 GPa, 4.9 $MPa \cdot m^{0.5}$, 878 MPa, and 11.1, respectively.

3.6.2. Comparison of Properties. In order to evaluate the relative quality of CODE fabricated 3Y-TZP specimens, a comparison of properties to conventional ceramic fabrication processes and ceramic additive manufacturing processes was made. Among various conventional processes, some sinter the green specimen under high pressure, such as hot pressing and hot isostatic pressing. The pressurized sintering processes typically exhibit higher strengths than their pressureless counterparts [24]. In order to have a fair comparison, only processes which sinter at atmospheric pressure were considered. In addition, the raw material may also affect the properties of the final specimen. By considering those effects, the property data provided by the powder manufacturer (Tosoh USA Inc., Grove City, OH, USA) was used for comparison. According to the datasheet [6], their specimens were first shaped by cold pressing under 70 MPa uniaxial pressure for 30 seconds, then sintered at atmospheric pressure. From the properties provided by the powder manufacturer, the three-point bending flexural

strength for the TZ-3Y-E powder is $\bar{\sigma}_{Tosoh-3Y} = 1000MPa$, and $\bar{\sigma}_{Tosoh-3YS} = 1500MPa$ for the TZ-3YS-E powder [6].

A direct comparison can be made for properties including density (*D*), hardness (*H*), fracture toughness (K_{IC}), and Weibull modulus (*m*). However, the observed flexural strength values of advanced ceramics are dependent on the test specimen size, geometry and stress state. Prior to making flexural strength comparisons, conversions are needed to account for the different specimen sizes and test configurations. ASTM C1683 [48] standard provides a methodology to convert the mean flexural strengths determined from different test configurations. According to [7,42], the flaw distribution was assumed to be volume-based, and Equation (2) [48] was used to convert the four-point bending flexural strengths under other configurations to the four-point bending flexural strengths under ASTM B-size configuration. Equation (3) [48] was then used to convert from the ASTM B-size four-point bending strength to the corresponding three-point bending strength under the powder supplier's (Tosoh's) configuration ($\bar{\sigma}_{DIP\text{-}B3}$). These equations are:

$$(\sigma_0)_v = \frac{\bar{\sigma}_{B4}\left\{\left[\left(\frac{L_{i4}}{L_{o4}}\right)\cdot m+1\right]\cdot\left[\frac{1}{2(m+1)^2}\right]\cdot b\cdot d\cdot L_{o4}\right\}^{1/m}}{\Gamma\left(\frac{1}{m}+1\right)} \tag{2}$$

$$\frac{\bar{\sigma}_{B3}}{\bar{\sigma}_{B4}} = \left(\frac{L_{o4}}{L_{o3}}\right)^{1/m}\left(\frac{m+2}{2}\right)^{1/m} \tag{3}$$

The flexural strength of CODE specimens under ASTM B-size four-point bending configuration ($\bar{\sigma}_{CODE\text{-}B4}$) was converted to obtain three-point bending flexural strength values ($\bar{\sigma}_{CODE\text{-}B3}$) which would correspond to the powder supplier's (Tosoh's) configuration using Equation (3), irrespective of whether the flaws are surface or volume-distributed. The nomenclature for Equations (2) and (3) is given below:

$\bar{\sigma}_{B4}$ = mean strength of a four-point flexure test specimen;

$\bar{\sigma}_{B3}$ = mean strength of a three-point flexure test specimen;

m = Weibull modulus;

b = width of a flexure test specimen;

d = thickness of a flexure test specimen;

L_{i4} = length of the inner span of a four-point flexure test specimen;

L_{o4} = length of the outer span of a four-point flexure test specimen;

L_{o3} = length of the outer span of a three-point flexure test specimen;

Table 3. Mechanical properties of ZrO_2 (3YSZ) specimens from different ceramic fabrication processes.

		Raw powder	D (%)	HV (GPa)	K_{IC} (MPa·m[0.5])	σ (MPa)	m	Comments
Conventional	**Cold uniaxial**	TZ-3Y-E[1]	99.9	12.3	5	1000	N.D.	Provided
Process	**Pressing [6]**	TZ-3YS-E[1]	99.9	12.3	5	1500	N.D.	by Tosoh [6]
AM Processes	**SLS [38,39]**	ZYP30[2]	56.0	N.D.	N.D.	N.D.	N.D.	--
	T3DP [41]	TZ-3YS-E	98.0	N.D.	N.D.	N.D.	N.D.	--
	EPP [46]	TZ-3Y-E	92.0	N.D.	N.D.	N.D.	N.D.	--
	DIP [42]	TZ-3YS-E	96.1	N.D.	N.D.	723	3.6	48.2% of $\bar{\sigma}_{Tosoh-3YS}$
	3DGP [47]	N.D.	97.6	14.4	N.D.	450	N.D.	--
	LCM [7]	N.D.	99.6	13.4	4.9	885	11.1	--
	CODE	TZ-3Y-E	99.2	13.1	4.6	715	7.9	71.5% of $\bar{\sigma}_{Tosoh-3Y}$

Note: 1. Powder supplied by Tosoh USA, Inc., Grove City, OH, USA. 2. Powder supplied by Zircar Zirconia, Inc., Florida, NY, USA

Similar conversions were applied to the reported results of DIP, LCM and 3DGP processes, and the converted values were eligible for direct comparison. It should be noted that the strength of CODE specimens was compared to $\bar{\sigma}_{Tosoh-3Y}$ since TZ-3Y-E powder was used in the CODE process, while the DIP's specimens' strength was

compared to $\bar{\sigma}_{Tosoh-3YS}$, which corresponds to the TZ-3YS-E powder used. Table 3

summarizes the comparison of the mechanical properties between the CODE process, a

representative conventional ceramic fabrication process, and other AM processes. The

density (D), Vickers hardness (HV), fracture toughness (K_{IC}), three-point bending flexural

strength (σ) and Weibull modulus (m) values in Table 3 are the highest values found in

the literature, the non-disclosed properties are marked as "N.D.".

      3.6.3. Discussion on Specimens' Properties. As presented in Table 3, among all

AM processes to date, only the CODE and LCM processes produce specimens

with >99% relative density, i.e., 99.2% and 99.6%, respectively. Compared to the

conventional process, however, the cold uniaxial pressed specimens reported by Tosoh

achieved a 99.9% relative density. One reason for the slightly lower specimen density of

the CODE and LCM processes was the defects inherent in the AM processes, such as

porosity caused by the inhomogeneity of feedstock and inaccuracy of material dispensing

[4,7,13,34,49]. Another reason could be their likely lower green density compared to

Tosoh's conventional processing, where the 70 MPa uniaxial pressing provided better

particle packing. Further investigations will be required to confirm this hypothesis. The

hardness and fracture toughness of CODE fabricated specimens are close to those of cold

uniaxial pressed specimens. The flexural strength and Weibull modulus are both lower

than the values associated with the LCM process, i.e., 715 MPa vs. 885 MPa and 11.1 vs.

7.9. However, since the powder used in the LCM process is not disclosed, further

information is needed for a complete comparison. Compared to the conventional process,

the flexural strength of CODE's specimens reaches ~71% of the values for cold uniaxial

pressed specimens reported by Tosoh ($\bar{\sigma}_{Tosoh-3Y}$). The absolute flexural strength reported

from the DIP process is slightly higher than that of CODE (715 MPa vs. 723 MPa),

however, the relative strength obtained by the DIP process is ~48% compared to the

values provided by Tosoh ($\bar{\sigma}_{Tosoh-3YS}$). This low bending strength could be caused by

pores considering the relatively low density (96.1%) of DIP fabricated specimens.

Overall, the 3YSZ components produced by the CODE process achieved the highest

relative density and relative flexural strength among all extrusion-based AM processes.

The Griffith criterion was used to estimate the expected critical flaw sizes in the

specimens. Equation (4) was used for calculating the flaw size, where $2a$ is the size of the

critical flaw (m), K_{IC} is the fracture toughness (MPa·m$^{0.5}$), σ_f is the fracture stress

(MPa), and Y is the stress intensity shape factor.

$$2a = 2 \cdot \left(\frac{K_{IC}}{Y \cdot \sigma_f} \right)^2 \tag{4}$$

According to ASTM 1322 [50], for volume flaws Y is equal to 1.77 or 1.13 for

penny-shaped narrow flaws and circular flaws, respectively; while for surface flaws, Y is

1.99 or 1.29 depending on the flaw geometry. Thus, the estimated flaw size ranged from

27 μm to 65 μm when the flaw was assumed to have a volume origin, and ranged from

21 μm to 50 μm when the flaw was assumed to have a surface origin. Considering the

fact that the grain size of the specimens was submicron, the less than 100% relative

flexural strength of CODE specimens was more likely to be caused by the higher

porosity, i.e., lower density (99.2% vs. 99.9%) compared to the uniaxially pressed

specimens, instead of the grain size and/or grain boundaries. The higher porosity, as

mentioned earlier, could have been resulted from the manufacturing defects inherent in

the AM processes.

3.7. SAMPLE COMPONENTS

To demonstrate the capabilities of the CODE process to fabricate 3D components with complex geometries and validate the printability of the ZrO_2 paste, several samples were successfully fabricated and sintered. Figure 6(a) shows two double helical gears fabricated using a 600 μm (inner diameter) nozzle. The layer thickness for printing was 400 μm which decreased to approximately 320 μm after sintering. A heart-shaped pendant fabricated using a 300 μm nozzle is shown in Figure 6(b), with a close-up side view, where the layer thickness was about 120 μm after sintering. Figure 6(c) shows a structure with four thin walls (0.5 mm) fabricated using a 200 μm nozzle, where the layer thickness was about 80 μm after sintering. All three types of sample components were fabricated without visible pores and gaps, indicating a high consistency of extrusion flow rate and effective extrusion starts and stops [4].
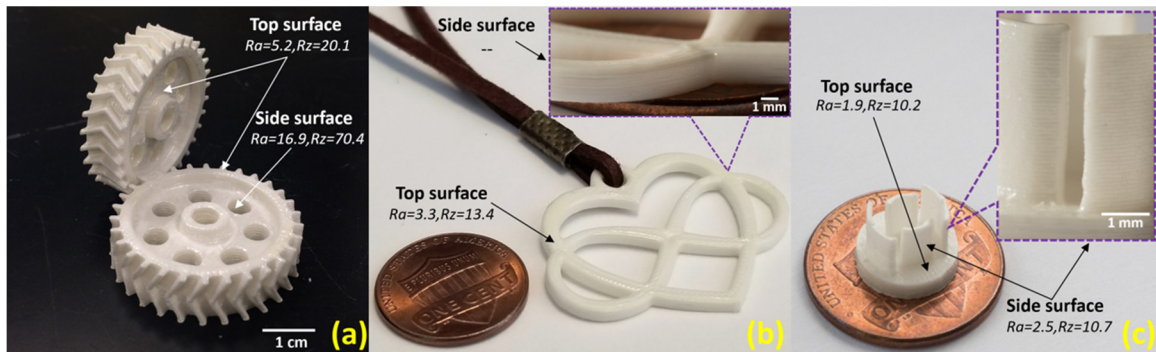
Figure 6. Sintered 3YSZ sample components: (a) two double helical gears, (b) a heart-shaped pendant, (c) thin wall structures.

The surface finish of the sample components was examined by a surface roughness tester (Mahr PS1, Mahr Gmbh, Göttingen, Germany). The tested surfaces were marked in Figure 6, and three measurements were taken for each surface at random

spots. When examining the roughness of the side surface, the probe traveled in the direction perpendicular to the layer plane. The probe traveled perpendicular to the direction of the deposited raster when examining the top surface. The side surface in Figure 6 (b) wasn't examined since the height (~2.4 mm) of the pendant was lower than the required length of the probe scanning path. The surface roughness measurements and their averaged values are presented in Table 4. The *Ra* and *Rz* of the gears' side surface were significantly higher than those of their top surface, i.e., 16.9 µm vs. 5.2 µm and 70.4 µm vs. 20.1 µm. This phenomenon is common in extrusion-based AM processes since a periodically fluctuated side surface is formed when stacking the layers vertically [51]. Thus a positive correlation exists between layer thickness and side surface roughness. The thin wall component in Figure 6(c) were fabricated with a much finer nozzle (200 µm vs. 600 µm in diameter) and layer thickness (80 µm vs. 320 µm) compared to the gears, thus a much lower surface roughness was obtained, as presented in Table 4, and the difference between its top surface and side surface became insignificant.

Table 4. Surface roughness values measured from example components.

Measurements (µm)	#1		#2		#3		Average	
	Ra	Rz	Ra	Rz	Ra	Rz	Ra	Rz
Top surface in Fig. 6 (a)	6.1	23.1	4.9	18.4	4.6	18.8	5.2	20.1
Side surface in Fig. 6 (a)	16.0	64.2	17.5	72.9	17.1	73.0	16.9	70.4
Top surface in Fig. 6 (b)	3.5	14.3	3.5	13.8	3.0	12.0	3.3	13.4
Top surface in Fig. 6 (c)	1.6	8.7	1.7	9.5	2.5	12.4	1.9	10.2
Side surface in Fig. 6 (c)	2.1	8.8	3.0	12.7	2.5	10.6	2.5	10.7

4. CONCLUSIONS

An aqueous paste consisting of 3 mol% yttria-stabilized zirconia was developed, and the Ceramic On-Demand Extrusion (CODE) process was employed to fabricate 3Y-TZP test specimens and sample components. The properties of fabricated test specimens were examined. A relative density of 99.1%-99.5% was achieved. The Vickers hardness (HV) and fracture toughness (K_{Ivb}) measured were 13.1 GPa and 4.6 MPa·m$^{0.5}$, respectively. The flexural strength obtained from a four-point bending test was 563 MPa, from which the estimated three-point bending strength was 715 MPa.

The measured results were compared to those from other additive manufacturing processes and a representative conventional process. The comparisons revealed that the density and bending strength of the CODE fabricated specimens are similar to those from the vat photopolymerization-based process (LCM) and stand out as the highest among all extrusion-based AM processes. The flexural strength reached ~70% of those of cold uniaxial pressed specimens, and the hardness and fracture toughness were close to that of cold uniaxial pressed specimens. Several sample components were successfully fabricated with 320, 120 and 80 μm layer thickness, which demonstrated CODE's capability of fabricating non-sparse components having a complex geometry and fine features. The surface roughness measurements having Ra and Rz of 5.2 μm and 20.1 μm, respectively, were obtained for the top surface of the specimens with approximately 320 μm layer thickness, while their side surface had Ra and Rz of 16.9 μm and 70.4 μm, respectively. For the specimen with approximately 80 μm layer thickness, the Ra and Rz

for both top surface and side surface were close and ranged from 1.6 µm to 3.0 µm and

8.7 µm to 12.7 µm, respectively.

ACKNOWLEDGMENTS

REFERENCES

[1]   R.H.J. Hannink, P.M. Kelly, B.C. Muddle, Transformation Toughening in Zirconia-Containing Ceramics, J. Am. Ceram. Soc. 83 (2004) 461–487. doi:10.1111/j.1151-2916.2000.tb01221.x.

[2]   A. Ghazanfari, W. Li, M.C. Leu, G.E. Hilmas, A novel freeform extrusion fabrication process for producing solid ceramic components with uniform layered radiation drying, Addit. Manuf. 15 (2017) 102–112. doi:10.1016/j.addma.2017.04.001.

[3]   W. Li, A. Ghazanfari, D. McMillen, A. Scherff, M.C. Leu, G.E. Hilmas, Fabricating Zirconia Parts with Organic Support Material by the Ceramic On-Demand Extrusion Process, in: D. Bourell, J. Beaman, R. Crawford (Eds.), Proc. 28th Annu. Int. Solid Free. Fabr. Symp., Austin,TX, 2017: pp. 606–615.

[4]   W. Li, A. Ghazanfari, M.C. Leu, R.G. Landers, Extrusion-on-demand methods for high solids loading ceramic paste in freeform extrusion fabrication, Virtual Phys. Prototyp. 12 (2017) 193–205. doi:10.1080/17452759.2017.1312735.

[5]   ASTM C373, Standard Test Method for Water Absorption, Bulk Density, Apparent Porosity, and Apparent Specific Gravity of Fired Whiteware Products, Ceramic Tiles, and Glass Tiles, (2014). doi:http://dx.doi.org/10.1520/C0373-14A.

[6]   Tosoh, Tosoh zirconia powder specification and typical properties, TOKYO, JAPAN, 2003. https://www.tosohusa.com/products--services/ceramic-materials.

[7]   W. Harrer, M. Schwentenwein, T. Lube, R. Danzer, Fractography of zirconia-specimens made using additive manufacturing (LCM) technology, J. Eur. Ceram. Soc. 37 (2017) 4331–4338. doi:10.1016/j.jeurceramsoc.2017.03.018.

[8]   ASTM C1327, Standard test method for Vickers indentation hardness of advanced ceramics, West Conshohocken, PA, 2015. doi:10.1520/C1327.

[9]   G.R. Anstis, P. Chantikul, B.R. Lawn, D.B. Marshall, A critical evaluation of indentation techniques for measuring fracture toughness: I, direct crack measurements, J. Am. Ceram. Soc. 64 (1981) 533–538. doi:10.1111/j.1151-2916.1981.tb10320.x.

[10]   ASTM C1421, Standard test methods for determination of fracture toughness of advanced ceramics, West Conshohocken, PA, 2007. doi:10.1520/C1421.

[11]   ASTM C1161, Standard test method for flexural strength of advanced ceramics at ambient temperatures, West Conshohocken, PA, 2008. doi:10.1520/C1161.

[12]   M.H. Sadd, Elasticity: Theory, Applications, and Numerics, second edi, Academic Press, Burlington, MA, USA, 2009.

[13]   A. Ghazanfari, W. Li, M.C. Leu, J.L. Watts, G.E. Hilmas, Additive manufacturing and mechanical characterization of high density fully stabilized zirconia, Ceram. Int. 43 (2017) 6082–6088. doi:10.1016/j.ceramint.2017.01.154.

[14]   M.I. Mendelson, Average Grain Size in Polycrystalline Ceramics, J. Am. Ceram. Soc. 52 (1969) 443–446. doi:10.1111/j.1151-2916.1969.tb11975.x.

[15]   C.A. Schneider, W.S. Rasband, K.W. Eliceiri, NIH Image to ImageJ: 25 years of image analysis, Nat. Methods 2012 97. (2012). doi:doi:10.1038/nmeth.2089.

[16]   T. Kosmač, C. Oblak, P. Jevnikar, N. Funduk, L. Marion, The effect of surface grinding and sandblasting on flexural strength and reliability of Y-TZP zirconia ceramic, Dent. Mater. 15 (1999) 426–433. doi:10.1016/S0109-5641(99)00070-6.

[17]   B.A. Cottom, M.J. Mayo, Fracture toughness of nanocrystalline ZrO_2-3mol% Y_2O_3 determined by Vickers indentation, Scr. Mater. 34 (1996) 809–814. doi:10.1016/1359-6462(95)00587-0.

[18]   N. Wang, Z. Wang, K.T. Aust, U. Erb, Effect of grain size on mechanical properties of nanocrystalline materials, Acta Metall. Mater. 43 (1995) 519–528. doi:10.1016/0956-7151(94)00253-E.

[19]   M. Trunec, Z. Chlup, Higher fracture toughness of tetragonal zirconia ceramics through nanocrystalline structure, Scr. Mater. 61 (2009) 56–59. doi:10.1016/j.scriptamat.2009.03.019.

[20]   Y.H. Sun, Y. feng Zhang, J.K. Guo, Microstructure and bending strength of 3Y-TZP ceramics by liquid-phase sintering with CAS addition, Ceram. Int. 29 (2003) 229–232. doi:10.1016/S0272-8842(02)00097-4.

[21]   M. Guazzato, M. Albakry, S.P. Ringer, M. V. Swain, Strength, fracture toughness and microstructure of a selection of all-ceramic materials. Part II. Zirconia-based dental ceramics, Dent. Mater. 20 (2004) 449–456. doi:10.1016/j.dental.2003.05.002.

[22]   F. Zhang, K. Vanmeensel, M. Inokoshi, M. Batuk, J. Hadermann, B. Van Meerbeek, I. Naert, J. Vleugels, 3Y-TZP ceramics with improved hydrothermal degradation resistance and fracture toughness, J. Eur. Ceram. Soc. 34 (2014) 2453–2463. doi:10.1016/j.jeurceramsoc.2014.02.026.

[23]   M. Ghatee, M.H. Shariat, J.T.S. Irvine, Investigation of electrical and mechanical properties of 3YSZ/8YSZ composite electrolytes, Solid State Ionics. 180 (2009) 57–62. doi:10.1016/J.SSI.2008.10.006.

[24]   M. Guazzato, M. Albakry, S.P. Ringer, M. V Swain, Strength, fracture toughness and microstructure of a selection of all-ceramic materials. Part II. Zirconia-based dental ceramics, Dent. Mater. 20 (2004) 449–456. doi:10.1016/J.DENTAL.2003.05.002.

[25]   ASTM C1239, Standard practice for reporting uniaxial strength data and estimating Weibull distribution parameters for advanced ceramics, West Conshohocken, PA, 2013. doi:10.1520/C1239.

[26]   H. Miyanaji, S. Zhang, A. Lassell, A. Zandinejad, L. Yang, Process development of porcelain ceramic material with binder jetting process for dental applications, J. Miner. Met. Mater. Soc. 68 (2016) 831–841. doi:10.1007/s11837-015-1771-3.

[27]   S. Zhang, H. Miyanaji, L. Yang, A. Ali Zandinejad, J. Dilip, B. Stucker, An experimental study of ceramic dental porcelain materials using a 3D print (3DP) process, in: D. Bourell, J. Beaman, R. Crawford (Eds.), Proc. 25th Annu. Int. Solid Free. Fabr. Symp., Austin,TX, 2014: pp. 991–1011.

[28]   S.M. Gaytan, M.A. Cadena, H. Karim, D. Delfin, Y. Lin, D. Espalin, E. MacDonald, R.B. Wicker, Fabrication of barium titanate by binder jetting additive manufacturing technology, Ceram. Int. 41 (2015) 6610–6619. doi:10.1016/J.CERAMINT.2015.01.108.

[29] J.A. Gonzalez, J. Mireles, Y. Lin, R.B. Wicker, Characterization of ceramic components fabricated using binder jetting additive manufacturing technology, Ceram. Int. 42 (2016) 10559–10564. doi:10.1016/J.CERAMINT.2016.03.079.

[30] T. Chartier, C. Chaput, F. Doreau, M. Loiseau, Stereolithography of structural complex ceramic parts, J. Mater. Sci. 37 (2002) 3141–3147. doi:10.1023/A:1016102210277.

[31] Q. Lian, F. Yang, H. Xin, D. Li, Oxygen-controlled bottom-up mask-projection stereolithography for ceramic 3D printing, Ceram. Int. 43 (2017) 14956–14961. doi:10.1016/J.CERAMINT.2017.08.014.

[32] H. Xing, B. Zou, S. Li, X. Fu, Study on surface quality, precision and mechanical properties of 3D printed ZrO_2 ceramic components by laser scanning stereolithography, Ceram. Int. 43 (2017) 16340–16347. doi:10.1016/J.CERAMINT.2017.09.007.

[33] H. Wu, W. Liu, R. He, Z. Wu, Q. Jiang, X. Song, Y. Chen, L. Cheng, S. Wu, Fabrication of dense zirconia-toughened alumina ceramics through a stereolithography-based additive manufacturing, Ceram. Int. 43 (2017) 968–972. doi:10.1016/J.CERAMINT.2016.10.027.

[34] M. Schwentenwein, J. Homa, Additive manufacturing of dense alumina ceramics, Int. J. Appl. Ceram. Technol. 12 (2015) 1–7. doi:10.1111/ijac.12319.

[35] N. Travitzky, A. Bonet, B. Dermeik, T. Fey, I. Filbert-Demut, L. Schlier, T. Schlordt, P. Greil, Additive manufacturing of ceramic-based materials, Adv. Eng. Mater. 16 (2014) 729–754. doi:10.1002/adem.201400097.

[36] M.K. Agarwala, R. Van Weeren, A. Bandyopadhyayl, P.J. Whalen, A. Safari, S.C. Danforth, Fused deposition of ceramics and metals : an overview, (n.d.).

[37] T. Huang, M.S. Mason, G.E. Hilmas, M.C. Leu, Freeze-form extrusion fabrication of ceramic parts, Virtual Phys. Prototyp. 1 (2006) 93–100. doi:10.1080/17452750600649609.

[38] K. Shahzad, J. Deckers, Z. Zhang, J.-P. Kruth, J. Vleugels, Additive manufacturing of zirconia parts by indirect selective laser sintering, J. Eur. Ceram. Soc. 34 (2014) 81–89. doi:10.1016/J.JEURCERAMSOC.2013.07.023.

[39] P. Bertrand, F. Bayle, C. Combe, P. Goeuriot, I. Smurov, Ceramic components manufacturing by selective laser sintering, Appl. Surf. Sci. 254 (2007) 989–992. doi:10.1016/J.APSUSC.2007.08.085.

[40]   J. Wilkes, Y. Hagedorn, W. Meiners, K. Wissenbach, Additive manufacturing of ZrO$_2$ -Al$_2$O$_3$ ceramic components by selective laser melting, Rapid Prototyp. J. 19 (2013) 51–57. doi:10.1108/13552541311292736.

[41]   U. Scheithauer, E. Schwarzer, H.-J. Richter, T. Moritz, Thermoplastic 3D printing-an additive manufacturing method for producing dense ceramics, Int. J. Appl. Ceram. Technol. 12 (2015) 26–31. doi:10.1111/ijac.12306.

[42]   E. Özkol, W. Zhang, J. Ebert, R. Telle, Potentials of the "Direct inkjet printing" method for manufacturing 3Y-TZP based dental restorations, J. Eur. Ceram. Soc. 32 (2012) 2193–2201. doi:10.1016/J.JEURCERAMSOC.2012.03.006.

[43]   C.F. Revelo, H.A. Colorado, 3D printing of kaolinite clay ceramics using the Direct Ink Writing (DIW) technique, Ceram. Int. (2017). doi:10.1016/J.CERAMINT.2017.12.219.

[44]   L. Rueschhoff, W. Costakis, M. Michie, J. Youngblood, R. Trice, Additive Manufacturing of Dense Ceramic Parts via Direct Ink Writing of Aqueous Alumina Suspensions, Int. J. Appl. Ceram. Technol. 13 (2016) 821–830. doi:10.1111/ijac.12557.

[45]   J.A. Lewis, J.E. Smay, J. Stuecker, J. Cesarano, Direct Ink Writing of Three-Dimensional Ceramic Structures, J. Am. Ceram. Soc. 89 (2006) 3599–3609. doi:10.1111/j.1551-2916.2006.01382.x.

[46]   M. Faes, J. Vleugels, F. Vogeler, E. Ferraris, Extrusion-based additive manufacturing of ZrO$_2$ using photoinitiated polymerization, CIRP J. Manuf. Sci. Technol. 14 (2016) 28–34. cccccdoi:10.1016/J.CIRPJ.2016.05.002.

[47]   H. Shao, D. Zhao, T. Lin, J. He, J. Wu, 3D gel-printing of zirconia ceramic parts, Ceram. Int. 43 (2017) 13938–13942. doi:10.1016/J.CERAMINT.2017.07.124.

[48]   ASTM C1683, Standard Practice for Size Scaling of Tensile Strengths Using Weibull Statistics for Advanced Ceramics, West Conshohocken, PA, 2010. doi:10.1520/C1683.

[49]   J. Li, An experimental study of fabrication temperature effect on aqueous extrusion freeform fabrication, Missouri University of Science and Technology, 2014.

[50]   ASTM 1322, Standard Practice for Fractography and Characterization of Fracture Origins in Advanced Ceramics, West Conshohocken, PA, 2010. doi:10.1520/C1322-05BR10.2.

[51]   H. Zhao, Y. He, J. Fu, J. Qiu, Inclined layer printing for fused deposition modeling without assisted supporting structure, Robot. Comput. Integr. Manuf. 51 (2018) 1–13. doi:10.1016/J.RCIM.2017.11.011.

III. FABRICATING CERAMIC COMPONENTS WITH WATER DISSOLVABLE SUPPORT STRUCTURES BY THE CERAMIC ON-DEMAND EXTRUSION PROCESS

ABSTRACT

This paper describes a further development of the novel Ceramic On-Demand Extrusion (CODE) process that was recently being developed. The new development focuses on fabricating ceramic components that have external/internal features such as overhangs, conformal cooling channels, etc. and thus cannot be fabricated without the use of support structures. The minimum angle of a slanted surface that can be fabricated using Al_2O_3 (alumina) paste without the need for a support structure is first determined. An inorganic sacrificial material, $CaCO_3$, is then identified for building support structures. After a green part with both main and sacrificial materials has been fabricated, it is dried and then sintered. During sintering, the main material densifies, while the sacrificial material decomposes and is then dissolved in water or acid. Sample parts are fabricated and evaluated to demonstrate the effectiveness of the sacrificial material as well as CODE's capability of fabricating geometrically complex parts.

1. INTRODUCTION

Fabricating three-dimensional components from ceramic materials is often expensive and time-consuming, and part geometrical complexity is limited when using conventional processing and machining techniques. Additive manufacturing (AM) can

be applied to reduce the fabrication time and cost, especially for small runs and for components with complex geometries.

Several AM techniques have been developed for ceramics and glasses, including binder jetting [1], material extrusion [2-6], vat photopolymerization [7], powder bed fusion [8,9], directed energy deposition [10], etc. Ceramic On-Demand Extrusion (CODE) is a recently developed paste extrusion based AM process, which produces ceramic components with near theoretical (>98%) density after sintering. It deposits high solids loading (>50 vol%) ceramic pastes onto a substrate layer by layer at room temperature. The printed parts are dried in a controlled environment with appropriate humidity to produce crack-free green parts, after which the green parts are sintered to produce highly dense ceramic parts [11,12].

The present paper describes the development of a method for fabricating ceramic parts with complex geometries or features that require the use of sacrificial support structures in the CODE process. A novel CODE fabrication machine was developed and configured to work with two extruders capable of depositing two materials. Concurrent deposition of the sacrificial material enables the CODE process to fabricate ceramic parts that have external/internal features such as overhangs, conformal channels, etc. Unlike the Freeze-form Extrusion Fabrication process [9], which is another paste extrusion based ceramic AM process that solidifies the paste by freezing, the selection of a suitable sacrificial material in the CODE process is more challenging because the process operates at room temperature. After identifying calcium carbonate ($CaCO_3$) as a workable sacrificial material, which decomposes during sintering and can be removed by dissolving in water or acid after sintering, aqueous $CaCO_3$ paste was prepared as the

support material. A multi-step sintering technique was used for Al_2O_3 parts due to the favorable phase equilibria between Al_2O_3 and $CaCO_3$ within the sintering temperature range. For demonstration purpose, cuboid parts with rectangular through-holes were fabricated to examine part dimensional accuracy. The fabrication of a geometrically complex part with overhangs and tube-shaped features by the CODE process was also successfully demonstrated.

2. PROCESS OVERVIEW AND EXPERIMENTAL SETUP

The CODE process extrudes and deposits aqueous pastes onto a substrate to print each layer sequentially. The substrate is placed inside a tank designed to hold a fluid medium (normally oil). Once one layer is deposited completely, the oil is pumped into the tank to surround the part, preventing undesirable water evaporation from the perimeters of the deposited layers. The oil level is maintained just below the topmost layer of the part being fabricated. Infrared radiation is then applied in a direction perpendicular to the top surface to uniformly dry the deposited layer, so that the part being fabricated will be partially dried and stiffened. This enables the printed body to sustain the weight of the subsequently deposited layers without deformation. By repeating the above steps, the part is printed in a layerwise fashion [11-13]. The layered uniform radiation drying, together with the prohibition of evaporation from the sides of the part, prevents moisture gradation in the part, thus avoiding part cracking and warping. Once a part is completely printed and removed from the oil tank, the remaining water content is eliminated by bulk drying to obtain a green body. The green body then goes

through post-processing, including sacrificial material removal, binder burnout, and sintering, to obtain a dense ceramic part.

The CODE fabrication system consists of a motion subsystem (gantry); extrusion devices mounted on the gantry and capable of extruding viscous ceramic pastes at controlled flow rates; an oil feeding device to regulate the oil level in the tank; and an infrared radiation heating device capable of moving the infrared source and providing on/off control. Figure 1 shows the CODE fabrication system and its environment. The details of this system and its subsystems were presented in our previous papers [11,14].
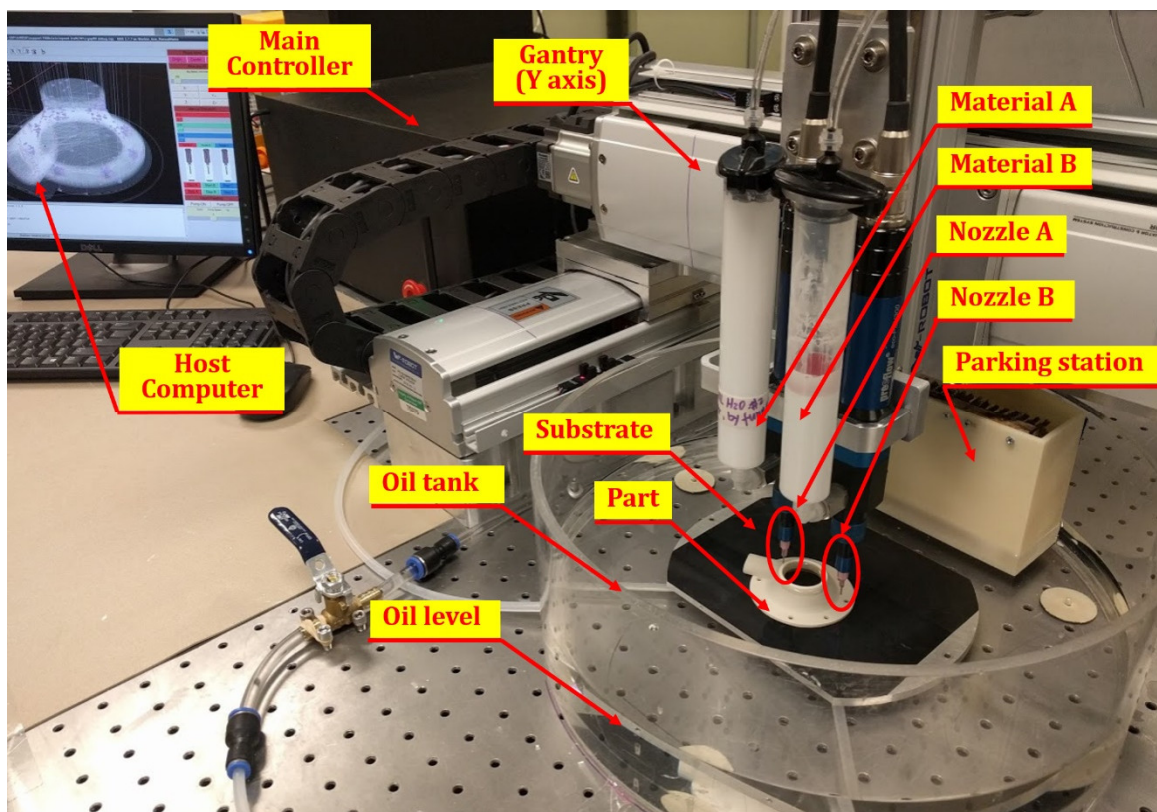
Figure 1. The CODE fabrication system configured for dual-extruder printing.

3. PART FABRICATION

3.1. PASTE PREPARATION

A 55 vol% solids loading alumina (Al_2O_3) paste was developed by following a previously developed recipe described in [13]. The calcium carbonate paste was prepared from $CaCO_3$ powder (Sigma Aldrich, St. Louis, MO, USA). Acetone (Sigma Aldrich, St. Louis, MO, USA) was the solvent chosen for ball milling to reduce the average particle size. An ammonium polyacrylate, Dolapix CE 64 (Zschimmer & Schwarz, Germany), was used as the dispersant; PEG 400 (poly (ethylene glycol); Sigma Aldrich, St. Louis, MO, USA) as the lubricant and humectant; and cold water dispersible c(methylcellulose; Dow Chemical Company, Pevely, MO, USA) as the binder. Both alumina paste and calcium carbonate paste have a viscosity around 200 Pa·s.

3.2. DETERMINATION OF MAXIMUM OVERHANG ANGLE

An experiment was conducted to find out the maximum angle of overhanging features that the CODE process is capable of printing without using support structures. In this experiment, a 55 vol% solids loading alumina paste was used. Several wedge-shaped parts with different overhang angles were identified as test parts. The process parameters in this experiment are listed in Table 1, whose values were determined and successfully implemented in previous studies [13]. As shown in Figure 2, the overhang did not start to collapse until the test parts with a 60° overhang were attempted. Hence, for the 55 vol% solids loading alumina paste, the maximum overhang angle for the CODE process was identified to be between 55° and 60°. Note that the limit of overhang angle may vary for

different part shape and process parameters. The wedge-shaped structure, compared to thin-wall and cylindrical structures, better represents the typical overhanging structure in AM processes. Hence, it was selected as a benchmark in this test.

Table 1. Process parameters for wedge-shaped test parts.

Parameter	Value
Nozzle diameter	610 μm
Layer thickness	400 μm
Distance between nozzle and build surface	0
Overall printing speed	20 mm/s
Number of perimeters	2
Drying time	10 s per layer
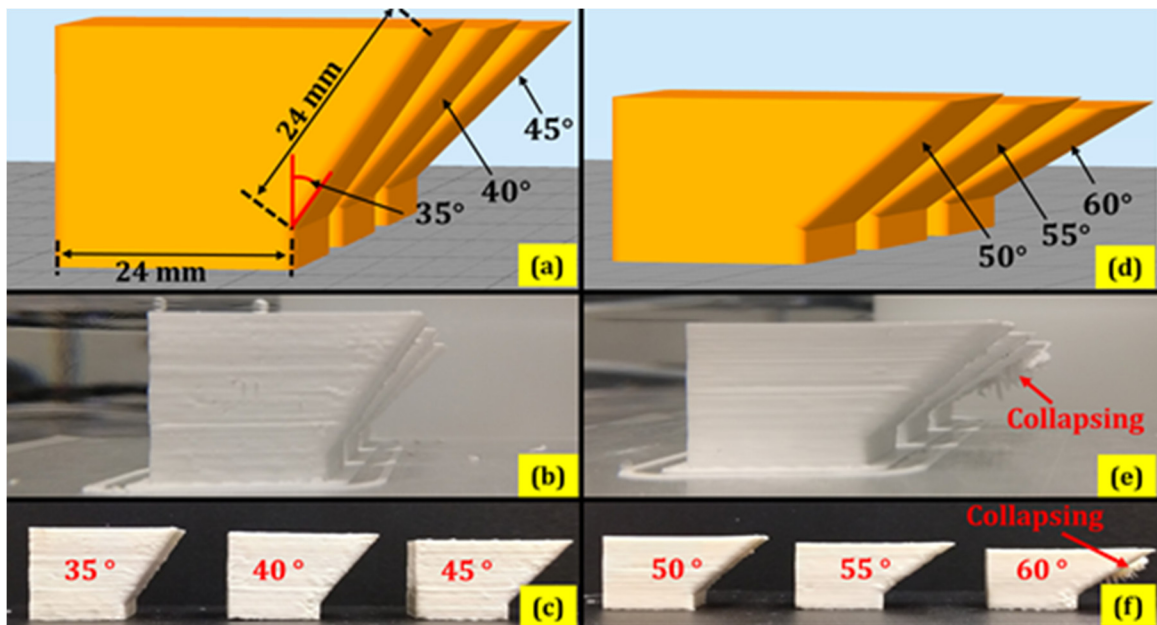
Figure 2. Wedge-shaped test parts: (a)(d) CAD model, (b)(e) As-printed parts surrounded by oil, (c)(f) As-sintered parts.

3.3. PRINTING OF SAMPLE PARTS

In this experiment, some sample parts which require support structures were fabricated to demonstrate the CODE system's capability of fabricating 3D components, evaluate the dimensional accuracy of fabricated parts, and validate the feasibility of using $CaCO_3$ paste as a support material.

3.3.1. Simple-geometry Sample Part. A cuboid with rectangular through-holes was chosen as a sample geometry to evaluate the dimensional accuracy of parts fabricated by the CODE process. The CAD model and the printing process of the cuboid are shown in Figure 3. Five cuboid sample parts were fabricate using the process parameters in Table 1. The main structure infill density was 100% (i.e., solid), and the support structure was printed with 50% density.
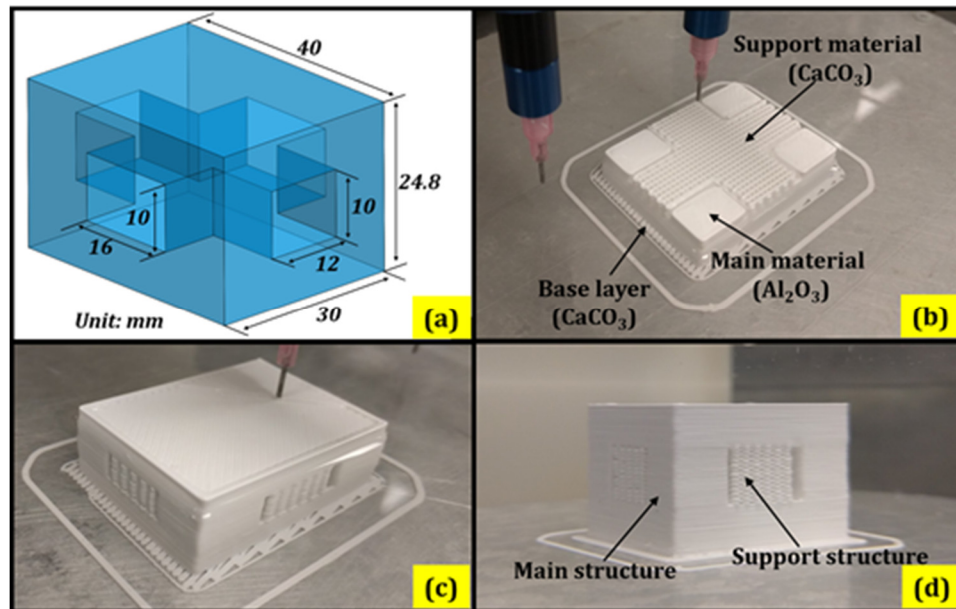
Figure 3. The cuboid part with rectangular holes: (a) CAD model, (b)(c) Part being printed, (d) Part printed completely and surrounded by oil.

3.3.2. Complex-geometry Sample Part. In addition to the sample cuboids, a turbine-blower housing with a relatively complex geometry (Figure 4) was printed to further validate the capability of the CODE process and the feasibility of the $CaCO_3$ support material. The same process parameters used for the cuboid samples were used in this experiment.
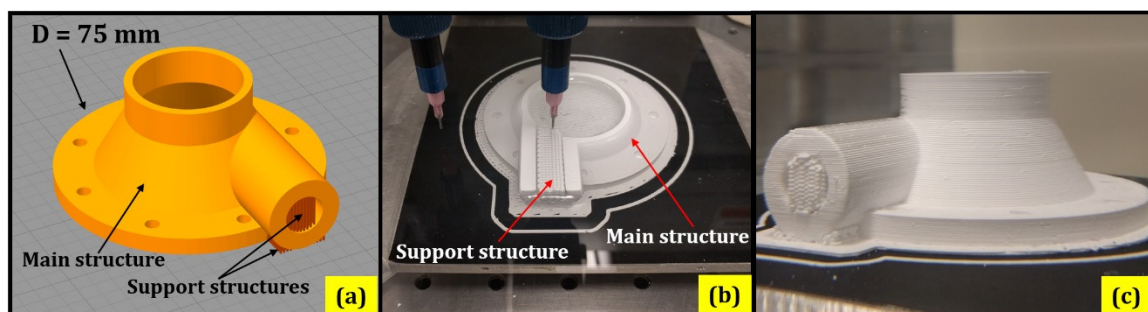
Figure 4. Sample turbine-blower housing: (a) CAD model with main and support structures, (b) Part being printed, (c) Completely printed part surrounded by oil.

3.4. POST-PROCESSING AND SUPPORT STRUCTURE REMOVAL

After the parts were printed, the oil in the tank was drained and the parts were moved out of the tank with the substrate attached for post-processing, which includes bulk drying to eliminate the remaining water content inside the parts and oil on the parts' surface, followed by debinding, decomposing of support material, and sintering.

Bulk drying was done by placing the parts in an environmental chamber (LH-1.5, Associated Environmental Systems, Ayer, MA, USA), where the relative humidity and temperature were controlled at 75% and 25 °C, for 12 h. The high humidity in the chamber provided a low drying rate so that warpage and crack formation were avoided to

produce crack-free green parts. Once dried, the part was readily separated from the substrate.

The green parts were then placed in a furnace (Deltech Inc., Denver, CO, USA), heated to 500 °C and held for 1 h to remove the binder content. The parts were next heated to 1500 °C and held for 1 h for sintering. The main material, Al_2O_3, would be densified, while the $CaCO_3$ support material was expected to decompose to form calcium oxide (CaO) and carbon dioxide (CO_2) and then to be removed from the part by immersing in water or acid solution to dissolve CaO. However, after sintering, the sparse support structure was not seen and a translucent, melted material was observed at the location of the support structure. The melted material was believed to be calcium aluminate ($mCaO·nAl_2O_3$), the product of the reaction between CaO and Al_2O_3. Depending on the concentrations of CaO and Al_2O_3, the melting point of calcium aluminate varies between 1360 and 2570 °C [15]. Hence the calcium aluminate could be formed and melted at the 1500 °C sintering temperature. The reaction between CaO an Al_2O_3 consumed the main structure, and the produced calcium aluminate flowed after melting, damaging the sintered part.

Knowing that the $CaCO_3$ starts decomposing at 850 °C and the alumina green body starts densifying at 980 °C [16], a two-step sintering method was developed to prevent the formation of glassy calcium aluminate. The 1st step of sintering held the temperature at 500 °C for 1 h for the purpose of debinding, then the furnace temperature was increased to 950 °C and held for 0.5 h to allow the $CaCO_3$ to decompose. The furnace temperature was then increased to 1100 °C with a 1 h hold for sintering of Al_2O_3. At this point, partially densified Al_2O_3 and porous CaO structures were obtained.

Although not fully densified, the Al_2O_3 structures exhibited sufficient strength for safe removal of the support structures. The cooled part was then placed into hydrochloric acid or water for about 30 seconds to dissolve the CaO support. The 2nd step of sintering then followed by heating the part to 1500 °C with a 1 h hold to obtain the dense ceramic part. The above procedure is illustrated in Figure 5. Another sample part, the turbine-blower housing, was processed in the same manner and two photos of the sintered turbine-blower housing are shown in Figure 6.
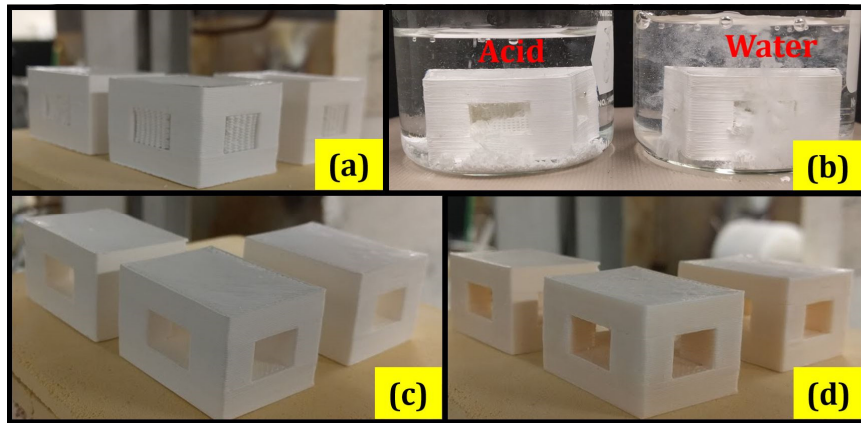
Figure 5. Two-step sintering and support structure removal: (a) Three parts in a furnace after 1st-step sintering, (b) Support structures being dissolved by hydrochloric acid or water, (c) Cleaned parts ready for 2nd- step sintering, (d) Parts obtained after two-step sintering.
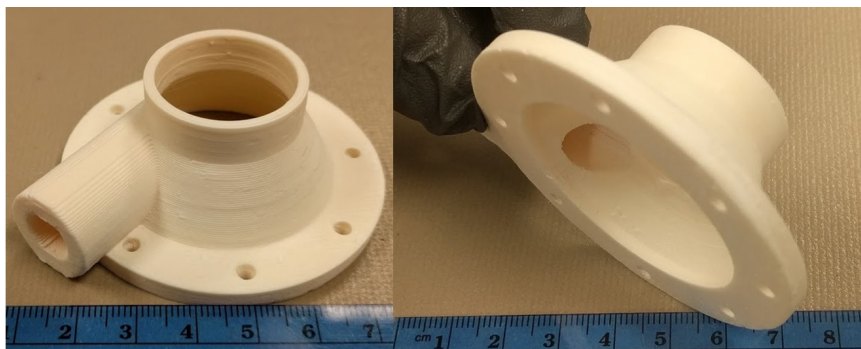
Figure 6. Final turbine-blower housing part after sintering.

4. PART CHARACTERIZATION AND DISCUSSION

4.1. CHARACTERIZATION OF PARTS

Key dimensions of the sample parts are provided on CAD models in Figure 7. Note that the dimensions D1, D2, D3 in Figure 7(b) are the outer diameters of the cylindrical features. The key dimensions were measured from the sintered parts and compared to the nominal values to evaluate the part shrinkage.
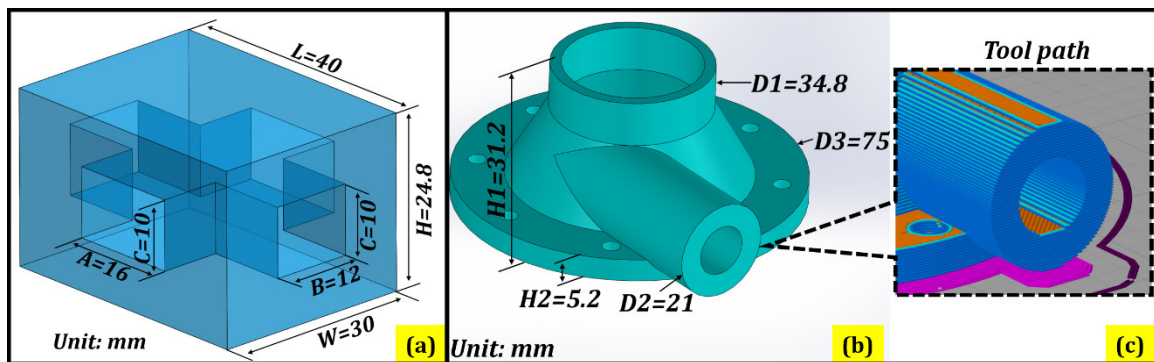
Figure **7.** CAD models: (a) Cuboid part, (b) Turbine-blower housing part, (c) Partial view of tool path for the horizontal cylindrical feature in (b).

4.1.1. Characterization of Cuboid Sample Parts. After the five cuboid parts were sintered, their key dimensions were measured. For each dimension in each part, six measurements were taken at random locations, and the mean values are provided in Table 2, followed by the standard deviations. The corresponding shrinkage rates in the sintered parts comparing to the CAD model were calculated and listed under the standard deviation values. The overall mean values and average shrinkage rates comparing to the CAD model are given at the bottom of Table 2. The five parts are denoted by #1 - #5 in this table.

Table 2. Measurements for cuboid parts after sintering.

Measurements		L (mm)	W(mm)	H(mm)	A(mm)	B (mm)	C(mm)
#1	Mean Std. Dev.	33.7 0.14	25.2 0.18	20.5 0.15	13.4 0.05	10.2 0.11	8.2 0.07
	Shrinkage	15.9%	16.1%	17.5%	16.0%	15.3%	17.8%
#2	Mean Std. Dev.	33.7 0.10	25.2 0.18	20.5 0.11	13.4 0.06	10.2 0.11	8.2 0.04
	Shrinkage	15.9%	16.1%	17.4%	16.3%	15.4%	17.8%
#3	Mean Std. Dev.	33.6 0.11	25.1 0.24	20.4 0.12	13.5 0.17	10.1 0.04	8.2 0.06
	Shrinkage	16.0%	16.4%	17.8%	15.4%	15.7%	18.0%
#4	Mean Std. Dev.	33.5 0.19	25.1 0.15	20.4 0.07	13.5 0.07	10.2 0.06	8.2 0.06
	Shrinkage	16.2%	16.5%	17.6%	15.5%	15.0%	18.2%
#5	Mean Std. Dev.	33.6 0.15	25.1 0.29	20.4 0.07	13.4 0.05	10.2 0.04	8.2 0.06
	Shrinkage	16.1%	16.3%	17.6%	16.0%	15.1%	18.0%
All	Mean	33.6	25.1	20.4	13.5	10.2	8.2
	Shrinkage	16.0%	16.3%	17.6%	15.9%	15.3%	18.0%

4.1.2. Characterization of The Turbine-blower Housing Part. The key dimensions of the turbine-blower housing part were measured after sintering. Each dimension was measured at ten random locations. The measured data are presented and statistically summarized in Table 3. The bulk density of the part was determined by Archimedes' method as 3.88 g/cm3, which is 97.5% of theoretical density.

Table 3. Measurements for turbine-blower housing part after sintering.

Measurements	H1(mm)	H2(mm)	D1(mm)	D2(mm)	D3(mm)
1	25.6	4.2	29.4	17.0	63.8
2	25.7	4.2	29.3	17.5	63.7
3	25.7	4.2	29.3	17.6	63.7
4	25.6	4.3	29.2	17.6	63.7
5	25.5	4.3	29.2	17.7	63.7
6	25.5	4.3	29.2	17.8	63.7
7	25.4	4.3	29.2	17.8	63,7
8	25.5	4.4	29.4	17.8	63.7
9	25.5	4.4	29.3	17.6	63.8
10	25.5	4.3	29.3	17.5	63.8
Mean	25.6	4.3	29.3	17.6	63.7
Std. Dev.	0.09	0.07	0.07	0.23	0.05
Shrinkage	18.1%	17.5%	15.9%	16.2%	15.0%
Max.	25.7	4.4	29.4	17.8	63.8
Min.	25.4	4.2	29.2	17.0	63.7

4.2. DISCUSSION

In Table 2, the standard deviations of the measured values for the six key dimensions varied between 0.3% and 1.3%, and the shrinkage rates of the five sintered final parts were in the range of 15-19%. In Table 3, the shrinkage rates of the five key dimensions on the sintered turbine-blower housing were also in the range of 15-19%. The diameters of two vertical cylindrical features, i.e., D1 and D3, have standard deviations of 0.26% and 0.07%, respectively, indicating a good circularity of these two cylindrical features. The dimension D2 in Table 3 has a higher standard deviation (1.3%) than the other dimensions measured. This large variation is reasoned to be a result of the staircase

effect error due to CAD model slicing and layer building. A partial view of the staircase effect on the horizontal tube-shaped feature which affected the D2 values is shown in Figure 7(c). The staircase effect error decreases as the nozzle diameter and layer thickness decrease. The nozzle diameter and layer thickness we used here are 610 μm and 400 μm, respectively, as given in Table 1. The minimum line spacing and layer thickness that can be used in the CODE process for the alumina paste based on our experimental investigation is 150 μm and 100 μm, respectively.

Further examination of the shrinkage rates of the dimensions in Tables 2 and 3 reveals that the vertical dimensions, i.e., H, C in Tables 2 and H1, H2, D2 in Table 3, exhibit higher shrinkage rates than the horizontal dimensions. The anisotropic shrinkage is probably caused by the effect of gravity during drying and sintering. However, further evidence is required to confirm this conjecture.

The relative density of CODE fabricated ceramic parts with a rectangular shape was determined to be 98% in our previous studies [12,13]. In the current study, the relative density of the sintered turbine-blower housing was determined to be 97.5%. The fabrication of a geometrically complex part such as this housing consisting of numerous extrusion starts and stops would have been expected to have a decreased density compared to simple geometries. However, the density of the turbine-blower housing in this study was essentially the same as the density of the simple- shaped part, indicating precise control of paste extrusion in the CODE process.

From the above results, the $CaCO_3$ paste has been validated as a sacrificial support material in the CODE process, and it can be readily removed by dissolving in acid or water. For the fabricated Al_2O_3 parts, two-step sintering is needed for support

structure removal. Compared to other potential sacrificial materials such as wax, thermoplastic, and light curable polymer, a major advantage of using $CaCO_3$ as sacrificial material is that no auxiliary devices such as a heating, light curing or freezing apparatus are required.

5. CONCLUSION

A method of fabricating ceramic components by the Ceramic On-Demand Extrusion (CODE) process with the use of sacrificial support material has been developed. Calcium carbonate ($CaCO_3$) was identified as a sacrificial material. Geometrically simple and complex sample parts were successfully fabricated using Al_2O_3 as the main material and with $CaCO_3$ as the support material.

A support material removal process was developed by using two-step sintering. The $CaCO_3$ support material was removed by dissolving in acid solution or water after the 1st-step sintering at 1100 °C, and then the parts went through the 2nd-step sintering at 1500 °C to obtain the dense ceramic parts. A geometrically complex Al_2O_3 turbine-blower housing achieved 97.5% relative density after the 2nd-step of sintering.

The dimensional shrinkage rates for the sintered parts compared to the CAD model were in the range of 15-19%. The shrinkage in the vertical direction was higher than that on the horizontal plane. The two vertical cylindrical features of the Al_2O_3 turbine-blower housing fabricated by the CODE process had standard deviations of 0.26% and 0.07% in diameter, and the horizontal cylindrical feature had a standard deviation of 1.3% in diameter, indicating good circularity.

ACKNOWLEDGMENTS

REFERENCES

[1]   Miyanaji H, Zhang S, Lassell A, Zandinejad A, Yang L (2016). Process development of porcelain ceramic material with binder jetting process for dental applications. Journal of The Minerals, Metals & Materials Society, 68(3), pp.831-841.

[2]   Cesarano J, Segalman R, Calvert P (1998) Robocasting Provides Moldless Fabrication from Slurry Deposition. Ceramic Industry, 148(4).

[3]   Agarwala MK, Weeren RV, Bandyopadhyay A, Whalen PJ, Safari A, Danforth SC (1996) Fused Deposition of Ceramics and Metals: An Overview. Proceedings of Solid Freeform Fabrication Symposium, Austin, Texas.

[4]   Luo J, Pan H, Kinzel EC (2014) Additive Manufacturing of Glass. Journal of Manufacturing Science and Engineering, 136 (6): 061024.1-6.

[5]   Hon KKB, Li L, Hutchings IM (2008) Direct Writing Technology—Advances and Developments. CIRP Annals-Manufacturing Technology, 57(2), pp.601-620.

[6]   Leu MC, Deuser BK, Tang L, Landers RG, Hilmas GE, Watts JL (2012) Freeze-form Extrusion Fabrication of Functionally Graded Materials. CIRP Annals-Manufacturing Technology, 61(1), pp.223-226.

[7]   Schwentenwein M, Homa J (2015) Additive Manufacturing of Dense Alumina Ceramics. International Journal of Applied Ceramic Technology, 12(1), pp.1-7.

[8]   Bertrand P, Bayle F, Combe C, Goeuriot P, Smurov I (2007) Ceramic Components Manufacturing by Selective Laser Sintering. Applied Surface Science, 254(4), pp.989-992.

[9]   Wilkes J, Hagedorn YC, Meiners W, Wissenbach K (2013) Additive
        Manufacturing of ZrO_2-Al_2O_3 Ceramic Components by Selective Laser Melting.
        Rapid Prototyping Journal, 19(1), pp.51-57.

[10]   Niu F, Wu D, Ma G, Wang J, Zhuang J, Jin Z (2016). Rapid Fabrication of
        Eutectic Ceramic Structures by Laser Engineered Net Shaping. Procedia CIRP,
        42, pp.91-95.

[11]   Ghazanfari A, Li W, Leu MC, Hilmas GE (2016) A Novel Extrusion-based
        Additive Manufacturing Process for Ceramic Parts. Proceedings of Solid
        Freeform Fabrication Symposium, Austin, TX.

[12]   Li W, Ghazanfari A, McMillen D, Leu MC, Hilmas GE, Watts JL (2016)
        Properties of Partially Stabilized Zirconia Components Fabricated by the Ceramic
        On-Demand Extrusion Process. Proceedings of Solid Freeform Fabrication
        Symposium, Austin, TX.

[13]   Ghazanfari A, Li W, Leu MC, Watts JL, Hilmas GE (2017) Mechanical
        Characterization of Parts Produced by Ceramic On‑Demand Extrusion Process.
        International Journal of Applied Ceramic Technology.

[14]   Li W, Ghazanfari A, Leu MC, Landers RG (2015) Methods of Extrusion On
        Demand for High Solids Loading Ceramic Paste in Freeform Extrusion
        Fabrication. Proceedings of Solid Freeform Fabrication Symposium, Austin, TX.

[15]   Alcoa Corporation (1996) High Alumina Cements & Chemical Binders. Available
        at: http://www.almatis.com/media/3986/high-calcium-aluminate-
        cements_and_chemical_binders.pdf [Accessed March 10, 2017].

[16]   Lin FJ, Jonghe LC, Rahaman MN (1997) Microstructure Refinement of Sintered
        Alumina by a Two‑Step Sintering Technique. Journal of the American Ceramic
        Society, 80(9), pp.2269-2277.

IV. FABRICATING FUNCTIONALLY GRADED MATERIALS BY CERAMIC ON-DEMAND EXTRUSION WITH DYNAMIC MIXING

ABSTRACT

Ceramic On-Demand Extrusion (CODE) is an extrusion-based additive manufacturing process recently developed for fabricating dense, functional ceramic components. Presented in this paper is a further development of this process focusing on fabrication of functionally graded materials (FGM). A dynamic mixing mechanism was developed for mixing constituent ceramic pastes, and an extrusion control scheme was developed for fabricating specimens with desired material compositions graded in real time. FGM specimens with compositions graded between Al_2O_3 and ZrO_2 were fabricated and ultimately densified by sintering to validate the effectiveness of the CODE process for FGM fabrication. Energy dispersive spectroscopy (EDS) was used to compare final compositions to the original material designs. The specimen's hardness at different locations along the gradients was examined by micro-indentation tests. The dimensions of sintered specimens were measured, and the effects of material composition gradients on the distortion of sintered FGM specimens were analyzed.

1. INTRODUCTION

Several additive manufacturing (AM) processes have been developed for ceramics and glasses, including binder jetting [1], [2], material extrusion [3]–[8], vat photopolymerization [9], [10], powder bed fusion [11, 12], and directed energy

deposition [13–15], among others. Ceramic On-Demand Extrusion (CODE) [7] is a recently developed paste extrusion-based AM process, which produces ceramic components with near theoretical density (>98%) after sintering [4, 16–18]. It deposits high solids loading (>50 vol%) aqueous ceramic pastes onto a substrate layer by layer at room temperature. Each deposited layer is partially solidified by uniform infrared radiation drying from above before the subsequent layer is initiated. At the same time, undesirable evaporation from the sides of the part is prohibited by surrounding the part with a liquid [7]. This layered uniform radiation drying approach minimizes the moisture content gradient in the part during the fabrication process and thus enables CODE to produce crack-free ceramic parts. The printed parts are then bulk-dried in a controlled environment with appropriate humidity, after which the green bodies are sintered to produce near-theoretical density parts [16–18].

Functionally graded materials (FGM) are characterized by gradual variations of material compositions over volumes, which allows for a combination of materials or material properties not typically achievable in monolithic materials [19]–[22]. Alumina/zirconia (Al_2O_3/ZrO_2) FGM components have been of great interest, mainly to enhance the fracture toughness through the incorporation of a partially stabilized ZrO_2 phase. One potential application is the prosthetic hip joint ball [22, 23], where the FGM realizes the transition from a tough ZrO_2 core, which provides the high strength of the hub structure and reduces the risk of cracking, to a more wear-resistant Al_2O_3 ball surface, which guarantees a long service life in a human body. Additive manufacturing (AM) processes are especially advantageous for fabricating FGM components due to the layer-by-layer nature of the processes. Considering that the melting temperatures of

ceramics are usually too high for thermal-based melt deposition and the fact that the ink jetting-based ceramic AM processes are subject to high porosity [20], material extrusion-based AM processes are the most favorable method for fabricating ceramic FGM components [20].

The present paper introduces a dynamic mixing device to the Ceramic On-Demand Extrusion (CODE) system for fabricating FGM specimens. Two distinct materials were extruded through separate extruders into the mixing chamber of the dynamic mixer with controlled flow rates. The pastes were then blended by the dynamic mixer to produce a homogenous mixture and finally deposited through nozzles to fabricate FGM specimens with planned material compositional distribution. The FGM specimens were post-processed and characterized to validate the functionality and accuracy of the dynamic mixing device. Deformation was observed on the sintered specimens. The effects of material composition gradients on the deformation of sintered FGM specimens were analyzed.

2. EXPERIMENTAL SETUP

The CODE fabrication system consists of a cartesian gantry system, an extrusion device mounted on the gantry and capable of extruding viscous ceramic pastes at controlled flow rates, an oil feeding device to regulate the oil level in the tank, and an infrared radiation heating device capable of positioning the infrared source and providing on/off control. Introduction and details of the CODE fabrication system were presented in previous papers [4, 7, 24]. In the present work, the CODE system was configured to

deposit a mixture of two materials using a dynamic mixing tool head consisting of two auger extruders and a dynamic mixer. The two auger extruders were controlled separately to extrude two different pastes at independent flow rates. As shown in

Figure 1(a), the two pastes are extruded through the inlets into the dynamic mixer. As the two pastes passed through the mixing chamber, a motor-driven mixing blade blended the distinct pastes to produce a homogenous mixture, which was then deposited through the outlet to form a 3D part. The actual components and layout of the dynamic mixing tool head are shown in Figure 1(b).

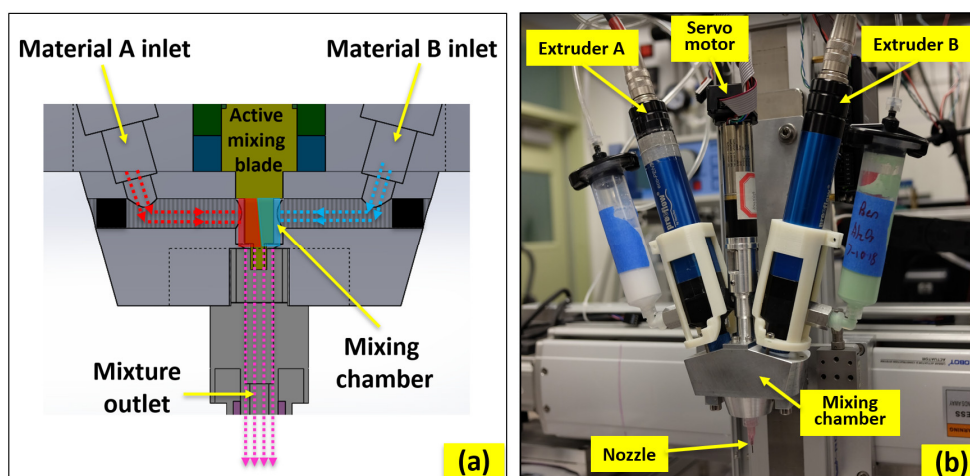Figure 1. Dynamic mixing tool head of the CODE system. (a) Schematic of the dynamic mixer, (b) The actual dynamic mixing tool head mounted on the CODE system.

3. FABRICATION OF FUNCTIONALLY GRADED MATERIALS

3.1. PREPARATION OF PASTES

Aqueous Al_2O_3 pastes and ZrO_2 (3Y) pastes were prepared as the feedstock materials. The composition of the pastes and detailed steps of paste formation can be

found in previous studies [16, 17]. The ZrO_2 pastes were prepared to have 50 vol% solids loading. Considering the shrinkage of components during the bulk drying process and the sintering process, the Al_2O_3 pastes were also adjusted to have 50 vol% solids loading, expecting to minimize the mismatch of shrinkage between the two materials, and hence minimize the distortion of the FGM specimens during sintering. In order to visualize the material variation in the printed specimens, the white Al_2O_3 pastes and ZrO_2 pastes were colored green and pink, respectively, using FD&C Yellow 5 & Blue 1 and FD&C Red 40 dyes.

3.2. PRINTING SINGLE-BEAD LINES WITH GRADED MATERIALS

To test the capability of the dynamic mixing tool head to build parts with graded materials and examine the response of changing material composition, a single-bead serpentine shape was printed using both the ZrO_2 paste (pink) and the Al_2O_3 paste (green). The ZrO_2 and Al_2O_3 pastes were extruded by extruders A and B, respectively. As shown in Figure 2, the dynamic mixing tool head was first loaded with ZrO_2 paste and was then commanded to switch to Al_2O_3 paste by turning off extruder A and turning on extruder B at location 1. The serpentine shape was printed from location 1 to location 5, during which the dynamic mixing tool head was commanded to switch between ZrO_2 and Al_2O_3 at locations 2, 3, and 4. The mixing blade was spinning at 900 rpm during the entire printing process. As expected, the change in material didn't take place immediately after receiving the control commands at locations 1-4. Instead, a delay was observed before the printed line changed color.
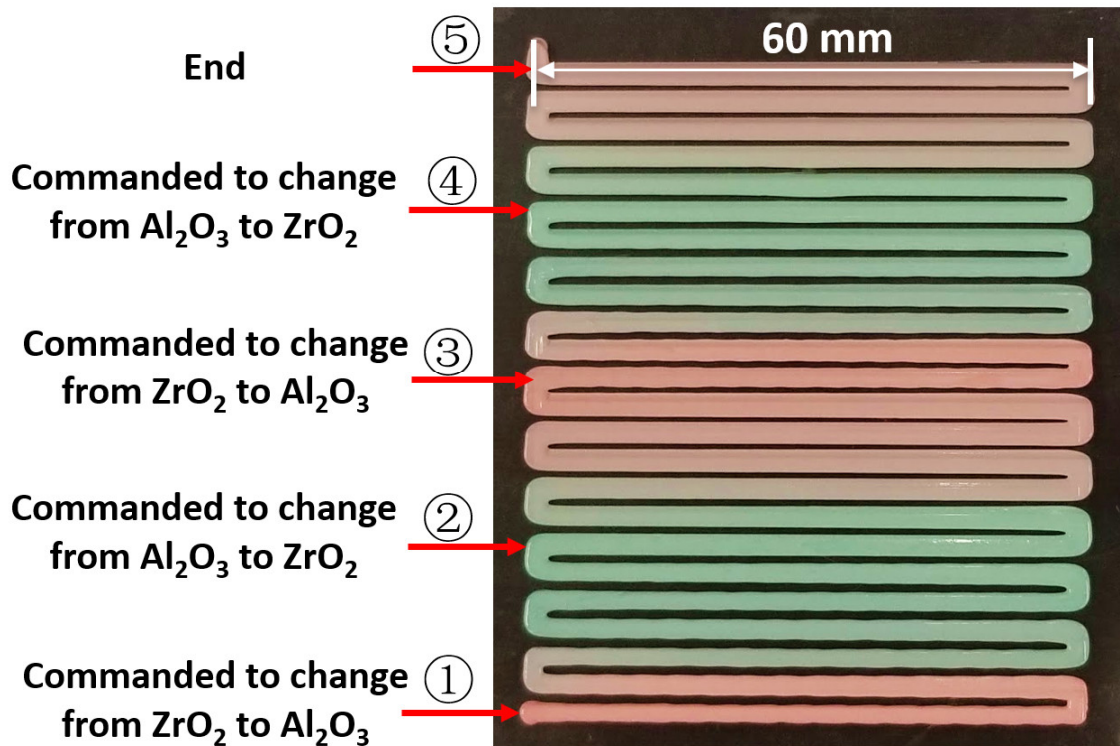
Figure 2. A single-bead serpentine printed using dynamic mixing device with graded materials (pink: ZrO_2, green: Al_2O_3). The mixing blade was spinning at 900 rpm during the entire printing process.

4. DETERMINING THE DELAY OF CHANGING MATERIAL COMPOSITION

The dried serpentine shaped specimen is shown in Figure 2 and Figure 3(a). The colors in Figure 3(a) indicated that the material composition changed periodically in four cycles as commanded. The pattern of material color change was similar in each cycle, indicating that the delay in composition transition was repeatable. Other than observing the material composition variation visually by color, EDS was also utilized on sintered specimens to obtain detailed measurements of composition at locations of interest. As shown in Figure 3(b), 42 locations of interest in cycle 1 were selected for EDS measurements. Locations 1 and 42 were the starting and ending locations of cycle 1, i.e.,

the locations where the tool head was commanded to switch from one material to another. The EDS measurements were taken at the surface of the specimen. At each location, the EDS measurement covered three areas of $\sim$ 120 µm by 120 µm. The percentages of Al atomic counts over the total atomic counts of Al, Zr, and Y of the three sampling areas for all locations are plotted in Figure 3(c). According to the graph in Figure 3(c), after the command to change material was received at location 1, the actual material composition started to change at location 7, and gradually transitioned to the desired material composition (100% Al_2O_3). Location 38 was determined as the location where the transition of composition was completed. The stable material composition between locations 1 and 7 was characterized as the result of purging out the residual ZrO_2 paste in the material outlet (shown in Figure 3 (a)). The volume of paste being deposited between locations 1 and 7 was termed the 'delivery delay'. On the other hand, the volume of paste being deposited between locations 7 and 38 was termed the 'transition delay', which was related to the propagating behavior of the paste streams in the flow path of the mixer, and the volume of the flow path. The delivery delay and the transition delay made up the total delay when changing material composition, and their volumes were quantified as 0.12 mL, 0.36 mL, and 0.48 mL, respectively. As expected, the delivery delay (0.12 mL) was equal to the volume of the material outlet of the mixer. In the practice of printing laminar FGM samples, the total delay (V_{delay}) was considered in the control scheme, and proper compensation was made to precisely deposit materials with desired compositions.
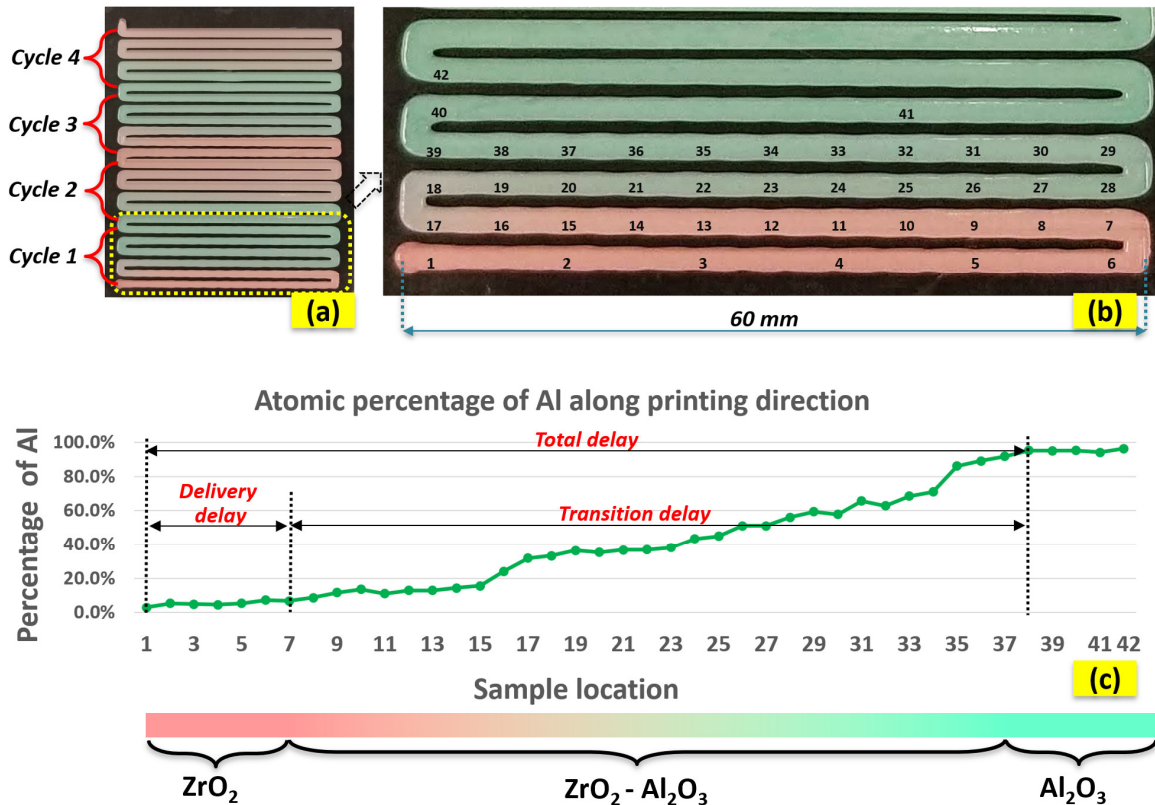
Figure 3. (a) Four cycles of the printed serpentine. (b) 42 sampling locations for EDS test on cycle 1 of the serpentine. (c) The atomic percentage of Al measured by EDS at different locations.

5. FABRICATING LAMINAR Al₂O₃/ ZrO₂ FGM SPECIMENS

To examine the ability of the dynamic mixing tool head to accurately control the material composition, and to study the drying and sintering behavior of bulk FGM specimens, three groups of laminar FGM specimens graded from Al_2O_3 to Al_2O_3/ZrO_2 (50/50) were fabricated. Each group had three samples with different material gradients. The material gradient for the three types is shown in Figure 4. Type 1 had a 5 vol% increment of ZrO_2 every layer and hence grads from Al_2O_3 to Al_2O_3/ZrO_2 via ten steps through 11 layers. Type 2 had a 10 vol% increment of ZrO_2 every two layers hence

changes from Al$_2$O$_3$ to Al$_2$O$_3$/ZrO$_2$ via five steps through 11 layers. Finally, Type 3 was

changed from Al$_2$O$_3$ directly to Al$_2$O$_3$/ZrO$_2$ at the 6th layer of the 11-layer sample. All the

FGM specimens were designed to have identical dimensions (70×20×6.6 mm^3) and

numbers of layers to ensure a fair comparison of potential part deformation after

sintering.
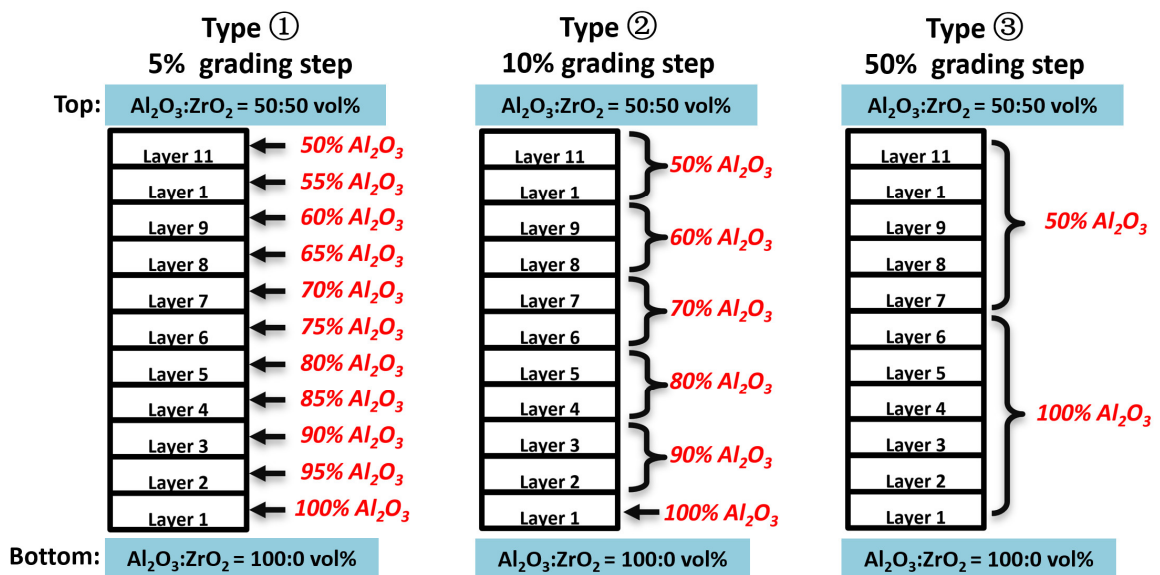
Figure 4. Design of material composition distribution in three types of FGM specimens.

Considering the significant delay (V_{delay} = 0.48 mL) to the change in composition

discussed in the previous section, each time a change of composition in a new layer was

required, an additional purging process was conducted before the new layer was started.

In the purging process, the dynamic mixing tool head was commanded to move out of the

building substrate, extrude two pastes at predetermined flow rates for a certain volume

V_{purge} until the materials at the nozzle tip reached the desired steady composition ($V_{purge} \geq$

V_{delay}), and was finally moved back to the building substrate to start the new layer. The

entire printing and purging process was fully automated by G-Codes. A V_{purge} of 0.5 mL

was used in this experiment. The printed FGM specimens were bulk dried in an environmental chamber for 12 hours where the temperature was controlled at 24°C and the relative humidity at 75%, then fired at 500°C for 1 hour to burn out the organic constituents including binder and dyes, and finally sintered at 1500°C for 1 hour for densification. The sintered specimens were characterized, and the result is presented in the following section. Figure 5 shows the printing process of an FGM specimen and dried FGM specimens of three types.
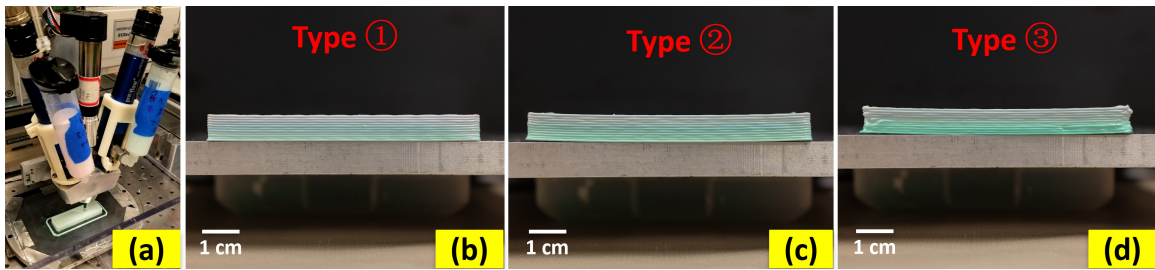
Figure 5. (a) A laminar Al_2O_3/ZrO_2 FGM specimen being printed using the dynamic mixing tool head. (b) (c) (d) A group of laminar Al_2O_3/ZrO_2 FGM specimens printed and dried.

6. RESULTS AND DISCUSSION

6.1. ACCURACY OF MATERIAL COMPOSITION CONTROL

Two sintered FGM specimens from Type 1 were cut, and ground from the side for ~ 4 mm to reveal the inner cross-section as illustrated in Figure 6(b), then polished down to a 0.25-micron finish and coated with gold/palladium for EDS measurements. For all 11 layers in the two specimens, EDS intensity measurements were taken over three regions with aproximately120 µm by 120 µm areas. The ratio of Al peak vs. Zr peak, as well as the SEM images of two example layers, are shown in Figure 6(c)(d). The dark (Al_2O_3)

and bright (ZrO_2) phases in the SEM images show a homogeneous distribution of the two materials.
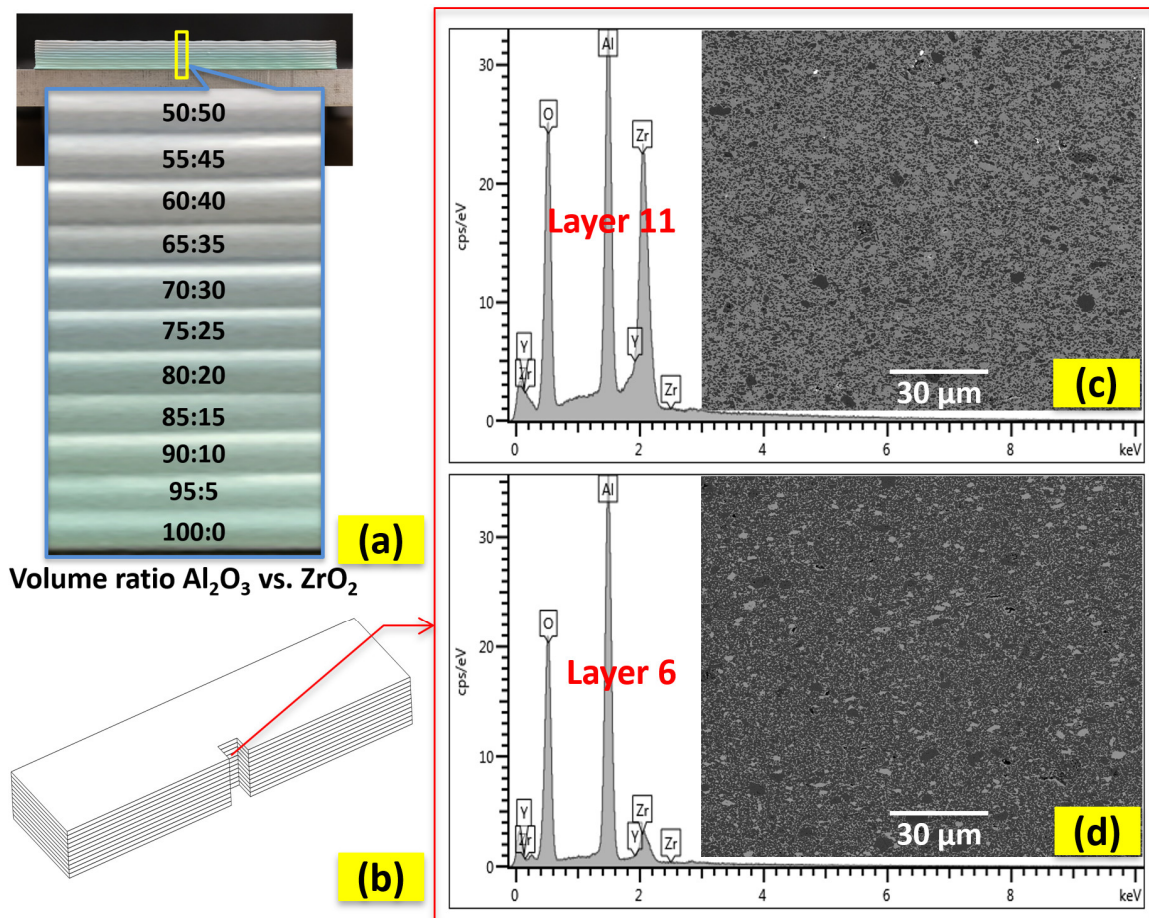
Figure 6. (a) A photo of a dried (not sintered) FGM specimen of Type 1, and a close-up view showing a color change of its layers. (b) Schematic showing the cross-section where EDS measurements were taken. (c) (d) EDS peaks and SEM images taken from layer 11 and 6 of the specimen.

The mean values of the measured atomic percentage of Al for layers 1-11 were plotted in Figure 7 by the solid line. Based on the designed volume ratio of the Al_2O_3 and ZrO_2 pastes, the solids loading of two pastes, density and molecular weight of the two materials, the nominal atomic percentages of Al in all layers were calculated and plotted

in Figure 7 by the dashed line. The average error between the measured value and nominal value was 1%, and the maximum discrepancy was 2%, indicating good accuracy of the dynamic mixing tool head for controlling material composition.
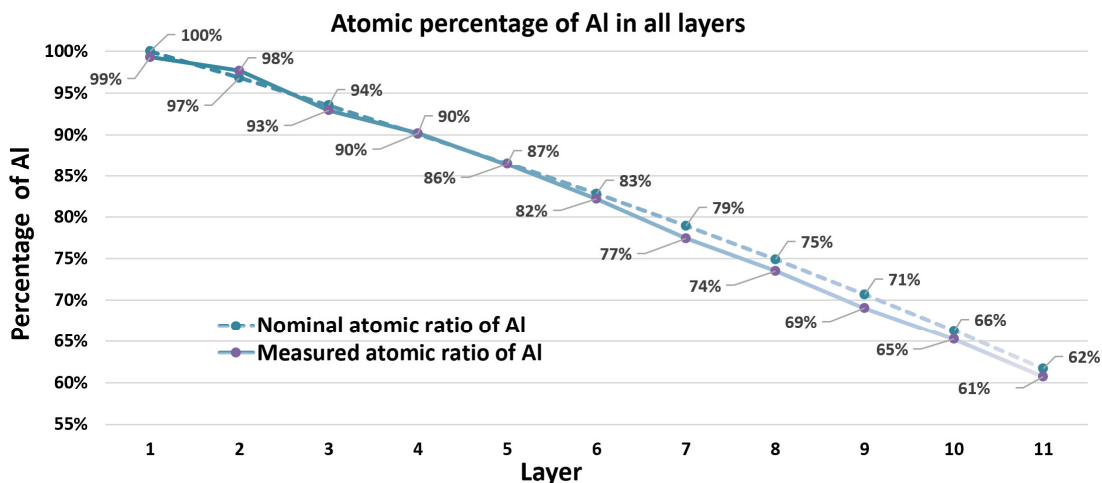
Figure 7. The atomic percentage of Al of each layer in the sintered FGM specimens.

6.2. DEFORMATION OF SPECIMENS

After sintering, the three groups of colored Al_2O_3/ZrO_2 specimens turned white since the organic dyes burned out during the firing process. Curling and delamination were observed in the sintered specimens. In order to quantify the deformation of each specimen, as shown in Figure 8, the specimens were flipped on a flat substrate to measure the heights at their center and two ends, from which the curling angles were calculated for every specimen. The quantified deformation of all FGM specimens is reported in Table 1.
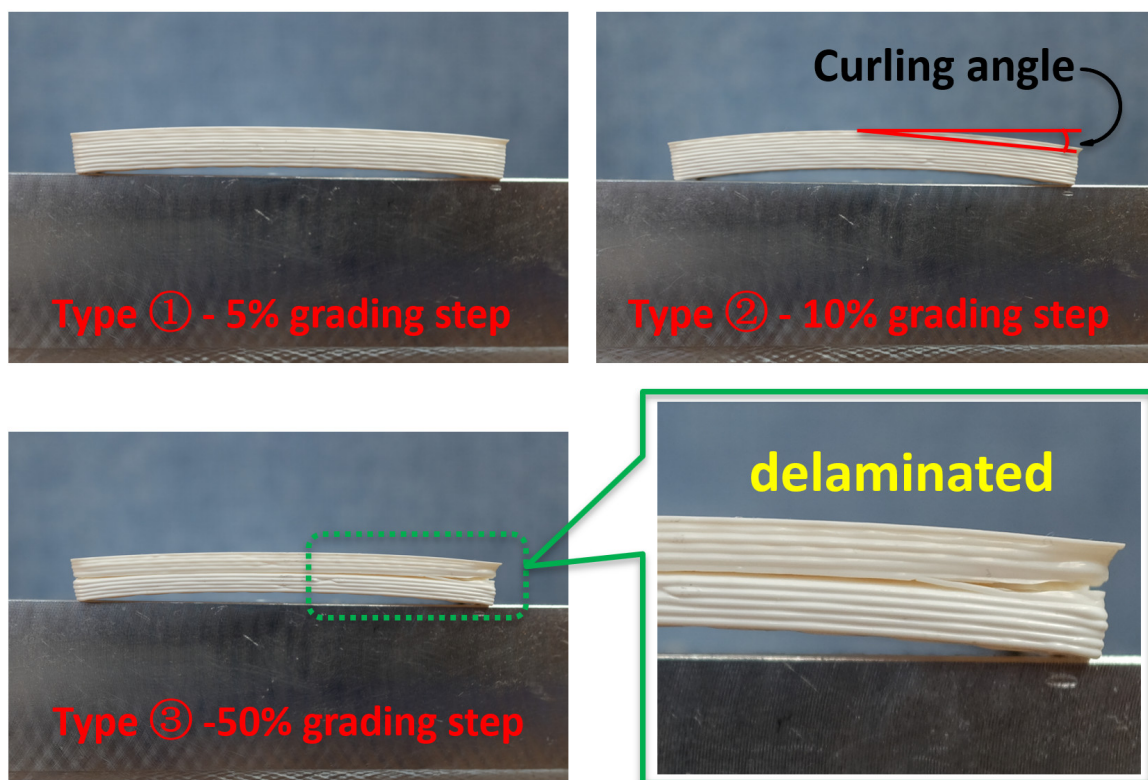
Figure 8. One group of FGM specimens after sintering, deformation, and failure were observed.

Table 1. Quantified deformation (curling angle) of each FGM specimen after sintering.

Grading Step	Curling Angle		
	Group 1	Group 2	Group 3
5% (Type 1)	2.7°	2.3°	2.9°
10% (Type 2)	3.6°	3.8°	3.7°
50% (Type 3)	4.9° (cracked)	delaminated	delaminated

6.3. VICKERS HARDNESS

A sintered FGM specimen from Type 2 was cut, ground and polished in a similar way illustrated in Figure 8(b). Micro-indentation tests were performed at layers with different material compositions following ASTM C1327 standard [26]. For each layer

with different compositions, five indentations were performed at different locations, and the mean values of Vickers hardness are presented in Table 2, as well as their standard deviations.

Table 2. Vickers hardness of layers with different composition of Al_2O_3/ZrO_2 in an FGM specimen.

Layer	Volume ratio of Al_2O_3 vs. ZrO_2	Vickers Hardness (*GPa*)	
		Mean	Standard Deviation
10-11	50%:50%	15.0	0.31
8-9	60%:40%	16.0	0.23
6-7	70%:30%	16.3	0.14
4-5	80%:20%	16.9	0.41
2-3	90%:10%	17.5	0.28
1	100%:0%	18.4	0.32

7. DISCUSSION

Due to the delay of changing material composition using the dynamic mixing tool head, time and material waste are introduced to the printing of laminar FGM specimens when pastes are purged out before they reach a desired stable composition for a new layer. Moreover, the transition delay also limits the accuracy of controlling the in-plane gradient of composition in one layer. Minimizing the delay is always desirable for fabricating FGM components. The key point of minimizing the delay is to reduce the volume of the flow path. However, tighter flow path leads to an increase of back pressure, which requires higher extrusion pressure, especially for highly-viscous ceramic

pastes. In addition, the fabrication of micro-sized mixing blades and flow paths is also challenging. A trade-off between the fast transition of composition and equipment investment is necessary, which will be investigated in the future, as well as the overall design of the dynamic mixer.

According to Figure 8 and Table 1, as the step of changing composition increased, the amount of deformation of the sintered FGM specimen increased until structural failure (cracking and delamination) took place. Although less significant, a similar trend of deformation was also observed on the FGM specimens after they were bulk dried, as shown in Figure 5(b)(c)(d). The deformation occurred during the bulk drying process indicated a mismatch in drying shrinkage of the two pastes. Since the two pastes had the same (50 vol%) solids loading, the difference in shrinkage was believed to be caused by the different packing density of the particles in the two pastes after they were dried. On the other hand, the deformation occurred during the sintering process was believed to be caused by the mismatch of sintering shrinkage and thermal expansion of Al_2O_3 and ZrO_2. Larger differences in material composition between layers lead to larger stresses caused by the mismatch of material properties, which explains the fact that the larger step of changing composition led to larger amounts of deformation. A smoother (reduced) gradient of material composition is likely to reduce the amount of deformation and the risk of part failure. Adjusting the inherent properties of the raw materials to reduce the mismatch of shrinkage could be another effective way of mitigating the stress and deformation. For example, according to the study of Sun et al. [27], adjusting the particle size distribution of the Al_2O_3 and ZrO_2 powders could contribute to matching the shrinkage of layers with different Al_2O_3/ZrO_2 ratios in the FGM specimens.

SEM images taken at the cross-section of the FGM specimens, of which two example images are shown in Figure 6, demonstrated a high homogeneity of the mixed Al_2O_3 and ZrO_2 phases. Vickers hardness reported in Table 2 demonstrated a clear trend of decreased hardness as the ZrO_2 concentration was increased. The hardness values were in good agreement with data reported from other literature [27–29]. The hardness measurements at different locations for each composition were highly consistent according to their standard deviations, which is further evidence that the Al_2O_3 and ZrO_2 pastes were highly homogeneous.

8. CONCLUSIONS

A dynamic extrusion-mixing device was developed for fabricating functionally graded materials (FGM) by the Ceramic On-Demand Extrusion process. The effectiveness of this device was validated by fabricating FGM specimens graded from pure Al_2O_3 to Al_2O_3/ZrO_2 with predetermined material gradients. The FGM specimens were sintered at 1500 °C and the material composition of each layer in the sintered FGM specimens was validated by measuring the atomic percentage of Al and Zr by energy dispersive spectroscopy (EDS) and compared to the original design of compositions. A 1% average error of material composition was observed from the comparison. Deformation was measured on the dried and sintered FGM specimens. Greater material composition gradients led to larger deformation of specimens. The Vickers hardness decreased from 18.4 GPa to 15.0 GPa as the volume percentage of ZrO_2 increased from 0 to 50 vol% in Al_2O_3/ZrO_2 layers.

ACKNOWLEDGMENTS

REFERENCES

[1]   S. Zhang, H. Miyanaji, L. Yang, A. Ali Zandinejad, J. Dilip, and B. Stucker, "An experimental study of ceramic dental porcelain materials using a 3D print (3DP) process," Proc. 25th Annu. Int. Solid Free. Fabr. Symp., pp. 991–1011, 2014.

[2]   H. Miyanaji, S. Zhang, A. Lassell, A. Zandinejad, and L. Yang, "Process development of porcelain ceramic material with binder jetting process for dental applications," J. Miner. Met. Mater. Soc., vol. 68, no. 3, pp. 831–841, 2016.

[3]   J. Cesarano, R. Segalman, and P. Calvert, "Robocasting provides moldless fabrication from slurry deposition," Ceram. Ind., vol. 148, no. 4, p. 94, 1998.

[4]   W. Li, A. Ghazanfari, D. McMillen, M. C. Leu, G. E. Hilmas, and J. Watts, "Fabricating ceramic components with water dissolvable support structures by the Ceramic On-Demand Extrusion process," CIRP Ann. - Manuf. Technol., vol. 66, no. 1, pp. 225–228, 2017.

[5]   M. Faes, J. Vleugels, F. Vogeler, and E. Ferraris, "Extrusion-based additive manufacturing of ZrO_2 using photoinitiated polymerization," CIRP J. Manuf. Sci. Technol., vol. 14, pp. 28–34, 2016.

[6]   K. K. B. Hon, L. Li, and I. M. Hutchings, "Direct writing technology—Advances and developments," CIRP Ann. - Manuf. Technol., vol. 57, no. 2, pp. 601–620, 2008.

[7]   A. Ghazanfari, W. Li, M. C. Leu, and G. E. Hilmas, "A novel freeform extrusion fabrication process for producing solid ceramic components with uniform layered radiation drying," Addit. Manuf., vol. 15, pp. 102–112, 2017.

[8]   J. Li, "An experimental study of fabrication temperature effect on aqueous extrusion freeform fabrication," Missouri University of Science and Technology, 2015.

[9]   M. Schwentenwein and J. Homa, "Additive manufacturing of dense alumina ceramics," Int. J. Appl. Ceram. Technol., vol. 12, no. 1, pp. 1–7, 2015.

[10]   T. Chartier, C. Chaput, F. Doreau, and M. Loiseau, "Stereolithography of structural complex ceramic parts," J. Mater. Sci., vol. 37, no. 15, pp. 3141–3147, 2002.

[11]   P. Bertrand, F. Bayle, C. Combe, P. Goeuriot, and I. Smurov, "Ceramic components manufacturing by selective laser sintering," Appl. Surf. Sci., vol. 254, no. 4, pp. 989–992, 2007.

[12]   N. Kang et al., "A novel approach to in-situ produce functionally graded silicon matrix composite materials by selective laser melting," Compos. Struct., vol. 172, pp. 251–258, 2017.

[13]   F. Niu, D. Wu, G. Ma, J. Wang, J. Zhuang, and Z. Jin, "Rapid fabrication of eutectic ceramic structures by laser engineered net shaping," Procedia CIRP, vol. 42, pp. 91–95, 2016.

[14]   F. Niu, D. Wu, G. Ma, J. Wang, M. Guo, and B. Zhang, "Nanosized microstructure of Al_2O_3-ZrO_2 (Y_2O_3) eutectics fabricated by laser engineered net shaping," Scr. Mater., vol. 95, no. 1, pp. 39–41, 2015.

[15]   F. Niu, D. Wu, G. Ma, and B. Zhang, "Additive manufacturing of ceramic structures by laser engineered net shaping," Chinese J. Mech. Eng., vol. 28, no. 6, pp. 1117–1122, 2015.

[16]   A. Ghazanfari, W. Li, M. Leu, J. Watts, and G. Hilmas, "Mechanical characterization of parts produced by ceramic on-demand extrusion process," Int. J. Appl. Ceram. Technol., vol. 14, no. 3, pp. 486–494, 2017.

[17]   W. Li, A. Ghazanfari, D. McMillen, M. C. Leu, G. E. Hilmas, and J. Watts, "Characterization of zirconia specimens fabricated by ceramic on-demand extrusion," Ceram. Int., vol. 44, no. 11, pp. 12245–12252, 2018.

[18]   A. Ghazanfari, W. Li, M. C. Leu, J. L. Watts, and G. E. Hilmas, "Additive manufacturing and mechanical characterization of high density fully stabilized zirconia," Ceram. Int., vol. 43, no. 8, pp. 6082–6088, 2017.

[19]   L. Yan, X. Chen, Y. Zhang, J. W. Newkirk, and F. Liou, "Fabrication of functionally graded Ti and γ-TiAl by laser metal deposition," JOM, vol. 69, no. 12, pp. 2756–2761, 2017.

[20]   L. Yang, H. Miyanaji, D. Janaki Ram, A. Zandinejad, and S. Zhang, "Functionally graded ceramic based materials using additive manufacturing: review and progress," Addit. Manuf. Strateg. Technol. Adv. Ceram., vol. 258, pp. 43–55, 2016.

[21]   W. Li, L. Yan, X. Chen, J. Zhang, X. Zhang, and F. Liou, "Directed energy depositing a new Fe-Cr-Ni alloy with gradually changing composition with elemental powder mixes and particle size' effect in fabrication process," J. Mater. Process. Technol., vol. 255, pp. 96–104, 2018.

[22]   Y. Li, Y. Shen, C.-H. Hung, M. C. Leu, and H.-L. Tsai, "Additive manufacturing of Zr-based metallic glass structures on 304 stainless steel substrates via V/Ti/Zr intermediate layers," Mater. Sci. Eng. A, vol. 729, pp. 185–195, 2018.

[23]   M. N. Rahaman, A. Yao, B. S. Bal, J. P. Garino, and M. D. Ries, "Ceramics for prosthetic hip and knee joint replacement," J. Am. Ceram. Soc., vol. 90, no. 7, pp. 1965–1988, 2007.

[24]   P. Muller, P. Mognol, and J.-Y. Hascoe, "Functionally graded material (FGM)parts: from design to the manufacturing simulation," Proc. ASME 2012 11th Bienn. Conf. Eng. Syst. Des. Anal., pp. 1–9, 2018.

[25]   W. Li, A. Ghazanfari, M. C. Leu, and R. G. Landers, "Extrusion-on-demand methods for high solids loading ceramic paste in freeform extrusion fabrication," Virtual Phys. Prototyp., vol. 12, no. 3, pp. 193–205, 2017.

[26]   ASTM C1327, "Standard test method for Vickers indentation hardness of advanced ceramics," West Conshohocken, PA, 2015.

[27]   L. Sun, A. Sneller, and P. Kwon, "Fabrication of alumina/zirconia functionally graded material: From optimization of processing parameters to phenomenological constitutive models," Mater. Sci. Eng. A, vol. 488, no. 1–2, pp. 31–38, 2008.

[28]   C. Kaya, "Al_2O_3-Y-TZP/Al_2O_3 functionally graded composites of tubular shape from nano-sols using double-step electrophoretic deposition," J. Eur. Ceram. Soc., vol. 23, no. 10, pp. 1655–1660, 2003.

[29]   A. Nevarez-Rascon, A. Aguilar-Elguezabal, E. Orrantia, and M. H. Bocanegra-Bernal, "On the wide range of mechanical properties of ZTA and ATZ based dental ceramic composites by varying the Al_2O_3 and ZrO_2 content," Int. J. Refract. Met. Hard Mater., vol. 27, no. 6, pp. 962–970, 2009.

[30] Z. Wu, W. Liu, H. Wu, R. Huang, R. He, Q. Jiang, Y. Chen, X. Ji, Z. Tian, and S. Wu, "Research into the mechanical properties, sintering mechanism and microstructure evolution of Al_2O_3-ZrO_2 composites fabricated by a stereolithography-based 3D printing method," Mater. Chem. Phys., vol. 207, pp. 1–10, 2018.

SECTION

2. CONCLUSIONS

A freeform extrusion fabrication process for producing ceramic parts, called Ceramic On-Demand Extrusion (CODE) was recently proposed. Further investigation and development of the CODE process are presented in this dissertation. To improve the fabrication precision of freeform extrusion fabrication process, Extrusion-On-Demand methods based on ram extruder, shutter valve, and auger extruder were first investigated for high solids loading ceramic pastes. Advantages and disadvantages of each method were discussed, and tentative guidelines for selecting the extrusion mechanism were given. The auger extruder was determined as the most suitable extrusion mechanism for high solids loading ceramic pastes.

A novel CODE fabrication system was built, auger extruders were integrated into the system. To examine the capabilities of the CODE process and fabrication system, ZrO_2 specimens were fabricated and characterized. A relative density of 99.1%-99.5% was achieved. The mechanical properties of parts were extensively studied. These properties surpass those produced by most other additive manufacturing processes and match those produced by conventional fabrication techniques.

A method of fabricating ceramic components by the Ceramic On-Demand Extrusion (CODE) process with the use of sacrificial support material has been developed. Calcium carbonate ($CaCO_3$) was identified as a sacrificial material. Geometrically simple and complex sample parts were successfully fabricated using Al_2O_3

as the main material and with $CaCO_3$ as the support material. A support material removal process was developed by using two-step sintering. The $CaCO_3$ support material was removed by dissolving in acid solution or water after the 1st-step sintering at 1100 °C, and then the parts went through the 2nd-step sintering at 1500 °C to obtain the dense ceramic parts.

A dynamic extrusion-mixing device was developed for fabricating functionally graded materials (FGM) by the Ceramic On-Demand Extrusion process. The effectiveness of this device was validated by fabricating FGM specimens graded from pure Al_2O_3 to Al_2O_3/ZrO_2 with predetermined material gradients. The FGM specimens were sintered at 1500 °C and the material composition of each layer in the sintered FGM specimens was validated by measuring the atomic percentage of Al and Zr by energy dispersive spectroscopy (EDS), and compared to the original design of compositions. A 1% average error of material composition was observed from the comparison. Deformations were measured on the dried and sintered FGM specimens. Greater material composition gradients led to larger deformations of specimens. The Vickers hardness decreased from 18.4 GPa to 15.0 GPa as the volume percentage of ZrO_2 increased from 0 to 50 vol% in Al_2O_3/ZrO_2 layers.

3. RECOMMENDATIONS FOR FUTURE WORK

Although the mechanical properties of parts produced by the Ceramic On-Demand Extrusion (CODE) process made of several materials have been extensively studied, there are many other ceramics, as well as metals which need to be studied [84] [85], and examine their properties. In fact, CODE is still in its fledgling stage, and many more studies need to be done to fully establish the process.

More alternatives to the support materials need to be developed. Although the $CaCO_3$ paste proposed in paper III was proven to be a suitable material, however, a tedious two-step sintering was needed due to the incompatibility between $CaCO_3$ and Al_2O_3 at the sintering temperature. Sacrificial materials that can be removed before the firing process can avoid the cofiring of support and main materials [88]. Moreover, the $CaCO_3$ paste must be prepared with proper solids loading so that it matches the shrinkage of the main material during the drying and cofiring process to avoid cracking, this issue could also be addressed by identifying alternative fugitive materials.

The dynamic mixing device introduced in paper IV demonstrated the capability of fabricating FGMs with accurate control of materials composition. However, optimization or the design of the mixing device can be expected to reduce the materials transition delay and hence increase the resolution of a varying materials composition. An in-depth study of the sintering process of FGMs is needed. Finally, an advanced control scheme needs to be developed to fabricated FGM specimens with complex material distribution. Fabrication of FGMs with other materials including metals can be studied using this device.

REFERENCES

[1]   H. Miyanaji, S. Zhang, A. Lassell, A. Zandinejad, and L. Yang, "Process development of porcelain ceramic material with binder jetting process for dental applications," *J. Miner. Met. Mater. Soc.*, vol. 68, no. 3, pp. 831–841, 2016.

[2]   M. C. Leu and D. A. Garcia, "Development of Freeze-form Extrusion Fabrication with use of sacrificial material," in *Proceedings of the 24th Annual Solid Freeform Fabrication Symposium*, 2013, pp. 326–345.

[3]   J. Cesarano, R. Segalman, and P. Calvert, "Robocasting provides moldless fabrication from slurry deposition," *Ceram. Ind.*, vol. 148, no. 4, p. 94, 1998.

[4]   J. Luo, H. Pan, and E. C. Kinzel, "Additive manufacturing of glass," *J. Manuf. Sci. Eng.*, vol. 136, no. 6, p. 061024, 2014.

[5]   M. C. Leu, L.Tang, B. Deuser, R.G. Landers, G.E. Hilmas, S. Zhang, J. Watts, "Freeze-form extrusion fabrication of composite structures," in *Proceedings of the 22nd Annual International Solid Freeform Fabrication Symposium*, 2011, pp. 111–124.

[6]   R. Clancy, V. Jamalabad, P. Whalen, P. Bhargava, C. Dai, S. Rangarajan, S. Wu, S. Danforth, N. Langrana, A. Safari, "Fused deposition of ceramics : progress towards a robust and controlled process for commercialization," in *Proceedings of the 8th Annual International Solid Freeform Fabrication Symposium*, 1997, pp. 185–194.

[7]   A. D. Lantada, A. de Blas Romero, M. Schwentenwein, C. Jellinek, and J. Homa, "Lithography-based ceramic manufacture (LCM) of auxetic structures: present capabilities and challenges," *Smart Mater. Struct.*, vol. 25, no. 5, p. 054015, 2016.

[8]   M. Schwentenwein and J. Homa, "Additive manufacturing of dense alumina ceramics," *Int. J. Appl. Ceram. Technol.*, vol. 12, no. 1, pp. 1–7, 2015.

[9]   W. Harrer, M. Schwentenwein, T. Lube, and R. Danzer, "Fractography of zirconia-specimens made using additive manufacturing (LCM) technology," *J. Eur. Ceram. Soc.*, vol. 37, no. 14, pp. 4331–4338, 2017.

[10]   U. Scheithauer, E. Schwarzer, T. Moritz, and A. Michaelis, "Additive anufacturing of ceramic heat exchanger: opportunities and limits of the lithography-based ceramic manufacturing (LCM)," *J. Mater. Eng. Perform.*, vol. 27, no. 1, pp. 14–20, 2018.

[11]   P. Bertrand, F. Bayle, C. Combe, P. Goeuriot, and I. Smurov, "Ceramic components manufacturing by selective laser sintering," *Appl. Surf. Sci.*, vol. 254, no. 4, pp. 989–992, 2007.

[12]   J. Wilkes, Y. Hagedorn, W. Meiners, and K. Wissenbach, "Additive manufacturing of ZrO_2 -Al_2O_3 ceramic components by selective laser melting," *Rapid Prototyp. J.*, vol. 19, no. 1, pp. 51–57, 2013.

[13]   F. Niu, D. Wu, G. Ma, J. Wang, M. Guo, and B. Zhang, "Nanosized microstructure of Al_2O_3-ZrO_2 (Y_2O_3) eutectics fabricated by laser engineered net shaping," *Scr. Mater.*, vol. 95, no. 1, pp. 39–41, 2015.

[14]   F. Niu, D. Wu, G. Ma, J. Wang, J. Zhuang, and Z. Jin, "Rapid fabrication of eutectic ceramic structures by laser engineered net shaping," *Procedia CIRP*, vol. 42, pp. 91–95, 2016.

[15]   G. Ma, D. Wu, F. Niu, and H. Zou, "Microstructure evolution and mechanical property of pulsed laser welded Ni-based superalloy," *Opt. Lasers Eng.*, vol. 72, no. August 2016, pp. 39–46, 2015.

[16]   S. Yan, D. Wu, F. Niu, G. Ma, and R. Kang, "Al_2O_3-ZrO_2 eutectic ceramic via ultrasonic-assisted laser engineered net shaping," *Ceram. Int.*, vol. 43, no. 17, pp. 15905–15910, 2017.

[17]   N. Travitzky, A. Bonet, B. Dermeik, T. Fey, I. Filbert-Demut, L. Schlier, T. Schlordt, P. Greil, "Additive manufacturing of ceramic-based materials," *Adv. Eng. Mater.*, vol. 16, no. 6, pp. 729–754, 2014.

[18]   M. A. Jafari, W. Han, F. Mohammadi, A. Safari, S. C. Danforth, and N. Langrana, "A novel system for fused deposition of advanced multiple ceramics," *Rapid Prototyp. J.*, vol. 6, no. 3, pp. 161–175, Sep. 2000.

[19]   A. Zocca, P. Colombo, C. M. Gomes, and J. Günster, "Additive Manufacturing of Ceramics: Issues, Potentialities, and Opportunities," *J. Am. Ceram. Soc.*, vol. 98, no. 7, pp. 1983–2001, 2015.

[20]   M. C. Leu, B. K. Deuser, L. Tang, R. G. Landers, G. E. Hilmas, and J. L. Watts, "Freeze-form extrusion fabrication of functionally graded materials," *CIRP Ann. - Manuf. Technol.*, vol. 61, no. 1, pp. 223–226, 2012.

[21]   A. Li, A. Thornton, B. Deuser, J. Watts, M.C. Leu, G. E. Hilmas, R. G. Landers, "Freeze-form extrusion fabrication of functionally graded material composites using zirconium carbide and tungsten," in *Proceedings of the 23th Annual Solid Freeform Fabrication Symposium*, 2012, pp. 467–479.

[22]   S. L. Morissette, J. a Lewis, J. Cesarano, D. B. Dimos, and T. Y. Baer, "Solid freeform fabrication of aqueous alumina-poly(vinyl alcohol) gelcasting suspensions," *J. Am. Ceram. Soc.*, vol. 83, no. 10, pp. 2409–2416, 2000.

[23]   J. N. Stuecker, J. Cesarano, and D. A. Hirschfeld, "Control of the viscous behavior of highly concentrated mullite suspensions for robocasting," *J. Mater. Process. Technol.*, vol. 142, no. 2, pp. 318–325, 2003.

[24]   J. Cesarano, J. G. Dellinger, M. P. Saavedra, D. D. Gill, R. D. Jamison, B. A. Grosser, J. M. Sinn-Hanlon, M. S. Goldwasser, "Customization of load-bearing hydroxyapatite lattice scaffolds," *Int. J. Appl. Ceram. Technol.*, vol. 2, no. 3, pp. 212–220, 2005.

[25]   P. Miranda, E. Saiz, K. Gryn, and A. P. Tomsia, "Sintering and robocasting of β-tricalcium phosphate scaffolds for orthopaedic applications," *Acta Biomater.*, vol. 2, no. 4, pp. 457–466, 2006.

[26]   R. Vaidyanathan, J. Walish, J. L. Lombardi, S. Kasichainula, P. Calvert, and K. C. Cooper, "The extrusion freeforming of functional ceramic prototypes," *JOM*, vol. 52, no. 12, pp. 34–37, 2000.

[27]   K. Stuffle, A. Mulligan, P. Calvert, and J. Lombardi, "Solid freebody forming of ceramics from polymerizable slurry," in *Proceedings of the 4th Annual Solid Freeform Fabrication Symposium*, 1993, pp. 60–63.

[28]   I. Grida and J. R. G. Evans, "Extrusion freeforming of ceramics through fine nozzles," *J. Eur. Ceram. Soc.*, vol. 23, no. 5, pp. 629–635, 2003.

[29]   S. Danforth, "Fused deposition of ceramics: a new technique for the rapid fabrication of ceramic components," *Mater. Technol.*, vol. 10, no. 7–8, pp. 144–146, 1995.

[30]   M. K. Agarwala, R. Van Weeren, A. Bandyopadhyayl, P. J. Whalen, A. Safari, and S. C. Danforth, "Fused deposition of ceramics and metals: an overview," in *Proceedings of the 7th Annual Solid Freeform Fabrication Symposium*, 1996.

[31]   T. Huang, M. S. Mason, G. E. Hilmas, and M. C. Leu, "Freeze-form extrusion fabrication of ceramic parts," *Virtual Phys. Prototyp.*, vol. 1, no. 2, pp. 93–100, 2006.

[32]   U. Scheithauer, E. Schwarzer, H.-J. Richter, and T. Moritz, "Thermoplastic 3D printing-an additive manufacturing method for producing dense ceramics," *Int. J. Appl. Ceram. Technol.*, vol. 12, no. 1, pp. 26–31, 2015.

[33] A. Safari, M. Allahverdi, and E. K. Akdogan, "Solid freeform fabrication of piezoelectric sensors and actuators," in *Frontiers of Ferroelectricity*, Boston, MA: Springer US, 2006, pp. 177–198.

[34] G. M. Lous, I. A. Cornejo, T. F. McNulty, A. Safari, and S. C. Danforth, "Fabrication of piezoelectric ceramic polymer composite transducers using fused deposition of ceramics," *J. Am. Ceram. Soc.*, vol. 83, no. 1, pp. 124–28, 2000.

[35] H. B. Denham, J. Cesarano, B. H. King, P. Calvert, "Mechanical behavior of robocast alumina," in *Proceedings of the 9th Annual Solid Freeform Fabrication Symposium*, 1998, pp. 589–596.

[36] K. Cai, B. Román-Manso, J. E. Smay, J. Zhou, M. I. Osendi, M. Belmonte, P. Miranzo, "Geometrically complex silicon carbide structures fabricated by robocasting," *J. Am. Ceram. Soc.*, vol. 95, no. 8, pp. 2660–2666, 2012.

[37] J. A. Lewis, J. E. Smay, J. Stuecker, and J. Cesarano, "Direct ink writing of three-dimensional ceramic structures," *J. Am. Ceram. Soc.*, vol. 89, no. 12, pp. 3599–3609, 2006.

[38] X. Li, W. Li, F. Rezaei, and A. Rownaghi, "Catalytic cracking of n-hexane for producing light olefins on 3D-printed monoliths of MFI and FAU zeolites," *Chem. Eng. J.*, vol. 333, pp. 545–553, 2018.

[39] C. Murphy, K. Kolan, W. Li, J. Semon, D. Day, and M. Leu, "3D bioprinting of stem cells and polymer/bioactive glass composite scaffolds for tissue engineering," *Int. J. Bioprinting*, vol. 3, no. 1, 2017.

[40] C. Murphy, K. C. R. Kolan, M. Long, W. Li, M. C. Leu, J. A. Semon, D. E. Day, "3D printing of a polymer bioactive glass composite for bone repair," in *Proceedings of the 27th Annual Solid Freeform Fabrication Symposium*, 2016, pp. 1718–1731.

[41] K. C. R. Kolan, W. Li, R. Althage, J. A. Semon, D. E. Day, and M. C. Leu, "Solvent and melt based extrusion 3D printing of polycaprolactone bioactive glass composite for tissue engineering," in *Proceedings of the 3rd International Conference on Progress in Additive Manufacturing (Pro-AM 2018)*, 2018, pp. 176–182.

[42] A. S. Thornton, "Freeze-form extrusion fabrication of boron carbide," Missouri University of Science and Technology, 2014.

[43] T. S. Huang, M. N. Rahaman, N. D. Doiphode, M. C. Leu, B. S. Bal, E. E. Day, X. Liu, "Freeze extrusion fabrication of 13–93 bioactive glass scaffolds for bone repair," *J. Mater. Sci. Mater. Med.*, vol. 22, no. 3, pp. 512–523, 2011.

[44]   T. Huang, G. E. Hilmas, W. G. Fahrenholtz, and M. C. Leu, "Dispersion of zirconium diboride in an aqueous,high-solids paste," *Int. J. Appl. Ceram. Technol.*, vol. 4, no. 5, pp. 470–479, 2007.

[45]   M. Li, A. Ghazanfari, W. Li, R. G. Landers, and M. C. Leu, "Modeling and analysis of paste freezing in freeze-form extrusion fabrication of thin-wall parts via a lumped method," *J. Mater. Process. Technol.*, vol. 237, pp. 163–180, 2016.

[46]   H. Zomorodi and R. G. Landers, "Extrusion based additive manufacturing using explicit model predictive control," in *Proceedings of the 2016 American Control Conference*, 2016, pp. 1747–1752.

[47]   B. K. Deuser, L. Tang, R. G. Landers, M. C. Leu, and G. E. Hilmas, "Hybrid extrusion force-velocity control using freeze-form extrusion fabrication for functionally graded material parts," *J. Manuf. Sci. Eng.*, vol. 135, no. 4, p. 041015, 2013.

[48]   X. Zhao, R. G. Landers, and M. C. Leu, "Adaptive extrusion force control of freeze-form extrusion fabrication processes," *J. Manuf. Sci. Eng.*, vol. 132, no. 6, p. 064504, 2010.

[49]   S. Iyer, J. McIntosh, A. Bandyopadhyay, N. Langrana, A. Safari, S. C. Danforth, R. B. Clancy, C. Gasdaska, P. J. Whalen, "Microstructural characterization and mechanical properties of Si 3 N 4 formed by fused deposition of ceramics," *Int. J. Appl. Ceram. Technol.*, vol. 5, no. 2, pp. 127–137, 2008.

[50]   J. Li, "An experimental study of fabrication temperature effect on aqueous extrusion freeform fabrication," Missouri University of Science and Technology, 2015.

[51]   A. Ghazanfari, W. Li, M. C. Leu, and G. E. Hilmas, "A novel extrusion-based additive manufacturing process for ceramic parts," in *Proceedings of the 27th Annual International Solid Freeform Fabrication Symposium*, 2016, pp. 1509–1529.

[52]   A. Ghazanfari, W. Li, M. C. Leu, and G. E. Hilmas, "A novel freeform extrusion fabrication process for producing solid ceramic components with uniform layered radiation drying," *Addit. Manuf.*, vol. 15, pp. 102–112, 2017.

[53]   A. Ghazanfari, W. Li, and M. C. Leu, "Adaptive rastering algorithm for freeform extrusion fabrication processes," *Virtual Phys. Prototyp.*, vol. 10, no. 3, pp. 163–172, 2015.

[54]   A. Ghazanfari, W. Li, M. C. Leu, and R. G. Landers, "Optimal rastering orientation in freeform extrusion fabrication processes," in *Proceedings of the 26th Annual Solid Freeform Fabrication Symposium*, 2015, pp. 1324–1333.

[55] A. Ghazanfari, W. Li, M. C. Leu, and R. G. Landers, "Planning freeform extrusion fabrication processes with consideration of horizontal staircase effect," in *Proceedings of the 26th Annual Solid Freeform Fabrication Symposium*, 2015, pp. 1313–1323.

[56] D. McMillen, W. Li, M. C. Leu, G. E. Hilmas, and J. Watts, "Designed extrudate for additive manufacturing of zirconium diboride by ceramic on-demand extrusion," in *Proceedings of the 27th Annual Solid Freeform Fabrication Symposium*, 2016, pp. 929–938.

[57] A. Ghazanfari, W. Li, M. C. Leu, J. L. Watts, and G. E. Hilmas, "Additive manufacturing and mechanical characterization of high density fully stabilized zirconia," *Ceram. Int.*, vol. 43, no. 8, pp. 6082–6088, 2017.

[58] A. Ghazanfari, W. Li, M. Leu, J. Watts, and G. Hilmas, "Mechanical characterization of parts produced by ceramic on-demand extrusion process," *Int. J. Appl. Ceram. Technol.*, vol. 14, no. 3, pp. 486–494, 2017.

[59] W. Li, A. Ghazanfari, D. McMillen, M. C. Leu, G. E. Hilmas, and J. Watts, "Characterization of zirconia specimens fabricated by ceramic on-demand extrusion," *Ceram. Int.*, vol. 44, no. 11, pp. 12245–12252, 2018.

[60] A. Ghazanfari, W. Li, M. C. Leu, J. Watts, Y. Zhuang, and J. Huang, "Freeform extrusion fabrication of advanced ceramic components with embedded sapphire optical fiber sensors," in *ASME 2016 Conference on Smart Materials, Adaptive Structures and Intelligent Systems, SMASIS 2016*, 2016, vol. 1, p. V001T04A014.

[61] A. Ghazanfari, W. Li, M. C. Leu, Y. Zhuang, and J. Huang, "Advanced ceramic components with embedded sapphire optical fiber sensors for high temperature applications," *Mater. Des.*, vol. 112, pp. 197–206, 2016.

[62] W. Li, A. Ghazanfari, D. Mcmillen, M. C. Leu, G. E. Hilmas, and J. Watts, "Properties of partially stabilized zirconia components fabricated by the ceramic on-demand extrusion process," in *Proceedings of the 27th Annual Solid Freeform Fabrication Symposium*, 2016, pp. 916–928.

[63] W. Li, A. Ghazanfari, D. Mcmillen, A. Scherff, M. C. Leu, and G. E. Hilmas, "Fabricating zirconia parts with organic support material by the ceramic on-demand extrusion process," in *Proceedings of the 28th Annual Solid Freeform Fabrication Symposium*, 2017, pp. 605–615.

[64] J. Luo, L. J. Gilbert, D. A. Bristow, R. G. Landers, J. T. Goldstein, A. M. Urbas, E. C. Kinzel, "Additive manufacturing of glass for optical applications," *SPIE Lase*, vol. 9738, p. 97380Y–97380Y–9, 2016.

[65] J. Klein, M. Stern, G. Franchin, M. Kayser, C. Inamura, S. Dave, J. C. Weaver, P. Houk, P. Colombo, M. Yang, N. Oxman, "Additive manufacturing of optically transparent glass," *3D Print. Addit. Manuf.*, vol. 2, no. 3, pp. 92–105, 2015.

[66] J. Luo, L. J. Gilbert, C. Qu, R. Landers, D. Bristow, and E. Kinzel, "Additive manufacturing of transparent soda-lime glass using a filament-fed process," *J. Manuf. Sci. Eng.*, vol. 139, no. 6, p. 061006, 2016.

[67] J. Luo, L. J. Gilbert, C. Qu, B. Morrow, D. A. Bristow, R. G. Landers, J. Goldstein, A. Urbas, E. C. Kinzel, "Solid freeform fabrication of transparent fused quartz using a filament fed process," in *Proceedings of the 26th Annual International Solid Freeform Fabrication Symposium*, 2015, pp. 122–133.

[68] J. Li and G. Deng, "Technology development and basic theory study of fluid dispensing - a review," in *Proceedings of the 6th IEEE CPMT Conference on High Density Microsystem Design and Packaging and Component Failure Analysis*, 2004, pp. 198–205.

[69] T. Oakes, P. Kulkarni, R. G. Landers, and M. C. Leu, "Development of extrusion-on-demand for ceramic freeze-form extrusion fabrication," in *Proceedings of the 20th Annual International Solid Freeform Fabrication Symposium*, 2009, pp. 206–218.

[70] W. Li, A. G. Ghazanfari, M. C. Leu, and R. G. Landers, "Methods of extrusion on demand for high solids loading ceramic paste in freeform extrusion fabrication," in *Proceedings of the 26th Annual Solid Freeform Fabrication Symposium*, 2015, pp. 332–345.

[71] W. Li, A. Ghazanfari, M. C. Leu, and R. G. Landers, "Extrusion-on-demand methods for high solids loading ceramic paste in freeform extrusion fabrication," *Virtual Phys. Prototyp.*, vol. 12, no. 3, pp. 193–205, 2017.

[72] Y. Jin, Y. He, and J. Fu, "Support generation for additive manufacturing based on sliced data," *Int. J. Adv. Manuf. Technol.*, vol. 80, no. 9–12, pp. 2041–2052, 2015.

[73] X. Huang, C. Ye, S. Wu, K. Guo, and J. Mo, "Sloping wall structure support generation for fused deposition modeling," *Int. J. Adv. Manuf. Technol.*, vol. 42, no. 11–12, pp. 1074–1081, 2009.

[74] P. Das, R. Chandran, R. Samant, and S. Anand, "Optimum Part Build Orientation in Additive Manufacturing for Minimizing Part Errors and Support Structures," *Procedia Manuf.*, vol. 1, pp. 343–354, 2015.

[75] J. Vanek, J. A. G. Galicia, and B. Benes, "Clever support: efficient support structure generation for digital fabrication," *Comput. Graph. Forum*, vol. 33, no. 5, pp. 117–125, 2014.

[76]   R. M. Mahamood and E. T. Akinlabi, *Functionally graded materials*. Springer, 2017.

[77]   L. Yang, H. Miyanaji, D. Janaki Ram, A. Zandinejad, and S. Zhang, "Functionally graded ceramic based materials using additive manufacturing: review and progress," *Addit. Manuf. Strateg. Technol. Adv. Ceram.*, vol. 258, pp. 43–55, 2016.

[78]   Y. Li, Y. Shen, C.-H. Hung, M. C. Leu, and H.-L. Tsai, "Additive manufacturing of Zr-based metallic glass structures on 304 stainless steel substrates via V/Ti/Zr intermediate layers," *Mater. Sci. Eng. A*, vol. 729, pp. 185–195, 2018.

[79]   W. Cui, S. Karnati, X. Zhang, E. Burns, F. Liou, "Fabrication of AlCoCrFeNi High-Entropy Alloy Coating on an AISI 304 Substrate via a CoFe2Ni Intermediate Layer," *Entropy*, vol. 21, no. 1, p. 2, 2018.

[80]   L. Yang, H. Miyanaji, D. Janaki Ram, A. Zandinejad, and S. Zhang, "Functionally graded ceramic based materials using additive manufacturing: review and progress," in *Additive Manufacturing and Strategic Technologies in Advanced Ceramics*, John Wiley & Sons, Ltd, 2016, pp. 43–55.

[81]   M. N. Rahaman, A. Yao, B. S. Bal, J. P. Garino, and M. D. Ries, "Ceramics for prosthetic hip and knee joint replacement," *J. Am. Ceram. Soc.*, vol. 90, no. 7, pp. 1965–1988, 2007.

[82]   Y. Fang, Y. Zhang, J. Song, H. Fan, and L. Hu, "Design and fabrication of laminated-graded zirconia self-lubricating composites," *Mater. Des.*, vol. 49, pp. 421–425, 2013.

[83]   M. Mott and J. R. . Evans, "Zirconia/alumina functionally graded material made by ceramic ink jet printing," *Mater. Sci. Eng. A*, vol. 271, no. 1–2, pp. 344–352, 1999.

[84]   L. Sun, A. Sneller, and P. Kwon, "Fabrication of alumina/zirconia functionally graded material: From optimization of processing parameters to phenomenological constitutive models," *Mater. Sci. Eng. A*, vol. 488, no. 1–2, pp. 31–38, 2008.

[85]   C. Hillman, Z. Suo, and F. F. Lange, "Cracking of laminates subjected to biaxial tensile stresses," *J. Am. Ceram. Soc.*, vol. 79, no. 8, pp. 2127–2133, 1996.

[86]   P. Z. Cai, D. J. Green, and G. L. Messing, "Constrained densification of alumina/zirconia hybrid laminates, I: experimental observations of processing defects," *J. Am. Ceram. Soc.*, vol. 80, no. 8, pp. 1929–1939, 2005.

[87] J. C. Chang, B. V. Velamakanni, F. F. Lange, and D. S. Pearson, "Centrifugal consolidation of Al_2O_3 and Al_2O_3/ZrO_2 composite slurries vs interparticle potentials: particle packing and mass segregation," *J. Am. Ceram. Soc.*, vol. 74, no. 9, pp. 2201–2204, 1991.

[88] Y. P. Zeng, D. L. Jiang, and T. Watanabe, "Fabrication and properties of tape-cast laminated and functionally gradient alumina-titanium carbide materials," *J. Am. Ceram. Soc.*, vol. 83, no. 12, pp. 2999–3003, 2000.

[89] Li Sun, A. Sneller, and P. Kwon, "Powder selection in cosintering multi-layered ceramic functionally graded materials based on the densification kinetics curves," *J. Compos. Mater.*, vol. 43, no. 5, pp. 469–482, 2009.

[90] M. Mehrali, H. Wakily, and I. H. S. C. Metselaar, "Residual stress and mechanical properties of Al_2O_3/ZrO_2 functionally graded material prepared by EPD from 2-butanone based suspension," *Adv. Appl. Ceram.*, vol. 110, no. 1, pp. 35–40, 2011.

[91] W. Li, A. Ghazanfari, D. McMillen, M. C. Leu, G. E. Hilmas, and J. Watts, "Fabricating ceramic components with water dissolvable support structures by the Ceramic On-Demand Extrusion process," *CIRP Ann.*, vol. 66, no. 1, pp. 225–228, 2017.

[92] W. Li, A. J. Martin, B. Kroehler, A. Henderson, T. Huang, J. Watts, G. E. Hilmas, M. C. Leu, "Fabricating functionally graded materials by ceramic on-demand extrusion with dynamic mixing," in *Proceedings of the 29th Annual International Solid Freeform Fabrication Symposium*, 2018, pp. 1087–1099.

VITA

Wenbin Li was born in Yichang, China. He received his B.S. and M.S. degrees in Mechanical Engineering from Beijing Institute of Technology (BIT) in 2011 and 2013, respectively. Wenbin joined the Innovative Smart & Additive Manufacturing (ISAM) laboratory at Missouri University of Science and Technology (Missouri S&T) in Spring 2014 and started working on the development of additive manufacturing processes and systems with a focus on structural ceramics and ceramic composites.

During his Ph.D. studies, Wenbin Li won the Missouri S&T College of Engineering and Computing Dean's Ph.D. Scholar Award (2018), Best Paper Award at Intelligent Systems Center Research Symposium (2018), Best Student Paper Award at the ASME Symposium on Integrated Systems Design and Implementation (2016), 2nd Best Paper Award at Intelligent Systems Center Research Symposium (2015), and 2nd Best Poster Award at Tenth Annual Intelligent Systems Center Poster Presentation (2014).

In April 2019, he received his Ph.D. under the direction of Dr. Ming C. Leu in Mechanical Engineering from Missouri University of Science and Technology, Rolla, Missouri, USA.